

# Understanding spatial and temporal variability in Supraglacial Lakes on an Antarctic Ice Shelf: A 31-year study of George VI

Thomas Barnes – MSc By Research – Environmental Science



## **Supervisors:**

Dr. A. Leeson; Dr. M. McMillan

This thesis is submitted for the degree of  
***MSc (by research) Environmental Science***

August 1, 2020

LANCASTER ENVIRONMENT CENTRE, LANCASTER UNIVERSITY

## Acknowledgements

Thanks to Dr. Amber Leeson and Dr. Mal McMillan for providing support, guidance and an enthusiasm for the subject which has kept me deeply interested in this project and the surrounding science throughout.

Additional thanks go to Diarmuid Corr and Jez Carter for providing data and offering their help in data testing and as test subjects for method tests.

Special thanks to Bryony Freer for the sharing of information between our parallel projects, allowing for greater, more in-depth analysis of the target region.

**Abstract** – Floating ice shelves cover ~1.5million km<sup>2</sup> of Antarctica's area, and are important as they buttress land ice, which limits sea level rise. In recent years, several such Antarctic ice shelves have collapsed or retreated. Supraglacial lakes are linked to warm periods and influence the stability of ice shelves through hydrofracture. Climate change induced temperature increases may increase lake presence, thus decreasing stability. Monitoring 'at risk' ice shelves is therefore important to understand their likelihood of fracture. George VI is located on the western Antarctic Peninsula, covering ~23200 km<sup>2</sup>, and has had high lake densities in its northern sector. This study analyses 31 years of imagery to understand the long-term and seasonal dynamics of lake evolution. This is the first study to characterise supraglacial lake variability in the long- and short-term on George VI, thus producing a comprehensive picture of lake evolution. Here I use a semi-automated technique to map lakes in >160 satellite images from Sentinel 2 and Landsat 4-8. Additional influences on stability and lake presence are gauged using climatic and glaciological data. Analysis of recent imagery shows that the apparent high lake density in summer 2020 is not unique on George VI, with 1989-90 having similar densities persisting over ≥3 years. Decadal average temperature and annual summer snowfall are found to be primary controls on lake density at their respective timescales, the former being influenced by changes in the southern annular mode. Climatic controls on an intra-annual scale are complex, with melt, snowfall and temperature influencing lake density. Although lakes are widespread in several years, little evidence has been found of the unstable drainage which preceded neighbouring ice shelf collapse. This study demonstrates the value of frequent monitoring by current generations of optical satellites in lake analysis; and provides the first long-term catalogue of lakes on George VI.

**Keywords:** Supraglacial lake, Optical satellites, Antarctica, George VI, Ice shelves.

# **Table of Contents**

## **(1.0) Introduction 4**

## **(2.0) Literature Review 5**

- (2.1) Climate Setting of GVI and the AP region 5
- (2.2) George VI Ice Shelf, Antarctic Peninsula 6
- (2.3) Supraglacial Lakes and Hydrology 9
- (2.4) Lake Identification on Ice Masses 10
- (2.5) Types of Satellite Imagery 11
- (2.6) Temporal Evolution 11

## **(3.0) Data and Methods 12**

- (3.1) Data Collection 14
  - (3.1.1) *Satellite Imagery 14*
  - (3.1.2) *Regional Glaciological Data 14*
  - (3.1.3) *Regional Climatic Data 14*
- (3.2) Data Processing 15
  - (3.2.1) *Delineation of SGLs 15*
  - (3.2.2) *Data Clean-up 16*
  - (3.2.3) *Method Testing 18*
- (3.3) Data Analysis 21
  - (3.3.1) *Polygons and Imagery 21*
  - (3.3.2) *Glaciological Data 22*
  - (3.3.3) *Climate Data 22*
  - (3.3.4) *Impact Estimation of Albedo 23*
  - (3.3.5) *Reflectance Calculation of Albedo 23*

## **(4.0) Results 24**

- (4.1) Climatic controls on Lake Formation 24
  - (4.1.1) *Inter-annual Variability in Lakes and Climatic Influences 24*
  - (4.1.2) *Intra-annual Variability in Lakes and Climatic Influences 30*
  - (4.1.3) *Pre-2000 climatic influences on SGLs 34*
- (4.2) Glaciological controls on lake formation 36
  - (4.2.1) *Evidence of lake drainage 38*
- (4.3) Albedo values and associated impacts 41

## **(5.0) Discussion 43**

- (5.1) Climatologically induced variation in SGLs on GVI 43
  - (5.1.1) *Interannual climatological variation 43*
  - (5.1.2) *Intra-annual climatological variation 44*
  - (5.1.3) *Pre-2000 climatological variation 45*
- (5.2) Glaciologically induced variation in SGLs on GVI 46
- (5.3) Drainage related impacts of SGLs on GVI 47
- (5.4) Albedo related impacts of SGLs on GVI 48
- (5.5) Limitations & Avenues for Future Work 48
  - (5.5.1) *Method Development 50*

## **(6.0) Conclusions 50**

## **(7.0) References 52**

## **(1.0) Introduction**

Ice shelves across West Antarctica are melting at a notable rate, with major collapse events in the past two decades showing clear signs of weakness in the polar regions – for example, Larsen B’s collapse in 2002 (Leeson et al., 2020). Current projects such as Antarctica 4D endeavour to understand and display a snapshot in time, or a ‘state of the system’ outlook on Antarctica, with particular attention paid to supraglacial lakes (SGLs) and melt channels. Supraglacial lakes have been shown to be directly linked to ice shelf collapse, thus showing a need for this focus (Bell et al., 2018). As ice shelves are part of the wider cryospheric system, which in turn links to the global system by managing temperatures, currents and other climatic factors, an understanding of ice shelves today is important.

This thesis aims to take a narrower spatial and wider temporal approach from the Antarctica 4D project, providing the basis for a long-term high temporal-resolution study of a region, allowing for more detailed analysis. The focus will be on George VI ice shelf (GVI), Antarctic Peninsula (AP), a significant candidate region which has been suggested to be at the ‘limit of its climatic stability’ (Branson, 2019; Holt et al., 2013). Thus, while wider studies take a ‘snapshot in time’ approach to Antarctic ice shelves, this will take a more focused view, studying how SGLs develop over time across a particularly vulnerable candidate ice shelf. This in turn will link into the wider study of climate and ice interactions, and provide a catalogue of lake development on GVI in the decades prior to a possible collapse – if collapse does occur. A second angle to the study focuses on the impact of these SGLs on GVI – particularly that of albedo and drainage across the ice mass.

This study’s primary aims are:

- 1) To understand temporal and spatial variations in SGLs on GVI on an intra- and inter-annual basis between 1989 and 2020.
- 2) To thus understand the possible impacts SGLs may have on GVI through drainage and the effects of albedo.
- 3) To identify further impacts on the stability of GVI and its lakes from glaciological and climatic datasets.

These will be achieved through a combination of optical satellite imagery from Landsat and Sentinel archives, glaciological data from MEaSURES and British Antarctic Survey (BAS), and climate data from BAS and two climate models – RACMO and ERA5. Further characteristics will be drawn using band calculation methods on the satellite imagery to retrieve lake depths and volumes, areas and monthly to yearly changes in some of these values.

To begin, this thesis will outline current knowledge and literature surrounding Antarctica, ice shelves and supraglacial lakes while identifying gaps which this study will fill. From there, methods and points of data collection that were used are identified and outlined, with sufficient detail to reproduce the methods used. Findings are then outlined and discussed, with possible implications on ice shelf stability for GVI, and the wider system being identified. Finally, limitations of the study are acknowledged, followed by clear conclusions on the gaps this study has filled, and possible future uses of the lake catalogue are identified.

## (2.0) Literature Review

### (2.1) Climate Setting of GVI and the AP region

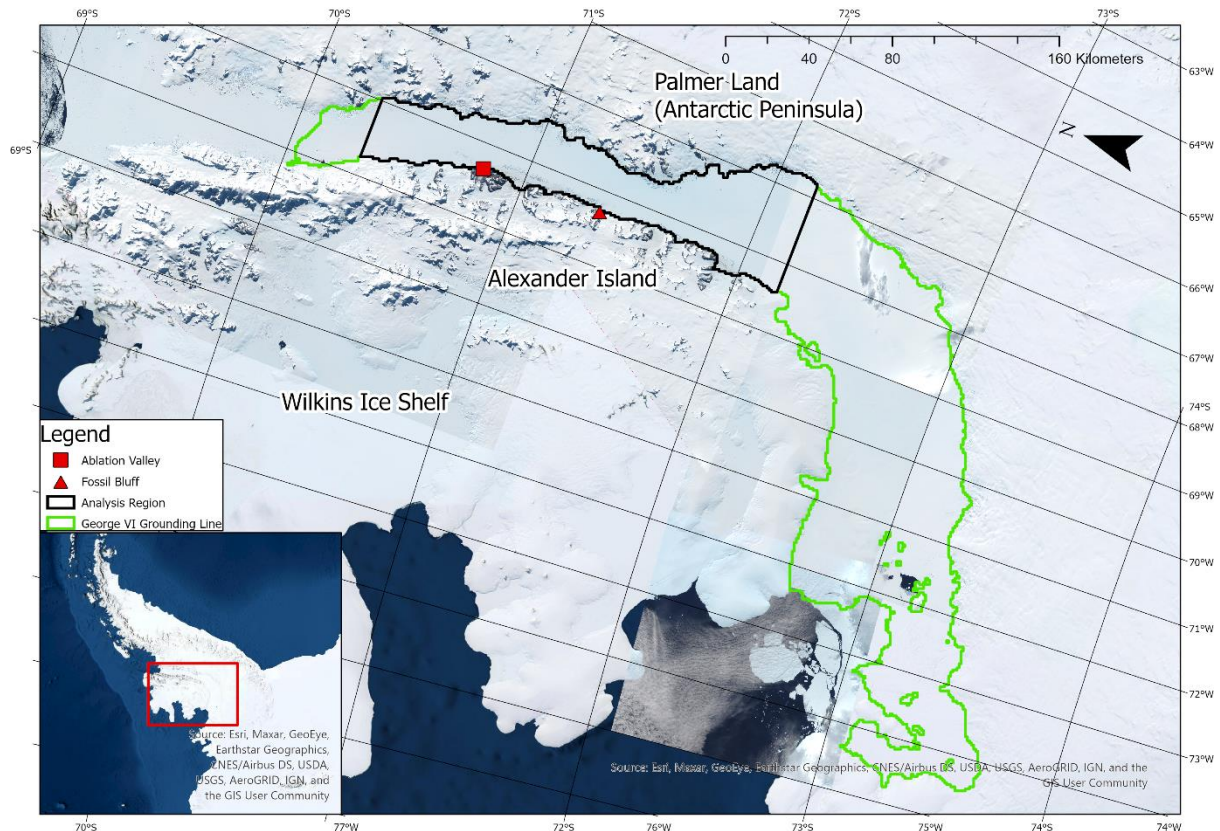


**Figure 1:** Map of GVI. Red identifies the region of the AP shown in the full image. Black identifies the primary area of study on GVI using the Bedmap2 boundary polygons, with green showing the full grounding line (Fretwell et al., 2013). Ablation Valley and Fossil Bluff are marked in red. Imagery from S2 (ESA, 2019).

Sources of melt in Antarctica stem from both ice dynamics, and climatological sources. Parts of the continent have been feeling the effects of anthropogenic climate change for several decades (Steig et al., 2009; Vaughan et al., 2003), with more severe melting emerging as recently as January 2020 (Hansen & Dauphin, 2020) and melting being projected to increase in the future (Naughten et al., 2018). This change will likely lead to localised regional warming at a higher rate than that of non-polar regions, as seen already in Greenland (IPCC, 2014). Such warming will lead to increased atmospheric and oceanic-driven melting and ice discharge, and may lead to the collapse of Antarctica's floating ice shelves, for example the Larsen B ice shelf which collapsed in 2002 (Glasser & Scambos, 2008). The loss of floating ice may lead indirectly to global sea level rise by the removal of their buttressing effect on grounded ice flow (Berthier et al., 2012), where an ice shelf slows the output of a glacier to the ocean by limiting flow velocity. Thus, their loss contributes to increased ice to sea delivery rates; estimated to be  $\sim 9 \text{ Gt yr}^{-1}$  at Larsen B since its collapse (Berthier et al., 2012).

The AP is the most sensitive region of Antarctica to change due to its latitude and being surrounded on three sides by the Southern Ocean, leading to increased influence of ocean currents and water availability in the atmosphere (Jun et al., 2016). Hambrey, et al. (2015), outlines the AP as Antarctica's region of highest surface melt, predominantly melting

on ice shelves; the region typically experiences higher temperatures than East or West Antarctica (EA, WA) alongside higher precipitation (Figure 2). This is likely due to several factors, notably proximity to the ocean, latitude, topographic (föhn) winds and high proportion of sea-ice versus grounded-ice. This dynamic climatic setting, coupled with the ratio of sea to grounded ice (for example, GVI, Larsen C), leaves the AP as one of the highest risk regions in terms of climate warming (Bell et al., 2018). Climatic impacts would most likely emerge through the break-up of ice shelves, and reduction of the buttressing effect they provide to grounded ice (Kingslake et al., 2017).

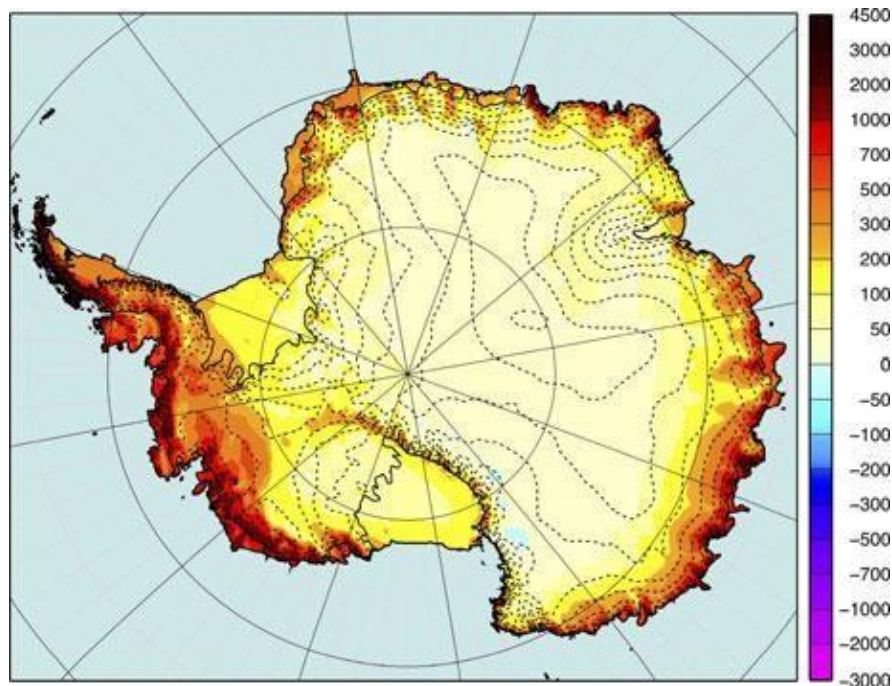


**Figure 2:** Surface mass balance (1989-2009) from RACMO 2, adapted from Van den Broeke et al., (2011). Values in  $\text{kg m}^{-2} \text{a}^{-1}$ , dashed contours at every 500 m a.s.l.

## (2.2) George VI Ice Shelf, Antarctic Peninsula

GVI Ice Shelf is situated on the western side of the AP, within George VI Sound between the AP mainland and Alexander Island. Its total surface area is  $\sim 22,000 \text{ km}^2$ , making it one of the largest AP ice shelves. Thus, GVI is located in one of the most northerly regions of Antarctica and is therefore subject to the impacts of a lower latitude - namely longer summers and increased air temperatures. This is clear in Figure 3, which demonstrates that as early as 2003, GVI demonstrated warmer surface temperatures than the Larsen ice shelves (Figure 3), of which several have collapsed (Cook and Vaughan, 2010). Additionally, the West AP, on which GVI is situated, experiences a high degree of warming from ocean currents due to its position in relation to the continent (Moffat and Meredith., 2018).

GVI's glaciological setting is dominated by inflows from the AP mainland along its west coast, as seen in Humbert (2007)'s model (Figure 4). From these inputs, flow direction trends down and up-channel, expanding radially from the input glaciers. These inputs accelerate ice flow towards the unusual two calving fronts of GVI, one at  $\sim 20 \text{ km}$  in the north, and one at  $\sim 75 \text{ km}$  in the south, at Marguerite Bay and Ronne Entrance respectively. Average flow rates have been modelled at  $327 \text{ m a}^{-1}$  in the south and  $25 \text{ m a}^{-1}$  in the north (Humbert, 2007). However, more recent studies have found point flow rates ranging between  $0.74$  to  $645 \text{ m a}^{-1}$  from  $72$  degrees South northwards (Mouginot et al., 2019).

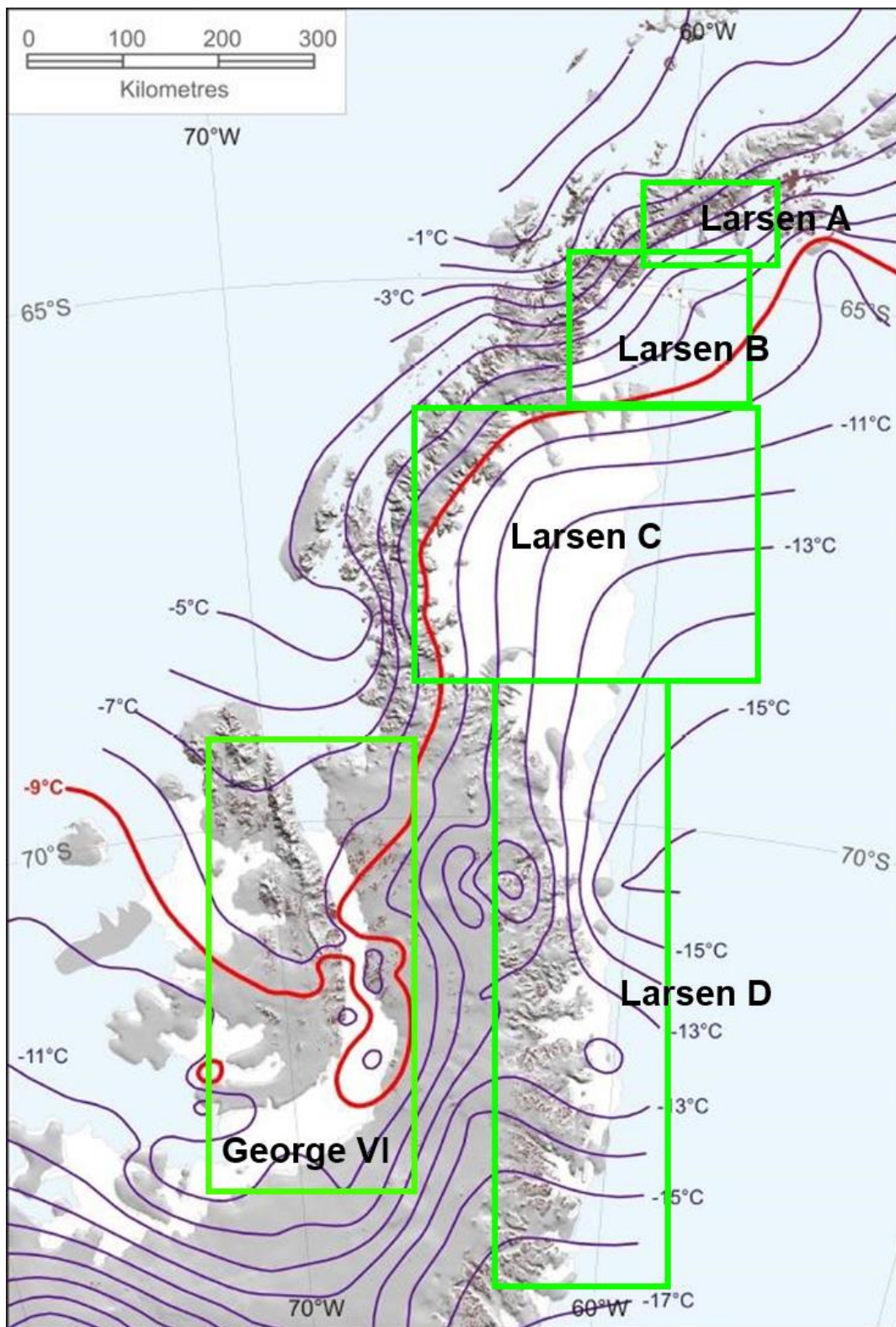


**Figure 3:** Annual average temperature isotherm map of the Antarctic Peninsula, adapted from Cook and Vaughan (2010). Red line indicates the  $-9^{\circ}\text{C}$  isotherm, extending down GVI Sound. Green boxes identify regions of Larsen ice shelves and George VI.

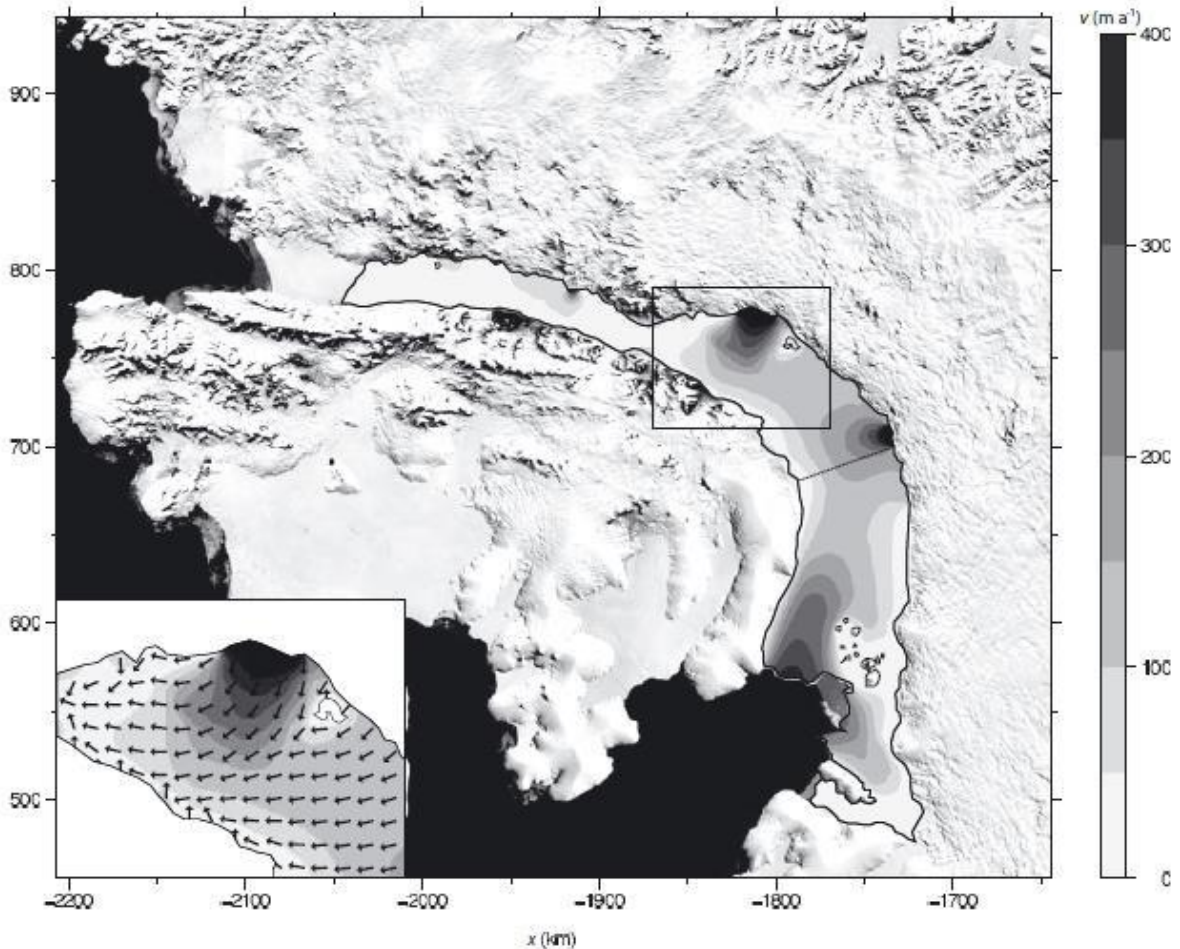


**Figure 4:** Modelled ice flow on GVI ice shelf as simulated by Humbert's flow model (2007). Flow rates increase towards the southern front, while being facilitated by inlet glaciers from Palmer Land around -1800 km\*700 km (X\*Y). Adapted from Humbert (2007). Colour ramp  $v$  (velocity) ( $\text{m a}^{-1}$ ) ranges from 0 to 400.

GVI's setting therefore has some positive impacts on its stability, as otherwise it would likely have suffered the same fate as Larsen B. As a result of this observed stability, Holt et al., (2013) concluded that currently GVI is not under threat of immediate collapse. One such point is the fact that GVI is situated within a topographic depression, thus shielding it from much of the ocean and climate's direct impacts, whilst also providing two smaller calving fronts, rather than a large fan front like most other shelves. This gives a smaller surface area for major ice-loss events through calving, and a smaller open water contact region. Furthermore, due to the modelled slow flow of ice within the northern region (Humbert, 2007), it is possible that the low ice throughput limits the degree of melting which can occur in the warmest region. This, coupled with the propensity of ice inflow from the western half of Palmer Land, suggests that the volume of ice provided to GVI may be a factor in its stability.

On the other hand, Branson (2019) suggests that GVI may be demonstrating instability due to climate, suggesting that it is possible to expect collapse in the near future, this is reflected by Holt et al., (2013), which states that this is possible if warming is to continue. One major factor that contributes to the instability of GVI, as with many ice shelves on the AP is that of föhn winds (Marshall et al., 2006). The topographic setting of GVI makes it particularly

at risk of föhn wind melting, as they flow from high to low altitude, leading to warming at the ice-shelf grounding line (Stokes et al., 2019). Due to GVI having two sides topographically constrained, this effect could be magnified. Such localised melting is suggested to be linked to the breakup of ice shelves such as Larsen B (Cape et al., 2015).

Furthermore, Moffat and Meredith (2018) identify oceanic currents as a major factor in warming on the AP, which could still have an impact on GVI due to its proximity to the Antarctic Circumpolar Current and resultant intrusions of Circumpolar Deep Water (Moffat and Meredith, 2018). The effect of oceanic warming can be seen in the waters of George VI Sound, which has shown temperatures of up to 1.1°C, 3°C warmer than the basal melting point (Talbot., 1988).

These two considerations of setting therefore put different ideas surrounding the stability of GVI forward. The impacts of both föhn winds, and oceanic currents must be understood in comparison to those effects which limit melting and ice loss. Major breakup events are therefore difficult to predict, as glaciological and climatological settings of each ice shelf differ, as GVI demonstrates clearly. As a result, in many cases the likely impacts of an ice shelf's loss are easier to identify than its likelihood of collapse - this is identified with Schannwell et al., (2018) suggesting that if GVI were to fail, global sea level would likely rise by ~8 mm due to a loss of buttressing from the ice shelf. This speedup of glacial output directly to the ocean has been observed in glaciers near the northern end of GVI, during measured retreat between 1989 and 2007 (Holt et al., 2013).

### (2.3) Supraglacial Lakes and Hydrology

SGLs have been observed on many ice masses globally, they cover extensive swathes of the Greenland ice sheet and in Antarctica are typically found on the ice shelves such as GVI (Kingslake et al., 2017). SGLs are formed when meltwater pools in an impermeable hollow on a relatively level (less than 3° slope) region of ice (Bell et al., 2018). Typically, on floating ice these form ribbon-like features (LaBarbera and MacAyeal., 2011), as the lakes are slowly advected in the direction of ice flow. An alternative method of formation to water pooling in a depression is through föhn wind induced melting, in which warm katabatic winds meet the low-lying ice at the grounding line, and ablate small, circular lakes (Branson, 2019).

Lakes on GVI have been usually attributed to föhn wind induced melting at grounding lines, particularly those on the eastern margin from Palmer Land (LaBarbera and MacAyeal., 2011). Lakes have been typically observed in two forms, en échelon - 'teardrop' shaped, bulging in the direction of ice flow - and circular or ribbon-like lakes (Branson, 2019), forming in regions of stagnation or low flow (LaBarbera and MacAyeal, 2011; Holt et al., 2013). The formation of en échelon lakes is identified as the result of 'pressure rollers', as a result of GVI's primary inputs flowing laterally across the ice shelf, rather than with the channel (Collins and McCrae., 1985). This results in the teardrop shapes along the Western shoreline of GVI. These 'pressure rollers' are described as a sinusoidal undulation in the ice shelf surface (Collins and McCrae 1985; LaBarbera and MacAyeal., 2011). Lakes have additionally been observed to migrate along the shelf at between 300 m a<sup>-1</sup>, and 760 m a<sup>-1</sup> (LaBarbera and MacAyeal., 2011), which fits in line with measurements made in other studies (Mouginot et al., 2019).

The impacts of SGLs upon the ice shelf stem from their drainage and capacity to alter the surface albedo and create a melting feedback (Box and Ski., 2007). Further impacts stem from flexural breakup, suggested to be caused through water mass loading on an ice shelf's

surface, followed by drainage or refreezing, causing the ice to flex and fracture. This has been observed to some degree on Larsen B prior to collapse, however there is limited evidence that SGLs directly cause breakup (Leeson et al., 2020). The principle of gravitational loading upon an ice shelf (Langley et al., 2016) is an important factor in the impacts of lakes on an ice mass, as suggested in Arthur et al., (2020). This is due to the repeated loading and unloading of ice shelves on a yearly basis through the formation and loss of supraglacial lakes causing flexural stresses on the supporting ice. This principle has been modelled in recent study by MacAyeal et al., (2015) as a means of understanding the entire process. Repeated flexural fracture was modelled, leading to 'traumatic' fracturing of an ice shelf and ice shelf-wide 'domino drainage'. Understanding of flexure has fuelled studies into Larsen B's collapse (Leeson et al., 2020; Banwell et al., 2013) and other ice shelves across Antarctica (Stokes et al., 2019). Lake refreezing is also significant, as latent heat is released and would likely impact the future energy budget post-melt season of the ice mass involved (Tedesco et al., 2012).

SGLs form during the melt season on many of Antarctica's ice shelves both in WA and EA (Bell et al., 2018; Langley et al., 2016). Thus, they should be studied further, as in Greenland they are associated with rapid acceleration of ice through basal lubrication from drainage on land-based ice, and breakup of floating ice tongues (Williamson et al., 2018; Tuckett et al., 2019; Banwell et al., 2014). Surface meltwater drainage through an ice shelf occurs via moulins and crevasses, the former typically forming at the deepest point of a lake where loading from the meltwater is highest (Pope et al., 2016). Other forms of drainage tend to occur supraglacially (Bell et al., 2017), through braided stream networks (Kingslake et al., 2017), including across the surface of GVI. Lake drainage tends to be observed about a week after the peak of melting on an ice shelf, with Branson, (2019) stating that the peak melt in 2017/18 was on 29/01, while the peak number of lakes are observed on GVI on 07/02. Vertical and horizontal drainage, alongside refreezing at the end of a melt season can be clearly identified through satellite imagery with a sufficiently high resolution (e.g. 30m), (Langley et al., 2016; Kingslake et al., 2017).

Vertically draining lakes shrink from the shoreline to the centre; creating a 'plughole' effect (Langley et al., 2016). The doline left by this process is characterised by concentric fractures caused by the rapid vertical drainage and subsequent hydrofracture, however it is only possible to identify these features in very high (~0.5 m) satellite imagery (Langley et al., 2016). Refreezing is characterised by lakes shrinking from the inside outwards, as an ice 'lid' forms and grows on top of each lake. Langley et al., (2016) and Banwell et al., (2013) also suggests another possibility for this, being multiple drainage phases leading to several recorded 'forms' of individual features.

#### (2.4) Lake Identification on Ice Masses

Previous studies into supraglacial lakes have utilised various methods of identifying and 'delineating' lakes, ranging from manual to automated. Branson (2019) for example, due to the smaller study area used a manual method, involving the isolation of lakes as polygons within GIS software through visual identification. This method is effective; however, it leaves room for human error and is generally time consuming due to the nature of the task. More commonly, methods using NDWI (Normalised Difference Water Index) are used.

NDWI calculations take several forms but typically require the ratio of two bands of satellite imagery. In the case of this study, Green and NIR bands are used, which is one of the 'standard' NDWI calculations (Liu, Yao and Wang, 2016). The others include NIR and MIR,

and Green and MIR. Each method here uses different bands as a means of cancelling out noise generated by surrounding features. Green – NIR NDWI methods have been previously used in remote sensing of ice (Watson et al., 2018; Gardelle et al., 2011), particularly on mountain glaciers, and have proved successful. However, in the case of Watson et al. (2018) debris and blue ice patches led to interference, requiring some optimisation of the calculation (NDWI-O). One method of approaching this is to run several versions of NDWI, such as “Green – SWIR” on S2 imagery, as this generally shows better lake identification, particularly where lakes may be shallow or surrounded by debris (Du et al., 2013; Li et al., 2013; Ji et al., 2009).

A primary issue in polar supraglacial lake delineation is that of blue ice and slush. These features can cause issues with automated lake delineation methods and lead to over and underrepresentation of lakes. Hence, alternate methods have been developed. One key method in this case is the “Blue – Red” NDWI method, (Moussavi et al., 2020). Yang et al., (2013) further exemplifies this by comparing NDWI versus NDW<sub>ice</sub> (blue – red) through worldview 2 imagery in Greenland. However, due to the variance in wavelengths of various satellite bands (ESA, 2019), each satellite requires slight changes and optimisations, with this being evidenced in Yang et al., (2013) concluding that “Blue – Red” NDWI can lead to misidentification of slush as ice.

The varying methods of NDWI within the study of glacial hydrology leads to a dilemma for each investigation. GVI ice shelf has been identified to have large portions of slush but little literature approaches blue ice on the shelf (Dell et al., 2020). As such, studies on GVI may prove to be ‘messy’ with the ‘Red – Blue’ NDWI method, and hence to minimise this, use of the more typical “Green – NIR” method may be warranted.

## (2.5) Types of Satellite Imagery

Satellite imagery has been used in the majority of recent studies on Antarctic and Greenlandic SGLs (Leeson et al., 2020; Langley et al., 2016; Stokes et al., 2019; Williamson et al., 2017; Williamson et al., 2018). Satellite remote sensing is one of the most effective ways of monitoring these lakes, as it provides continuous coverage in space and time, while having a good temporal (weekly to daily) and spatial (1030m) resolution for publicly available data. The two most commonly used types of imagery for monitoring lakes are Synthetic Aperture Radar (SAR) such as Sentinel 1 (Branson, 2019), and optical, such as the Landsat series, MODIS and Sentinel 2 (Kingslake et al., 2017). Some studies aim to focus on one or the other, while others make use of a combination of data types to produce a full picture (Miles et al., 2017). Additionally, satellite data works as a balance between spatial resolution, temporal resolution and number of bands; as stated in Arthur et al., (2020), and Leeson et al., (2013); thus outlining that an acceptable temporal and spatial resolution must be balanced to provide useful data for research.

## (2.6) Temporal Evolution

Studies of the seasonal evolution of supraglacial lakes have been key in understanding the wider effects they have on ice shelf breakup (Leeson et al., 2020; Banwell et al., 2013; 2014). However, less attention has been paid to their evolution on longer timescales, including on GVI ice shelf which has an interesting glaciological setting, being constrained by fjord walls to the East and West and with two short calving fronts to the north and south. From long-term study, patterns of glacial hydrology drainage and flow have been identified (Kingslake et al.,

2017; LaBarbera and MacAyeal., 2011), thus leading to a greater understanding of long-term change on ice shelves showing presence of supraglacial hydrological systems. Thus, methods to understand the impacts of this water can be developed and applied, in order to study future change in affected ice masses, as summarised in Bell et al., (2018), and applied in Leeson et al., (2020).

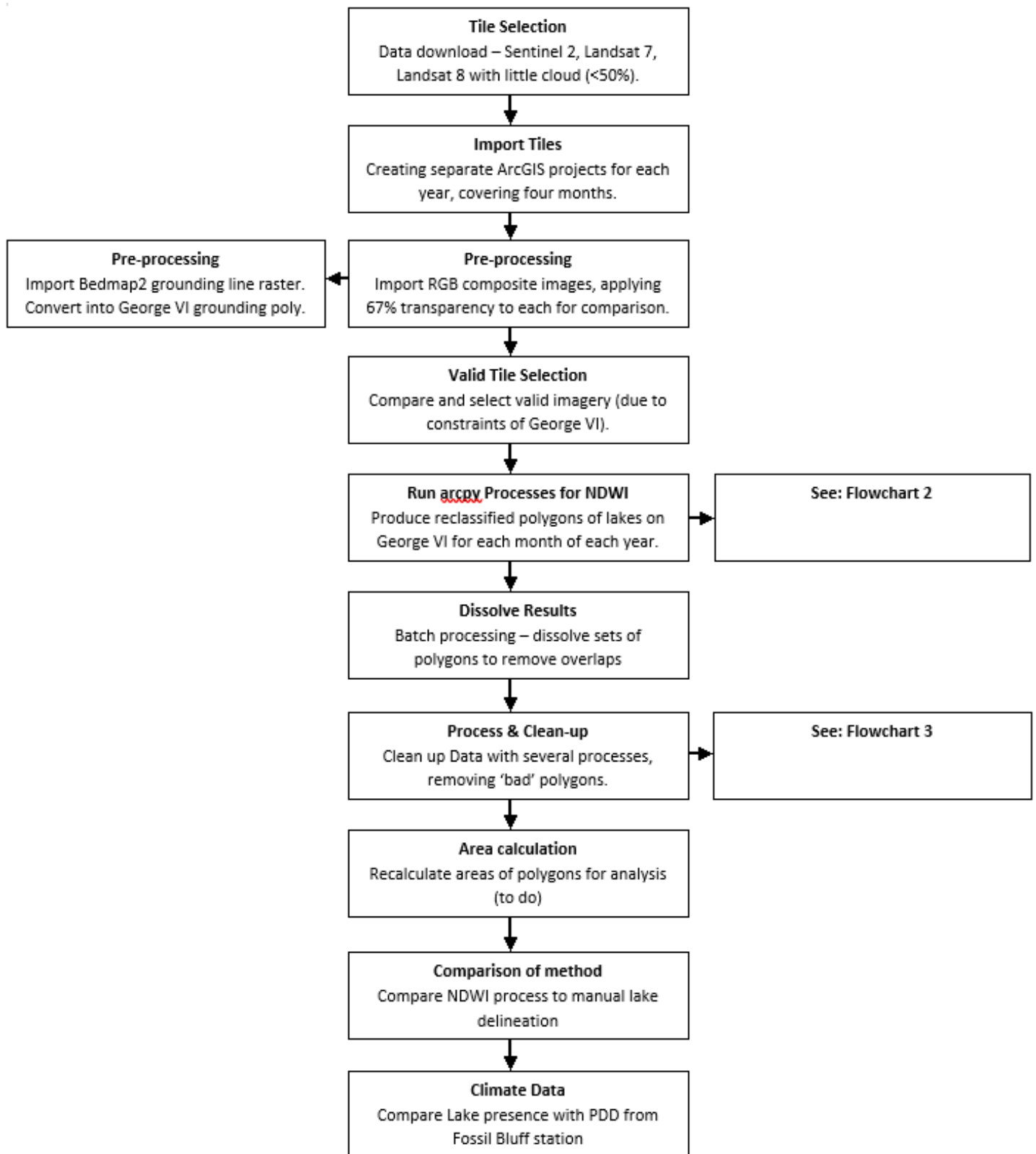
Increased temporal resolution of data is important in understanding the key processes at play with supraglacial lakes on ice shelves. Typical ice-shelf processes occur on seasonal to yearly timescales (Benn and Evans, 1998), such processes include flow rate, measured in metres per year (Mouginot et al., 2019). On the other hand, some processes, such as SGL development and drainage occur on hourly to weekly timescales (Das et al., 2008). Thus, to understand such processes in detail, a high temporal resolution is ideal. In many studies however, due to the nature of satellite imagery there are often trade-offs between temporal and spatial resolution.

Often, due to this trade-off, studies focus on either a snapshot in time, typically a single melt season as with Branson (2019), or they look at long-term changes, while foregoing temporal detail (LaBarbera and MacAyeal., 2011). Thus, a more beneficial approach would be to look at various timescales, in order to understand how long and short timescales are connected within the complex system of an ice shelf such as GVI. One such way to do this would be through collating previous studies as a review (Bell et al., 2018), while another would be to focus on a small region such as GVI and look at an increasing depth of temporal resolution, ranging from yearly to intra-seasonal. The second approach would be made more effective when combined with previous studies, to provide a comprehensive analysis of a set region. Typical states and patterns on various scales could be identified, as in Cook and Vaughan (2010); which could be used as a basis for a wider spatial study.

The inherent connectivity between imagery datasets from a combined timescale approach would allow for different types of data to be to be connected. A multi-dataset approach combining different scales of imagery, along with climatic data would therefore prove useful, and has been carried out previously in regions of Greenland (Leeson et al., 2013). For a study on GVI, data from local BAS stations and RACMO modelling would offer a means for this approach to work. Thus, the results of this would allow the identification of controlling climatic factors in specific timescales.

### **(3.0) Data and Methods**

This section outlines and discusses in detail the methods used within this body of research. Flowchart 1 outlines the basic methodology in reference to data collection, NDWI processing and climate data. Initially I address data collection, identifying where datasets were obtained including satellite imagery, regional glaciological data and regional climate data in section 3.1. In section 3.2 I outline the methods of data processing including a detailed look at NDWI processing, data clean-up and method testing. In section 3.3 I explain the methods of analysis of lake polygons, climate data, glaciological data and albedo values.



**Flowchart 1:** Shows the general order of processing for data used in this study. Tile selection involves the download and analysis of satellite image tiles in order to minimise cloud coverage. Valid tiles had little to no cloud. Where multiple existed, those closest to the centre point of each month were selected to avoid results skewing.

### (3.1) Data Collection

#### (3.1.1) *Satellite Imagery*

LS7 ETM+ (Enhanced Thematic Mapper), LS8 OLI (Operational Land Imager) and S2 MSI (Multispectral Instrument) archives were accessed via USGS EarthExplorer (<https://earthexplorer.usgs.gov>) for the melt seasons of 2000 to 2020, covering four months from December through March (Appendix 1). Landsat 4-5 (LS4-5) data was additionally used for pre-2000 imagery, taken from the years 1989-1991. This imagery was manually selected from tiles displaying little cloud-cover on GVI, as a percentage cloud cover value did not account for the topographic cloud which often forms in GVI sound. In months where several images were available, those with the closest date to 'mid-month' and each other were used. This was done to prevent skewing of results due to the short melt season, where late February imagery would be less lake-dominated than early February for example. Any periods which required the use of imagery with cloud cover were checked to keep cloud cover to a minimum, and away from typical regions of lake formation where possible, using years of high lake formation with low cloud cover as examples. The relevant bands for this study include Red, Green, Blue and Near Infra-Red (R, G, B and NIR), with a multispectral composite being made of each granule. LS7 and LS8 imagery was not pan-sharpened, as lakes are clearly visible in imagery, therefore producing a minimum pixel area of 900 m<sup>2</sup>. Due to this, minimum lake area is recorded as 1800 m<sup>2</sup>, to sit in line with 2 px being the minimum accepted size for a lake (Stokes et al., 2019). Where months were missing within the dataset, this was noted and recorded. Additionally, in years where possible, S2 imagery was used preferentially over L8 imagery, due to the finer resolution, and typically clearer imagery.

#### (3.1.2) *Regional Glaciological Data*

For this study, regional glaciological data was required, including grounding line locations, glacial surface DEMs and glacial dynamics data. Grounding line data was taken from Bedmap 2 (Fretwell et al., 2013), found at (<https://bas.ac.uk/project/bedmap-2/>). Additionally, Bedmap 2 provided an ice surface DEM at 1 km<sup>2</sup> resolution. The grounding line mask was clipped to the extent of GVI, and used subsequently to clip the DEM to the region of study identified (Figure 1). Glacial dynamics data (flow speed, direction) were acquired from MEaSURES (<https://nsidc.org/data/measures/aiv>) and imported into GIS software directly (Mouginot et al., 2019). Calculations provided in Mouginot et al., (2019) allowed for conversion of this data into flow speed from flow x and y, and flow direction raster layers. The data used here was taken from the MEaSURES Phase-Based Antarctica Ice Velocity Map, Version 1 (Mouginot et al., 2019).

#### (3.1.3) *Regional Climatic Data*

Three datasets were used, a recorded temperature dataset from the automated weather station at Fossil Bluff Station (UK Polar Data Centre, 2020), Antarctica via the UK Polar Data Centre (2019) for years 2007-20. Two sets of indirect data were acquired – RACMO, from (<https://projects.science.uu.nl>) (Wessem et al., 2017), covering 1979 to 2020 and involving temperature, precipitation and melt data for Fossil Bluff's co-ordinates; and ERA5, (<https://cds.climate.copernicus.eu>) (Copernicus Climate change Service (C3S), 2017) covering 2000-2020. ERA5 was corrected for lapse rate in line with RACMO and Fossil Bluff Station data, using the calculated lapse rate of 0.43°C per 100 m (Ambrozova et al., 2018) as observed on James Ross Island above 56 m. The lapse rate correction was applied ERA5's 328.8 m ASL elevation, and the lapse rate values in Ambrozova et al. (2018). This data was then plotted into comparative graphs to identify any systematic bias within the data.

### (3.2) Data Processing

#### (3.2.1) *Delineation of SGLs*

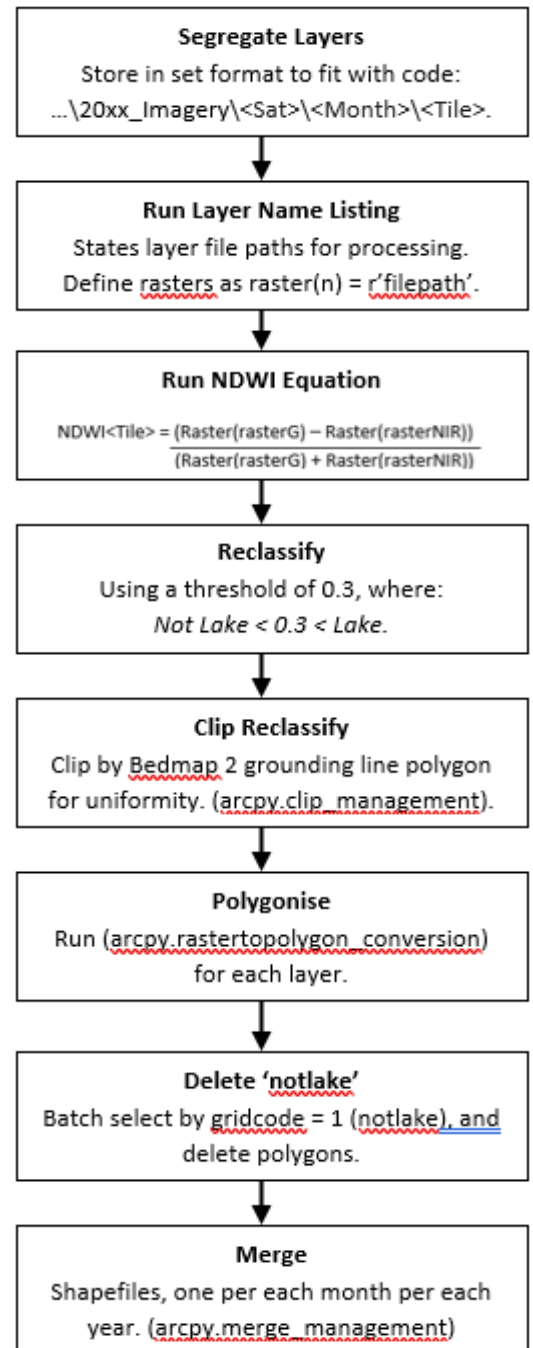
The Normalised Difference Water Index (NDWI) was used, as identified by Williamson (2017). The method used involves Green and NIR bands, as opposed to the Blue and Red bands. However, for 2015-2020 both methods were tested to prove their efficacy, with Green and NIR producing less errors in data. As such, equation 1 was used as the primary method of automated delineation:

$$NDWI = (Green - NIR)/(Green + NIR)$$

Once collected, layers were segregated and stored into a set format to ease python processing of multiple rasters. The processing chain as described here is visible in short in flowchart 2. In addition to using python, each season of imagery (Dec-Mar of a corresponding melt season) was imported into a standalone ArcGIS Pro project to prevent system slowdown from project size, hence producing a semi-automated processing method. This semi-automated method of processing was chosen due to the size of the dataset involved, with the overall polygon count before clean-up producing 1.36million polygon features across the entire timescale. Several python modules were key to this chain of processing, including <<arcpy>>, <<glob>> and <<os>> in order to make file system processing more efficient with the varying storage methods used by each satellite.

Reclassification of rasters post-NDWI was characterised by a set threshold. Previous studies have identified a threshold for “lake” versus “not lake” values of between 0.2 and 0.5, depending on the region of Antarctica under study. As such, the threshold for this study was found through interactively running the reclassification on 2020 imagery, increasing incrementally, which settled on a threshold of 0.3 for the most accurate data, with the fewest false classifications (Appendix 2). Post-reclassification, the raster was clipped to the grounding line from Bedmap2 (Fettweis et al., 2013) and polygonised, with “not lake” values were removed.

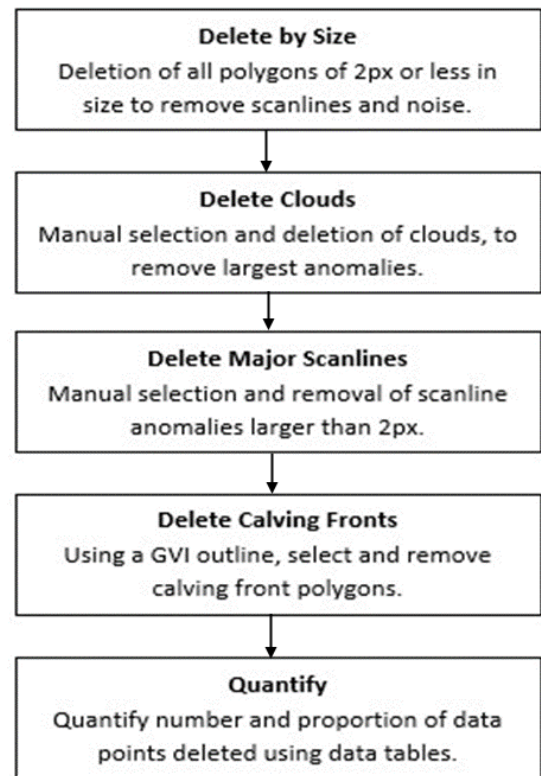
Polygons were then grouped using the built-in merge and dissolve functions within ArcGIS Pro. This produced a polygon layer for each month of each year between 2000-2020 where data was available, while the dissolve function ensured there were no overlapping features. Additionally, NDWI was run on 1989-1991, then manual delineation was applied due to the low frequency of imagery and relatively high levels of cloud cover. The resulting layers were then imported into a new project, allowing inter-year and well as intra-year comparisons. This process was carried out manually rather than using python, however following the same steps as described in Flowchart 1, through use of ArcGIS Pro tools on Landsat 4-5 imagery.



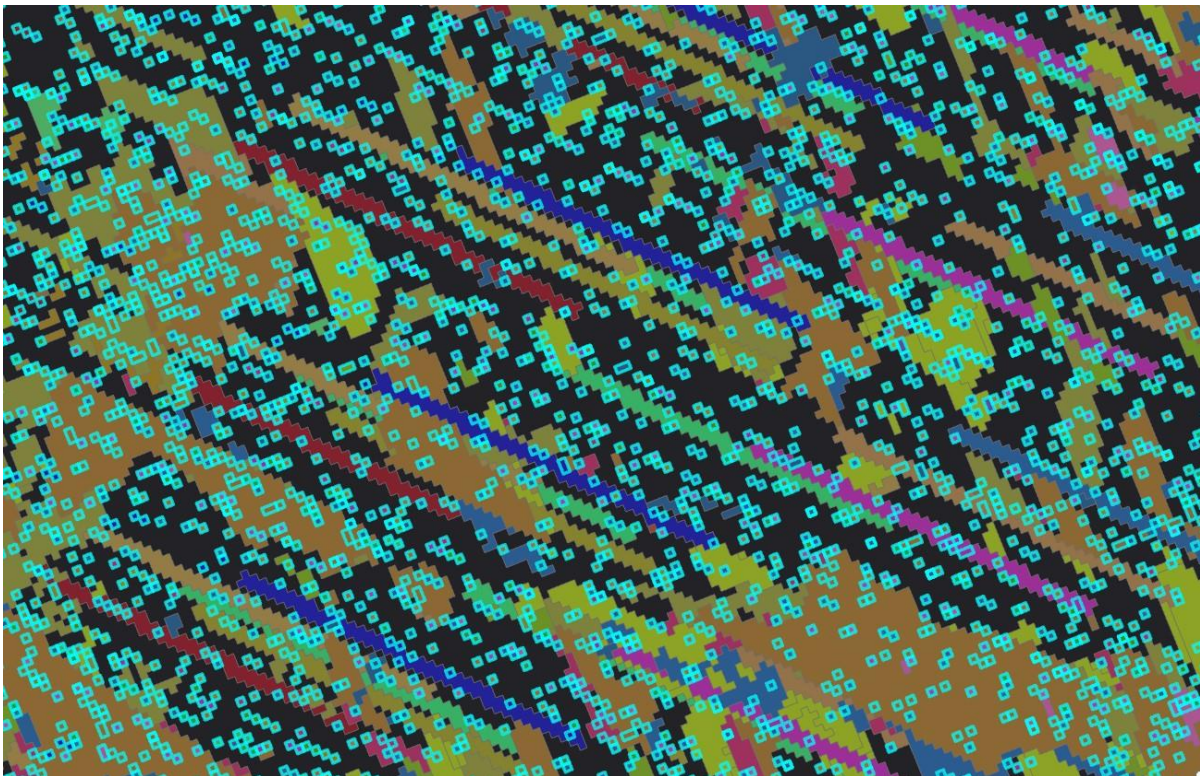
**Flowchart 2:** Python processing chain for each individual raster tile in order to produce polygons of each lake on GVI.

### (3.2.2) Data Clean-up

Several clean-up processes were required (flowchart 3). The primary method was to remove all polygons smaller than 2 pixels in size, as identified by Stokes et al., (2019). This limited the minimum lake size to 1800 m<sup>2</sup>, and was kept uniform between both Landsat and Sentinel data. This had the additional benefit of removing some anomalous scanline points (Figure 5a, b), produced by imagery bands not completely overlapping. The count of polygons removed, along with the area removed was quantified (Appendix 3).



**Flowchart 3:** Displays the required data clean-up due to inherent 'features' of the associated data.



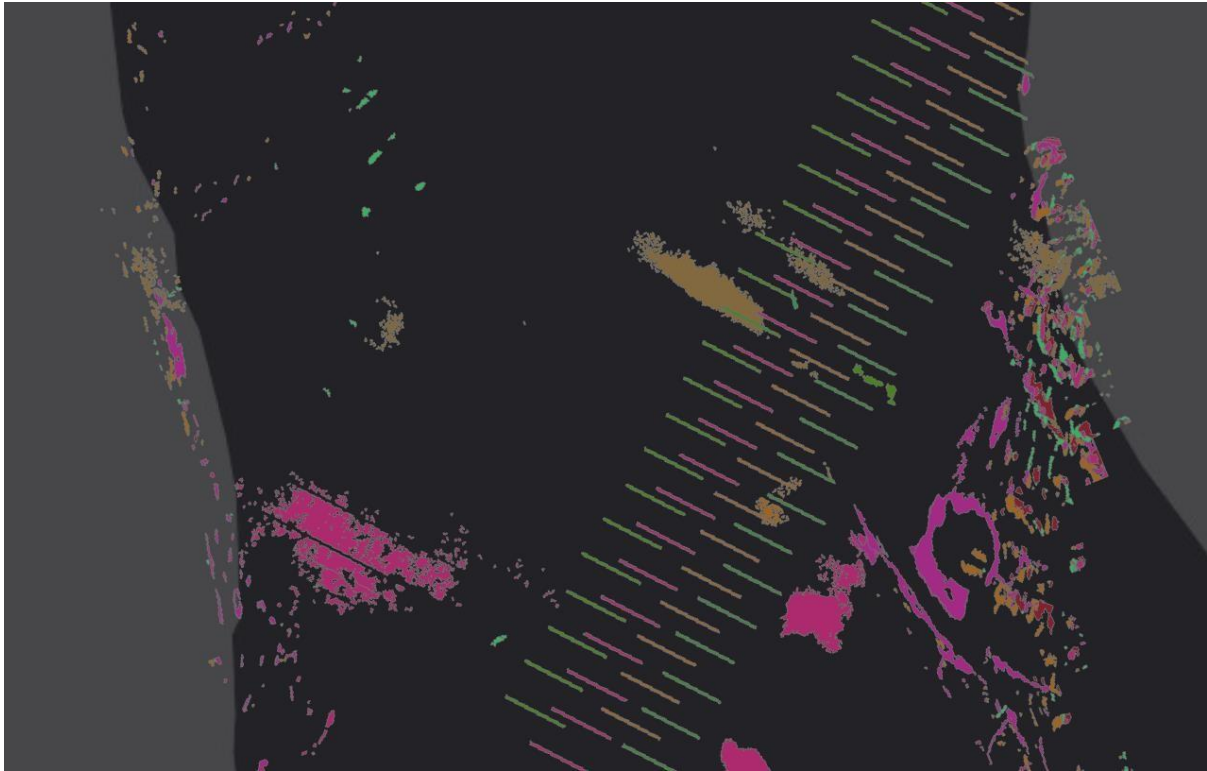


**Figure 5: (a)** Removed ‘small polygons’ (cyan outline), many of which are a component of incorrectly overlapping band layers from satellite imagery. Scale: 1:25000 at ~71.059°S 67.950°W **(b)** Scanline anomalies and large areas of cloud detected erroneously by the NDWI calculation, these were cross-referenced with imagery and removed. Scale: 1:100000 at 71.589°S 68.384°W; 71.380°S 67.533°W (SW;NE).

Once small polygons were removed, clouds and any residual features identified as bedrock were compared with corresponding imagery and deleted (Figure 5b). Clouds were the primary feature which caused data corruption, and were the focus of removal, while bedrock features typically appeared in the same location year on year, allowing for a more simplistic “blanket” removal. These features were all removed manually, in order to prevent any removal of lake features by automated methods or a cloud mask removing polygons overlain by cirrus cloud. Calving front anomalies (cracks, open water) were additionally removed manually, however few of these anomalies were present.

The final, most intensive component of clean-up was that of scanlines (Figure 5b). These were an artefact of the scanline anomalies produced due to a fault with the LS7 ETM+ sensor, creating streaks where differing bands align incorrectly and create overlap, emerging as the polygons shown. Correction for this, according to USGS (2003) results in the loss of 22% of data (USGS, 2003). Scanline anomalies were removed manually to ensure no overlapping lake features were deleted. Where lake features overlapped these anomalies, a polygon snipping tool was used to extract the scanline anomaly from the associated polygon.

The data loss as a result of scanline anomalies (and the corresponding missing data due to the extended scanlines) was quantified in order to produce a ‘data loss factor’, comparable to the average data loss stated by USGS (2003). LS7 rasters for three years were taken at random and reclassified with NoData (scanlines) as “1”, and Data as “NoData”, producing scanline masks. These were then polygonised and superimposed onto polygon layers for 2017-2020. The scanline masks were then used as a clip mask for the 2017-2020

polygons, and statistics of total area were generated for each set of lake polygons. This was then converted to a percentage change value between the original area, and the LS7 masked area, producing a data retention percentage of 77.6% (or 22.4% lost), close to the USGS value (Appendix 4). Overall, 89% of polygons were removed (Appendix 3).

### (3.2.3) Method Testing

Methods were tested for efficacy through several means. G – NIR NDWI was compared to R – B NDWI using the January and December imagery from 2020's melt season, as this was typically the clearest data with large quantities of lakes present. The python processing chain (flowchart 2) was carried out for both equation 1 and equation 2:

$$NDWI = (Blue - Red)/(Blue + Red)$$

Thus, producing a second set of NDWI raster layers. This was additionally carried out for both LS8 and S2 data over the same period, allowing for detection of differences based on each satellite. The produced polygon layers were then overlaid onto the corresponding multiband imagery for each period, and polygon symbology was adjusted to show where each method correlated. This was then studied visually to identify which dataset produced the highest number of false results. Once the method denoted by equation 1 had been selected, the LS8 and S2 polygons were both compared, allowing for testing of the value of each dataset, and the same visual analysis was carried out.

Method testing was also carried out to compare the efficacy of NDWI versus manual delineation. Despite the large dataset, a baseline was required to evaluate the value of NDWI delineated lakes. Thus, a set area of 5 km<sup>2</sup> was selected within the centre of the ice shelf, corresponding to a randomly selected grid square in the ArcGIS Pro display. Imagery tiles corresponding to January & February of 2018 (S2) and 2009 (LS7) were selected, ensuring that roughly 100 lakes were present within the 5 km<sup>2</sup> area. The lake features were then manually delineated using ArcGIS's polygon creation tools by two different individuals and compared with polygons from the tiles' corresponding NDWI results. A visual comparison was made (Figure 6), and combined with a quantitative approach, through exporting polygon data for the 5 km<sup>2</sup> region into a spreadsheet. The count, total area, mean area, max area and min area were accounted for and compared. This was then used to compare manual versus semi-automated methodologies.

Climatic data was compared with Fossil Bluff automated weather station being treated as a true reading of local air temperatures. RACMO and ERA5 temperature data was thus tested against data produced by BAS at Fossil Bluff. Data was compared to find systematic bias and any noticeable variance in results (Appendix 5). The understanding of systematic bias in climatic data for the region originates from literature (Leeson et al., 2017) which identifies systematic biases in RACMO temperature data for Larsen B. Bias found in RACMO data suggests that temperatures trend low, between 2-5°C lower than recorded values (Figure 7a), while ERA5 temperatures fall much closer to the recorded value (Figure 7b). Hence, ERA5 temperature data was concluded to be more useful than RACMO temperature data due to the closer agreement with recorded data, this does not mean however, that RACMO shows systematic bias when considering precipitation and melt values. Furthermore, systematic bias within the RACMO data used appeared consistent across the temperature range, with summer and winter bias having the same range in values.

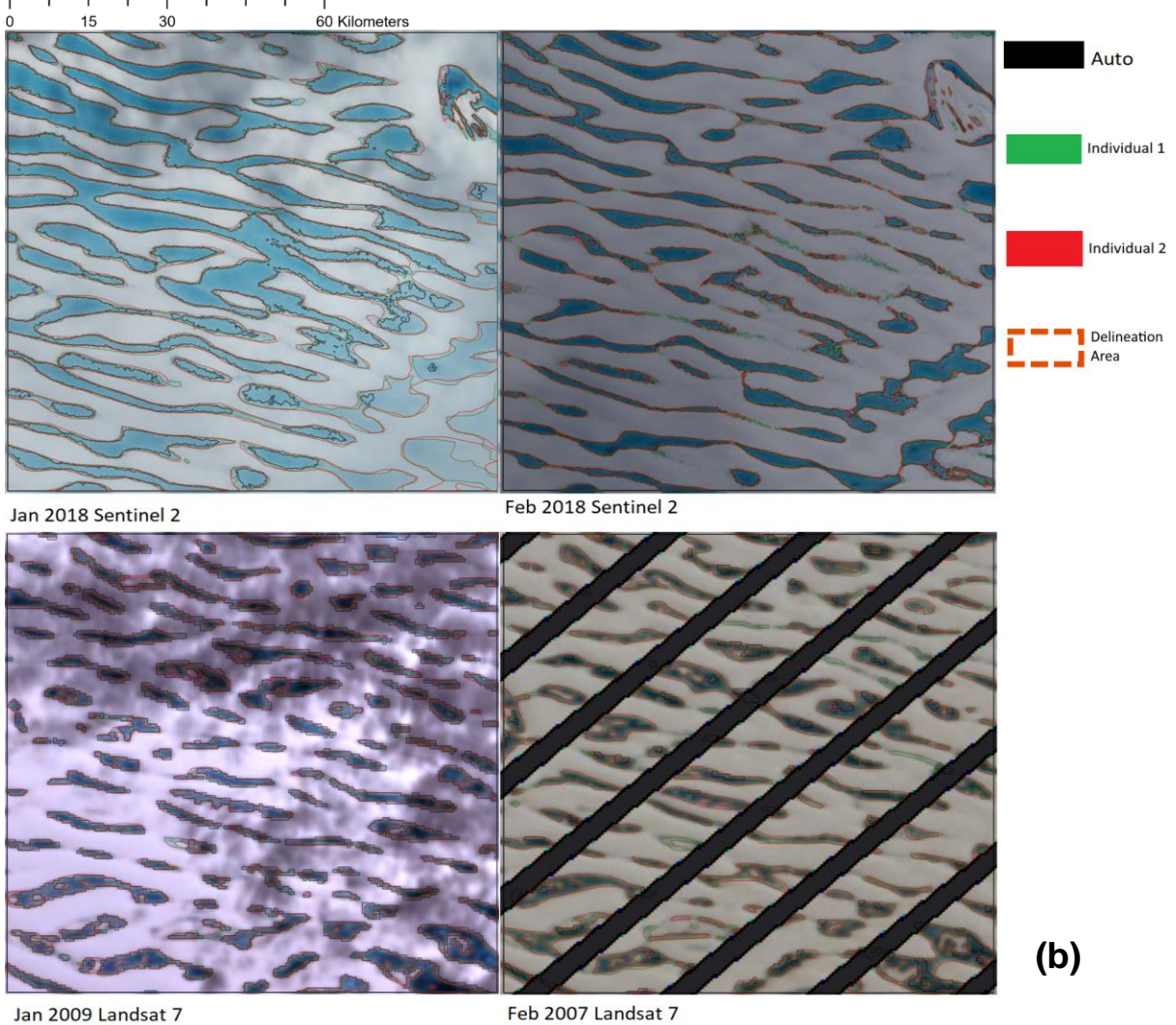
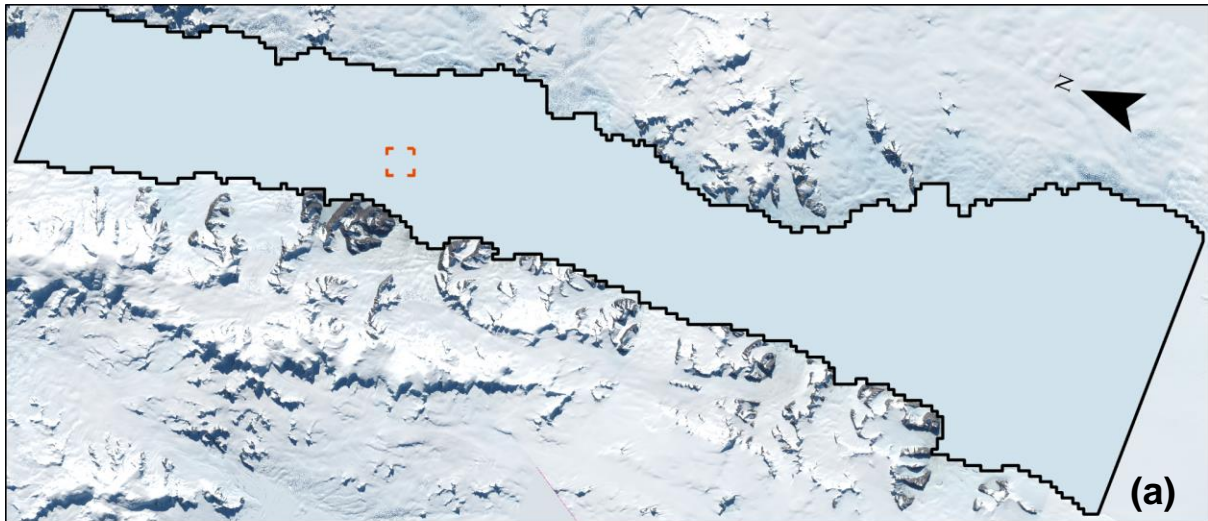


**Figure 6:** (a) Location map identifying test area within the study region. (b) Output polygons from the manual delineation methods versus automated NDWI. Automated is shown in black, Individual 1 is shown in green and Individual 2 is shown in red. Some clear discrepancies can be observed, particularly in the January data due to shallow lakes.

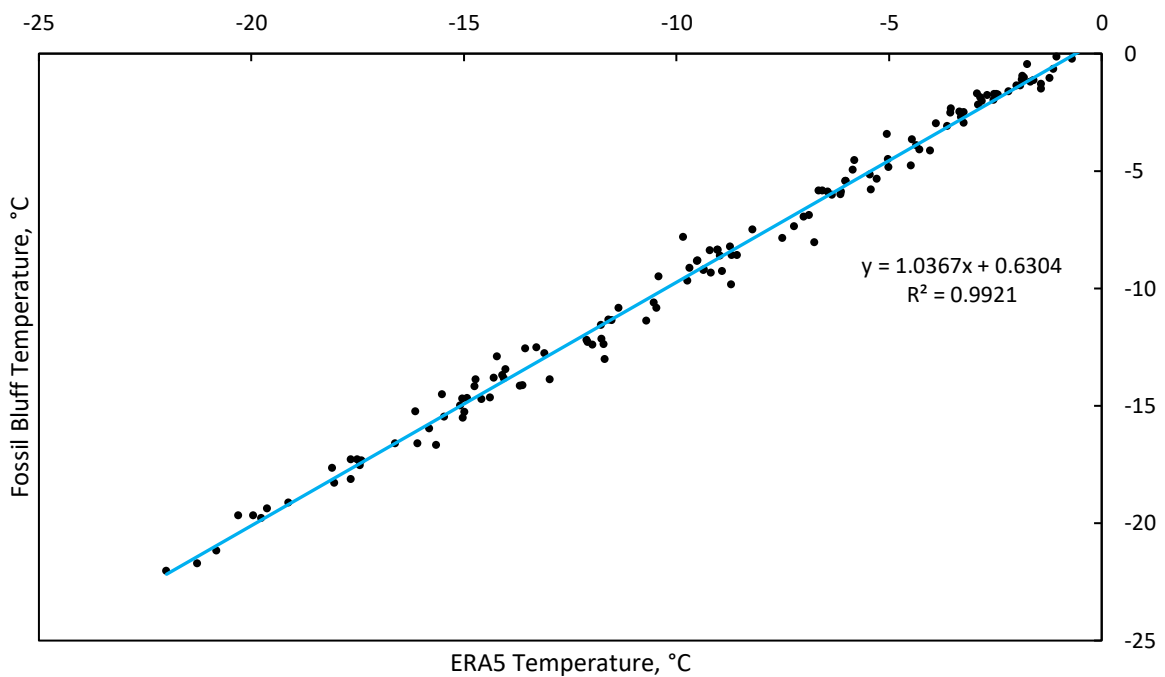
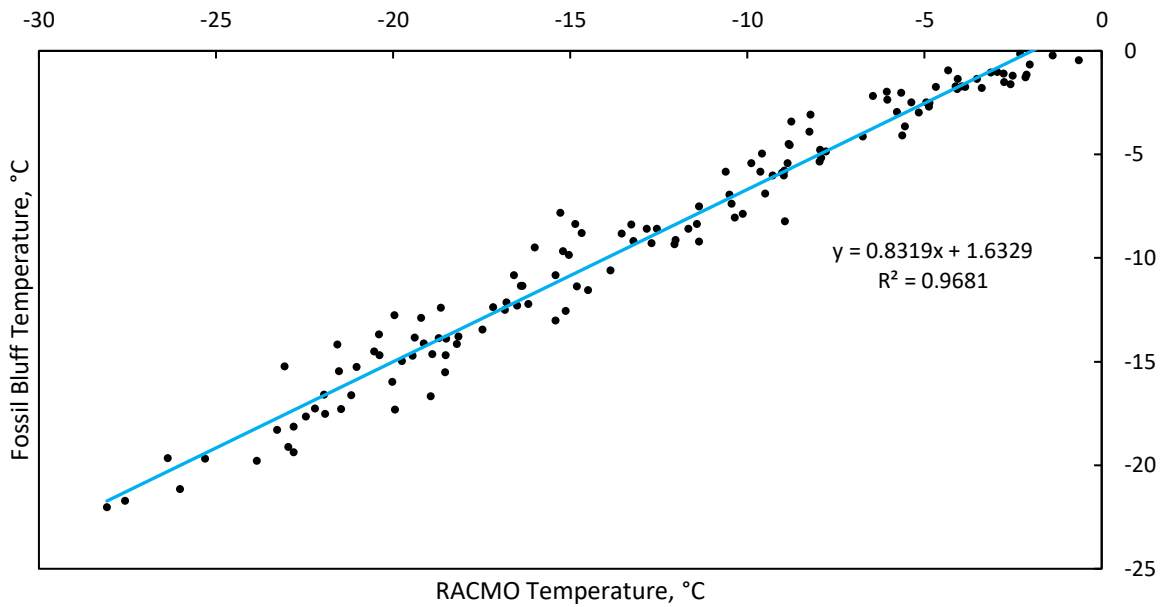


**Figure 7: (a)** Relationship between RACMO (x axis) and recorded monthly mean temperature values (y axis), RACMO trends lower than recorded values, with a strong correlation, but some variance. Years involved in study cover 2006/07-2016/17 melt seasons. **(b)** Relationship between ERA5 (x axis) and recorded monthly mean temperature values (y axis), ERA5 trends similarly to recorded values, with a stronger correlation than RACMO. Years involved in study cover 2006/07-2016/17 melt seasons. This relationship is further documented in Appendix 5.

### (3.3) Data Analysis

#### (3.3.1) *Polygons and Imagery*

Polygons were clipped to a test region corresponding to the coverage of the Sentinel 2 tiles “T19DEA” and “T19DEB” across GVI, producing a total ice shelf study area of 6776.22 km<sup>2</sup>. This was to provide a focus region for the study, and from overviews this region was identified as the most active part of GVI Ice Shelf, as most identified lakes would appear here. Additionally, this corresponded closely with the -9°C isotherm’s extension into GVI (Cook and Vaughan, 2010). Within this region, lake statistics were gathered, identifying average lake area, total lake area, lake volume and lake count for each combination of month and year. These statistics, taken from the attribute table of each polygon layer were exported to .csv and collated into a spreadsheet document for further analysis. The results were further processed in this document, providing full-season totals from the monthly data. Percent of ice-shelf covered by lakes (lake density) was additionally calculated for each year by subtracting the total lake area covered in each month from 6776.22 km<sup>2</sup>, and then converted to a percent value for each month, and season.

The proportion of lake types was estimated for 2020 via close inspection of February imagery. As the definition of a ‘ribbon lake’ is not easily defined within GIS software, due to irregular shapes and interconnectedness of these features, manual visual observations were used to differentiate between ‘ribbon’ and ‘globular’. Lakes which were at minimum 2-3 times longer north-south than their east-west width were determined as ‘ribbons’. Globular lakes were those more circular or regular in shape, while outliers that were ‘wider’ than their length, were identified as ‘arcuate’, a form of transverse ribbon lake feature.

During processing, total lake area was determined to be the most useful metric for the areal dimension of lakes, as lake mean area was corrupted by both LS7 scanlines dividing large features; and singular pixels in NDWI causing lakes to be connected where other methods may identify them as separate. As such, lake mean area is only comparable between images from the same satellite, while total lake area can be corrected for LS7 faults and made wholly comparable.

While lake areas and count were taken directly from statistics automatically generated by GIS software, lake volume was calculated for all lakes of 2015-2020 as these had the lowest propensity to scanline corruption due to the lack of LS7 data. Lake depth was calculated using the radiative transfer model (Sneed and Hamilton, 2007; Box and Ski, 2007), as demonstrated by equation 3:

$$z = \frac{\ln(A_d - R_\infty) - \ln(R_z - R_\infty)}{g}$$

Where  $z$  is depth,  $A_d$  is bed reflectance,  $R_\infty$  is reflectance from scattering in the water column,  $R_z$  is the pixel reflectance value and  $g$  is the attenuation co-efficient (rate of scatter and absorption within the water column). Once depth was calculated, volume was found by multiplying the mean depth by total area of each lake polygon. Once all data was collated and processed to produce seasonal averages, these data were graphed, with timeseries graphs

being produced alongside scatter plots of lake area and volume for 2015-2020, and histograms of lake volume. Uncertainties have been found in depths below 3 m (Box and Ski., 2007) but between 3-10 m, depth values however agree with measurement in previous studies (Pope et al., 2016). Additionally, depths of below 0.1 m are considered unrealistic, and hence lake depths were assumed to have a 0.1 m minimum value.

Additional processing was required to produce a “frequency of formation” layer, ie. displaying the frequency at which a lake would form in a set region of the ice shelf. Polygons were collated to produce a “seasonal maximum” layer for each year from 1999/2000 to 2019/20, then converted to raster, producing 21 unique layers. These were then reclassified, where lakes would return the value “1” and no lake presence would return “0”. These rasters were then added together, producing a raster with values of 0 to 21, and reclassified once more so “0” returned a “NoData” value. This was then returned to vectorised polygon format and a colour ramp was applied. Thus, the frequency of lake formation per area was made visible.

Drainage features such as dolines were identified using manual visual methods, by direct manual observations of imagery at a large scale ~1:50000. Specific characteristics were looked for including shadow, basin streaks, persistence outside of the melt season and concentric lakes surrounding the feature. These observations were carried out for 2020, 2000 and 1991 in detail, while intermediate years were checked for new features forming where possible. During 2020, imagery from Landsat and Sentinel was compared in order to confirm the existence of a doline, versus artefacts in satellite imagery.

### *(3.3.2) Glaciological Data*

Elevation, velocity and flow direction rasters were taken and clipped to the extent of the study region using the clip raster tool. In turn, the elevation raster colour ramp was limited between 9 – 99 m, encompassing the region’s entire elevation profile. The flow speed and direction rasters were clipped similarly, with the colour ramp of velocity being limited between 0 – 645 m a<sup>-1</sup>. Hence, this produced comparative raster layers, upon which lake polygons could be overlain. This allowed for visual comparison between lake frequency polygons, elevation, flow direction and flow speed. Additionally, the relationships between formation frequency, elevation and velocity were quantified using spatial correlation tools in GIS software.

### *(3.3.3) Climate Data*

Climatic data, once processed as above, was coupled with the lake area and volume data. Average temperature, total melt and total precipitation were plotted on a timeseries, from 2000 to 2020. Therefore, allowing for comparisons between the impact of climate on lake formation. This was repeated through comparing summer and winter averages with lake area, to provide a narrower scale approach. Temperatures from differing sources were additionally plotted on scatter charts alongside one another in order to identify any systematic variance in the data collection methods, and to produce a more ‘complete’ dataset where some was missing. Furthermore, temperature data for 1979-2020 was used to produce 10 year averages of temperature, allowing for analysis of decadal cycles such as the southern annular mode (Marshall et al., 2006; Turner et al., 2016).

A multivariate regression analysis was carried out on the climate data in order to identify primary controlling variables in lake formation (Appendix 6). The variables included in analysis were seasonal precipitation totals and averages, seasonal temperature positive degree days. These values were calculated against lake densities to identify significant correlations between each variable.

#### (3.3.4) Impact Estimation of Albedo

Methods of identifying impacts of lakes on albedo were derived as a means of linking observations of lakes to a 'real' representation of their impacts. The first method used an equation based on the assumption that melting at the base of supraglacial lakes is roughly double that of the surrounding ice (Leeson et al., 2015; Tedesco et al., 2012). The equation takes lake area and lake albedo to produce an impact value, Equation 4:

$$\left( \frac{\dot{\alpha}_{ice} * A_{ice} + \dot{\alpha}_{lakes} * A_{lakes}}{A_{total}} \right) - \left( \frac{A_{ice} * A_{total}}{A_{total}} \right)$$

Where  $\dot{\alpha}_{ice}$  and  $\dot{\alpha}_{lakes}$  are ice and lake melt rates,  $A_{ice}$  and  $A_{lakes}$  are ice and lake areas and  $A_{total}$  is the total area of study. This produced an impact value, corresponding to lake density across the area of GVI, which estimates the impact which supraglacial lakes have on the ice shelf. This calculation was carried out for the years 2014-2020 to produce a representative sample without using LS7 data.

#### (3.3.5) Reflectance Calculation of Albedo

A second approach was taken to produce values direct from the observed data. This was done through use of ArcGIS Pro and S2/LS8 tiles. First, top of atmosphere (TOA) reflectance was obtained, with S2 data providing this directly in L1C products, the LS8 data required converting using guidance provided in Ihlen and Zanter (2019). Once gathered, the GVI grounding line mask produced from Bedmap2 was used (Fretwell et al., 2013), and copied for each of the years 2014-2020. The R, G, B and NIR satellite tiles were then stitched together using a mosaic tool, producing four rasters for each year. Over this, a zonal statistics tool was run to produce mean values of reflectance for each band across the entirety of GVI, including lakes. Once this was gathered, lake polygons were cut out of the Bedmap 2 produced overlay for each year, and zonal statistics were re-calculated, producing new mean values with the reduction in reflectance from lakes removed.

Using the calculated reflectance of "lakes" and "no lakes", a percentage change between these two was calculated, and averaged for each band to produce a mean change in reflectance value. thus showing the impact on GVI's reflectance lakes have. From here, ERA5 corresponding monthly snow albedo values (C3S, 2017) were taken and each had their corresponding percentage change applied, to represent when accounting for the specific lake presence of each year. This therefore produced an accurate change in albedo for the region of GVI based on ERA5 data.

## **(4.0) Results**

Here I present the main findings of this research: in section 4.1, I address climatic controls on SGLs, at the inter-annual scale in 4.1.1 and intra-annually in 4.1.2. In 4.1.3 I explain the observed relationship between climate and SGLs prior to 2000. From there, controls on lake variability from a glaciological perspective are addressed in section 4.2, covering ice flow and elevation characteristics. In section 4.3 I outline findings with respect to lake drainage, or lack thereof on GVI. Finally, in section 4.4 I address the calculated values for albedo across the GVI ice shelf in correspondence to lake density and other relevant values.

### **(4.1) Climatic controls on Lake Formation**

#### *(4.1.1) Inter-annual Variability in Lakes and Climatic Influences*

Between 2000 and 2020, annual maximum lake covered area on George VI is highly variable (Figure 8). Lakes do not form at all in 2014, yet cover 11.83% of the ice shelf in 2020. Between 2000 and 2010, maximum lake area increases at an average rate of 0.75% per year, reaching a peak in 2010 of 9.2%. Between 2011 and 2018 however, lake covered area is consistently low (1.72% on average) and is near-zero in 2019. Refrozen lakes can be seen on the ice shelf in 2019 through visual inspection. It is not clear however whether these were open water lakes that formed and froze through between image acquisitions, or whether they were relics from the previous melt season, revealed as snow cover was removed

Mean lake depths on the day when lakes are most abundant each year range from 0.43 m (2020) to 0.86 m (2016), while annual maximum depth values range between 3.1 m (2017) and 4.8 m (2016). These lake depths are comparable to those on the Larsen-B ice shelf before it collapsed, reported to be between 1 m – 4 m in 2000 (Banwell et al., 2014). Annual maximum lake depth does not change significantly on GVI between years, despite the large variations in lake area, with  $R^2$  values between these two variables ranging between 0.000134 (2020) and 0.008629 (2019). In 2017 for example, lakes only formed in the North-West of the ice shelf, but had a maximum depth of 3.1 m. This is not notably shallower than lakes in the highest melt year, 2020, when maximum lake depth was 3.5 m.

There is no trend in either winter mean temperatures or summer mean temperatures between 2001-2019 inclusive. This lack of trend is further reflected with PDD values showing no significant link to lake density. Average summer mean temperature was  $-4.3^{\circ}\text{C}$  ( $\sigma = -0.92^{\circ}\text{C}$ ) and average winter mean temperature was  $-13.3^{\circ}\text{C}$  ( $\sigma = -1.20$ ) during this period. Annual maximum lake density is not strongly correlated with either summer mean temperature ( $R^2 = 0.165$ ;  $p = 0.48$ , Figure 9b) or winter mean temperature ( $R^2 = 0.013$ ;  $p = 0.96$ , Figure 9c). However, the coldest summer on record (2014,  $2.4\sigma$  colder than average) and the warmest summer on record (2020,  $2.7\sigma$  warmer than average), have the lowest and highest lake density during the study period, respectively. Interestingly, whilst 2010 had the second highest lake density in the 2000-2020 record, it had a fairly cold summer ( $0.6\sigma$  cooler than average). Lake abundance is thus not a linear function of temperature on George VI, with these findings holding for shorter-term datasets from the AWS at Fossil Bluff and the RACMO model.

Similar to temperature, total seasonal melt (ERA5, m of water equivalent taken at Fossil Bluff, -68.28E, -71.33N) shows little relationship with lake density. Furthermore, winter precipitation shows no relationship on an annual scale with lake density. However, there are some exceptions, as 2010 shows a low value of prior winter precipitation. Additionally, 2017 shows an extreme peak in precipitation from the prior winter, yet no significant lake presence. The low summer and low winter precipitation in 2010 both correspond to a high peak in lake formation. Summer precipitation shows a weak but significant correlation with lake density, both from mean and total values (mean:  $R^2 = 0.21$   $p = 0.04$ ; total:  $R^2 = 0.51$   $p = 0.001$ ), this was reflected through multivariate regression analysis. Total precipitation additionally shows a greater correlation with lake density than mean precipitation. As such, summer precipitation shows that to a degree it has influence over lake density on GVI.

Spatially, clusters of lakes tend to form in patterns that are largely in-line with those discussed in prior studies (Collins and McCrae 1985; LaBarbera and MacAyeal., 2011; Mouginot et al., 2019). Lakes form in a 'globular' style along the eastern side of the shelf, evolve into east-west 'bands' across the surface, and end as elongate 'ribbons' in a north-south orientation along the western side of the ice shelf (Figure 11). Lakes consistently form in the North-West of the ice shelf, around Ablation Valley, even in years with low lake coverage (e.g. 2008 and 2017). Here, lakes typically have a ribbon-like appearance, in common with much of the rest of the lakes along GVI's western margin, with lakes forming frequently even on low-melt years. Ribbon lakes are the most common form of lake present on GVI, as ribbon and arcuate lakes make up ~80% of features, while globular make up approximately 20% in 2020. Additionally, lakes form in the same regions year on year, with years that experience more lake formation showing full coverage as seen in Figure 11.

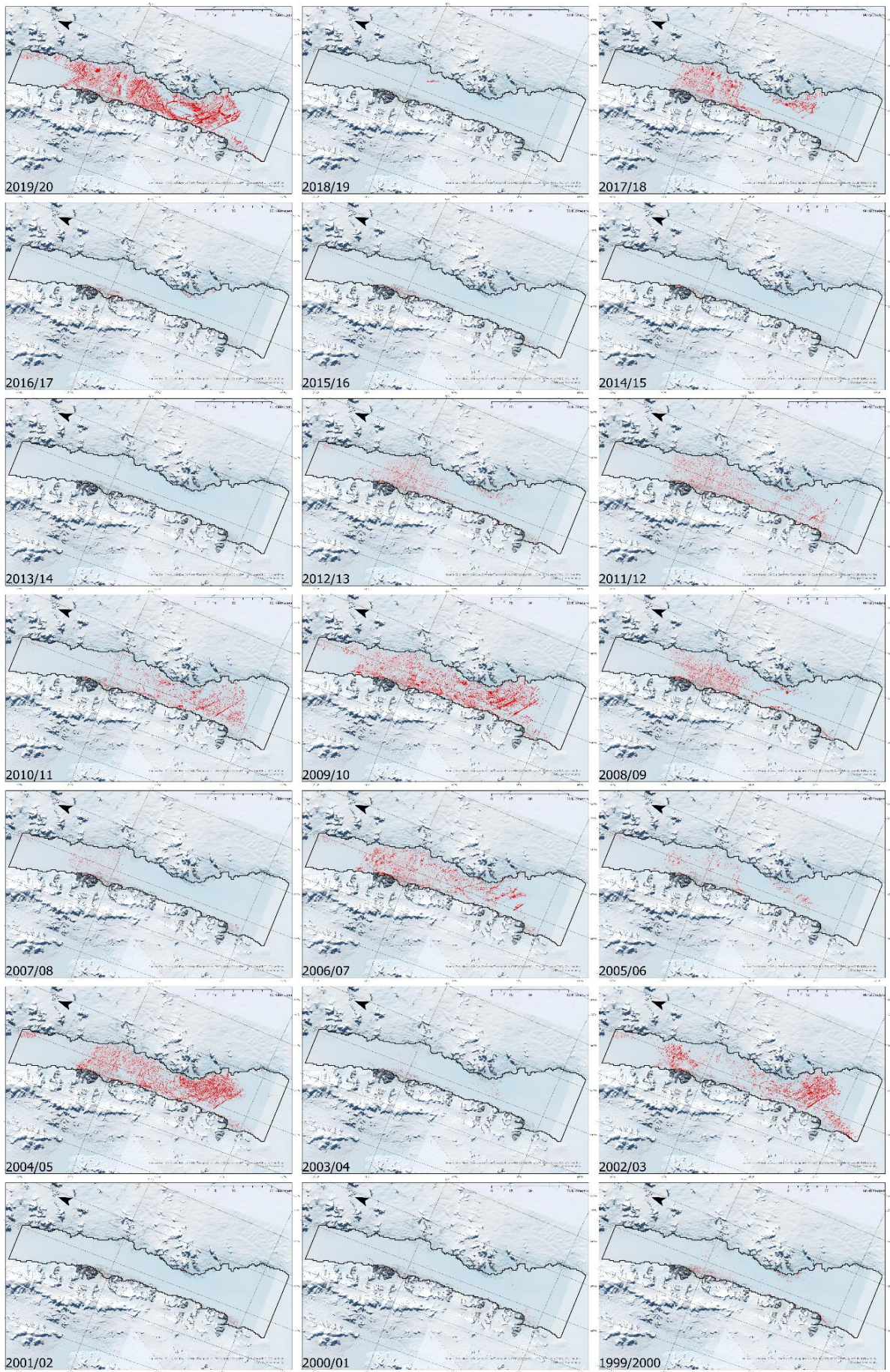


**Figure 8:** Annual maximum extent of lakes on GVI Ice Shelf in each year of analysis (2000-2020, where year relates to the year in which January and February of the DJF melt season occurred). Red polygons show lakes. Background is S2 imagery, comprised of cloud-free tiles from the 2016/17 melt season (ESA, 2019). Grounding Line, and study area limits (Black) outline produced from Bedmap2 data (Fretwell et al., 2013). Full size images can be found in Appendix 7.

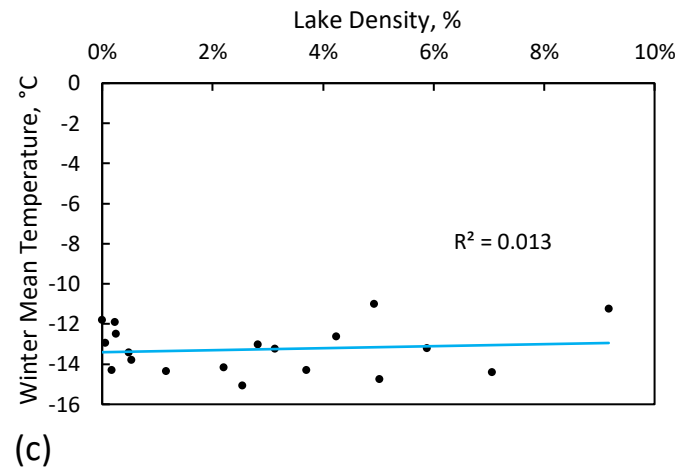
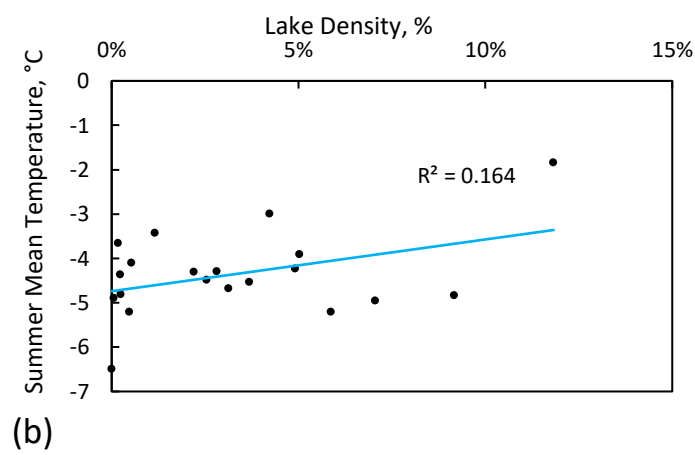
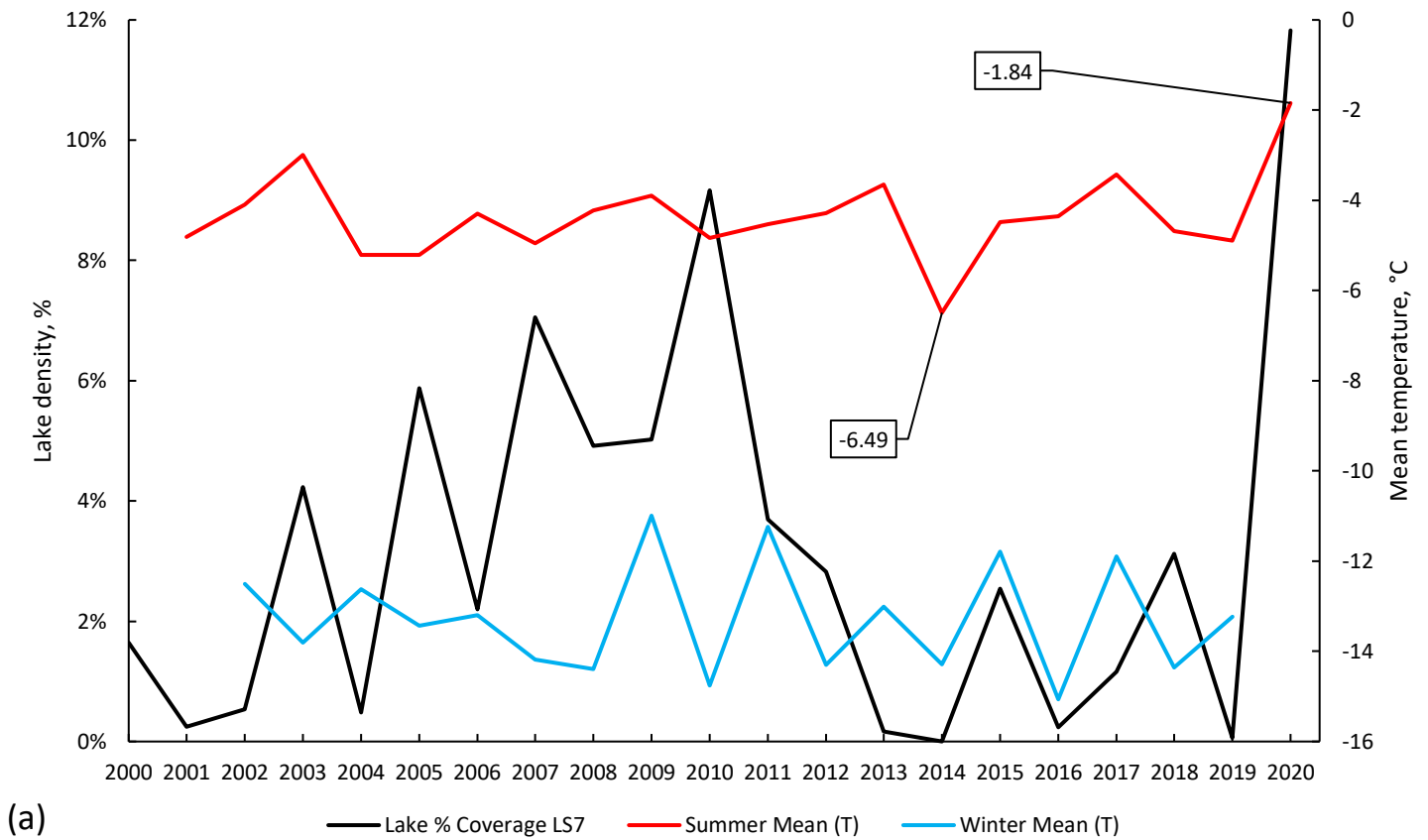


**Figure 9:** (a) Annual maximum lake density on GVI between 2000 and 2020 (black). Mean annual winter temperature from the year prior to the melt season ERA5 (blue). Mean annual summer temperature from ERA5 (red). (b) Mean summer temperature from ERA5 vs annual maximum lake density. (c) Mean winter temperature from ERA5 vs annual maximum lake density.

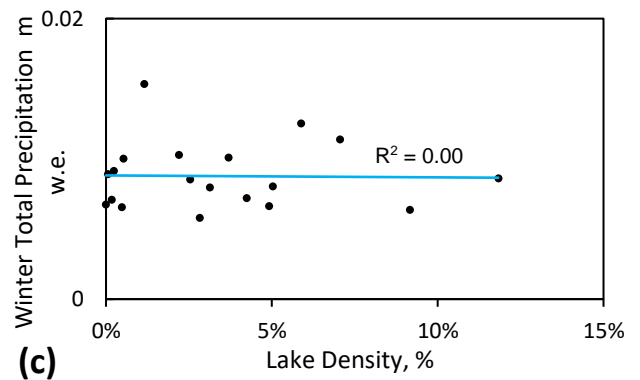
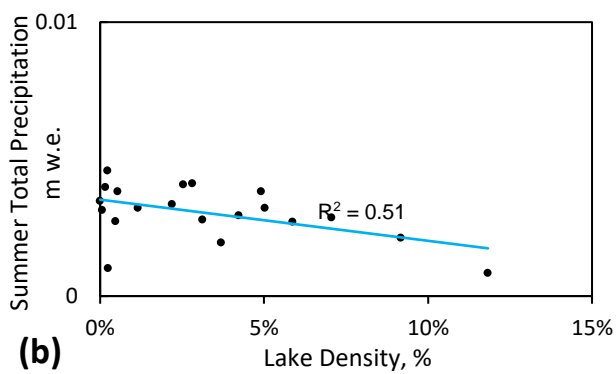
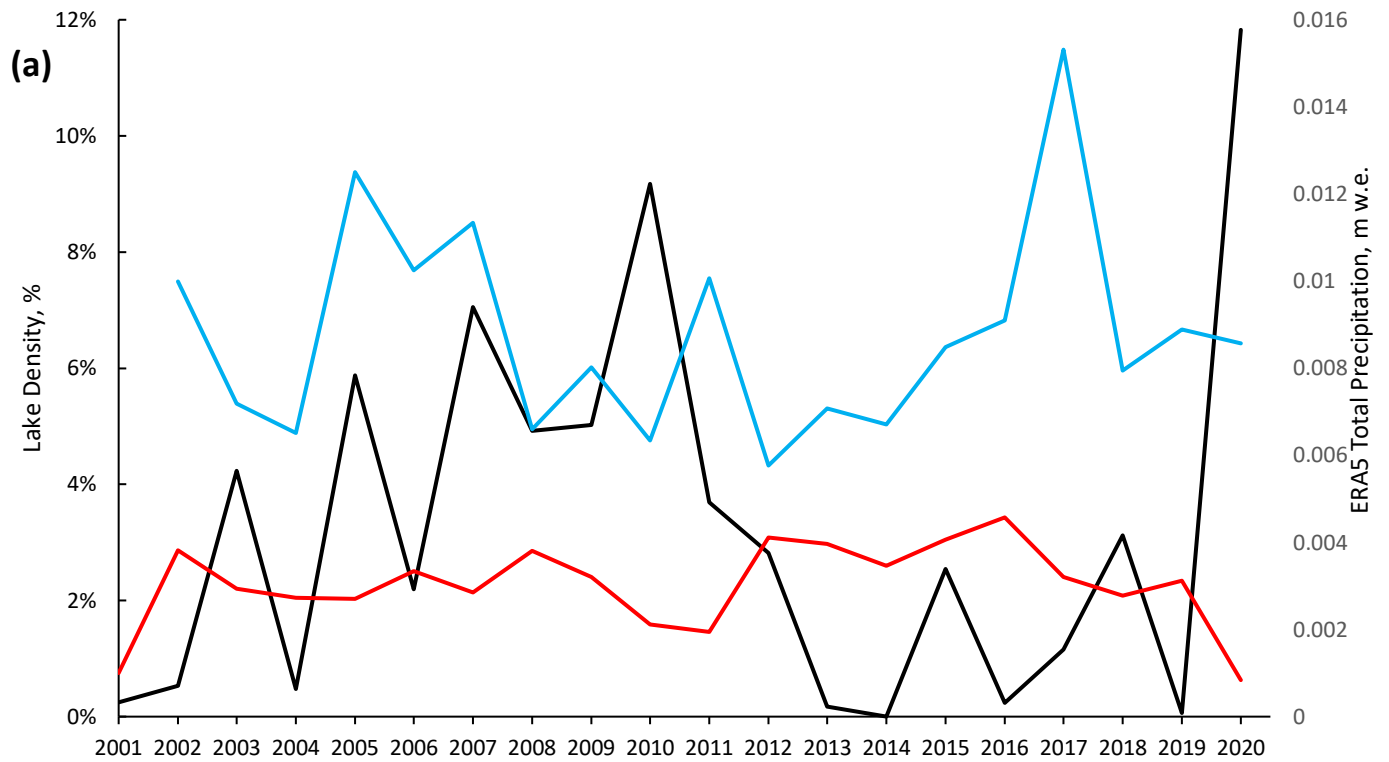


**Figure 10: (a)** Mean precipitation (m of water equivalent) for summer and winter as a timeseries alongside lake density (%). Summer precipitation appears red, Winter precipitation prior to the melt season appears blue, lake density appears black. Precipitation data from ERA5 (C3S, 2017). **(b)** total summer precipitation, m w.e. versus lake density ( $p = 0.04$ ) **(c)** total winter precipitation, m w.e. versus lake density ( $p = 0.94$ ).

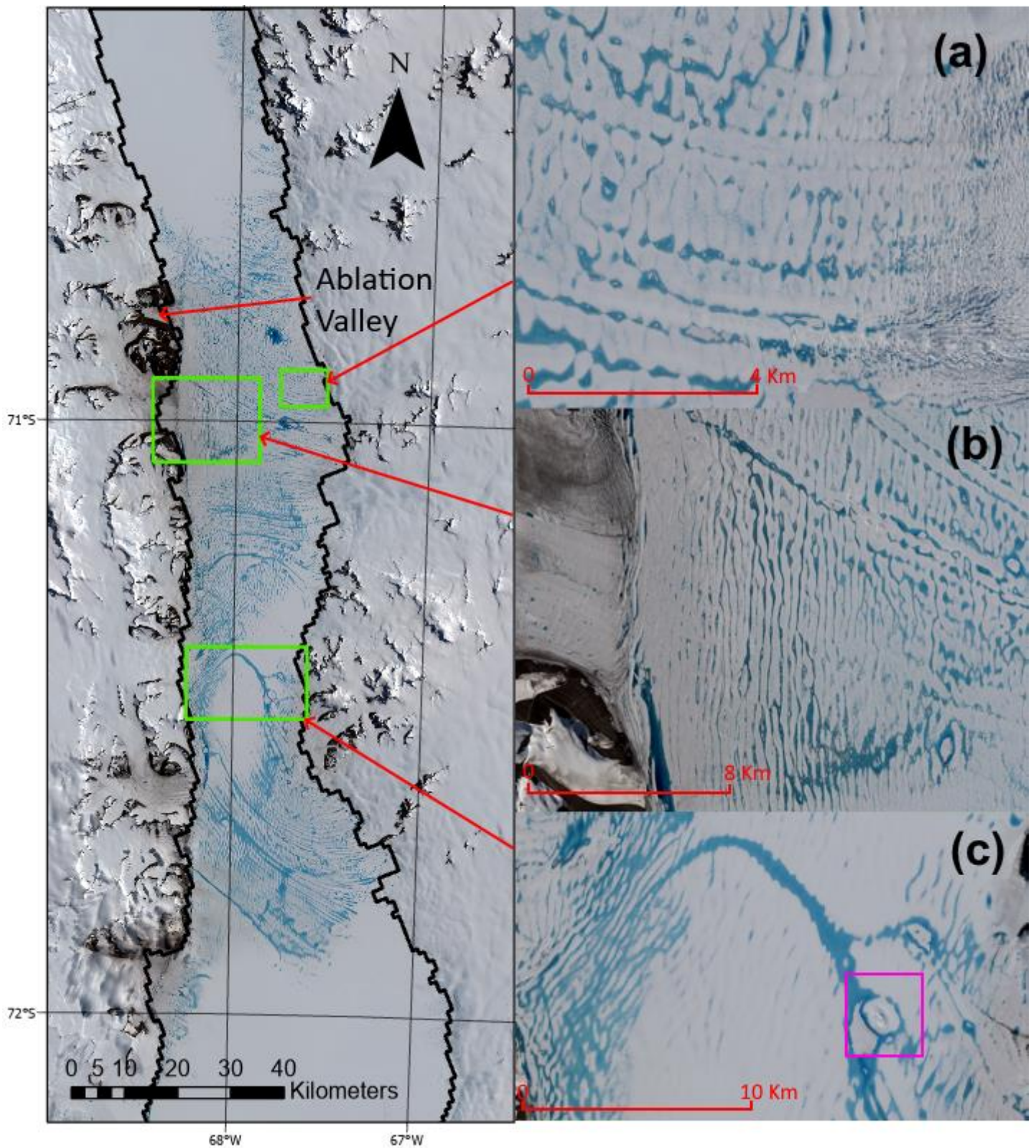


**Figure 11:** Lakes in Sentinel 2 image acquired 19-01-2020. (a) globular lakes, common along the Eastern shoreline, (b) ribbon lakes, common in the West, with some globular lakes to the east, (c) demonstrates an arcuate band, common across several years. Magenta box indicates a relic lake doline (Figure 18).

#### *(4.1.2) Intra-annual Variability in Lakes and Climatic Influences*

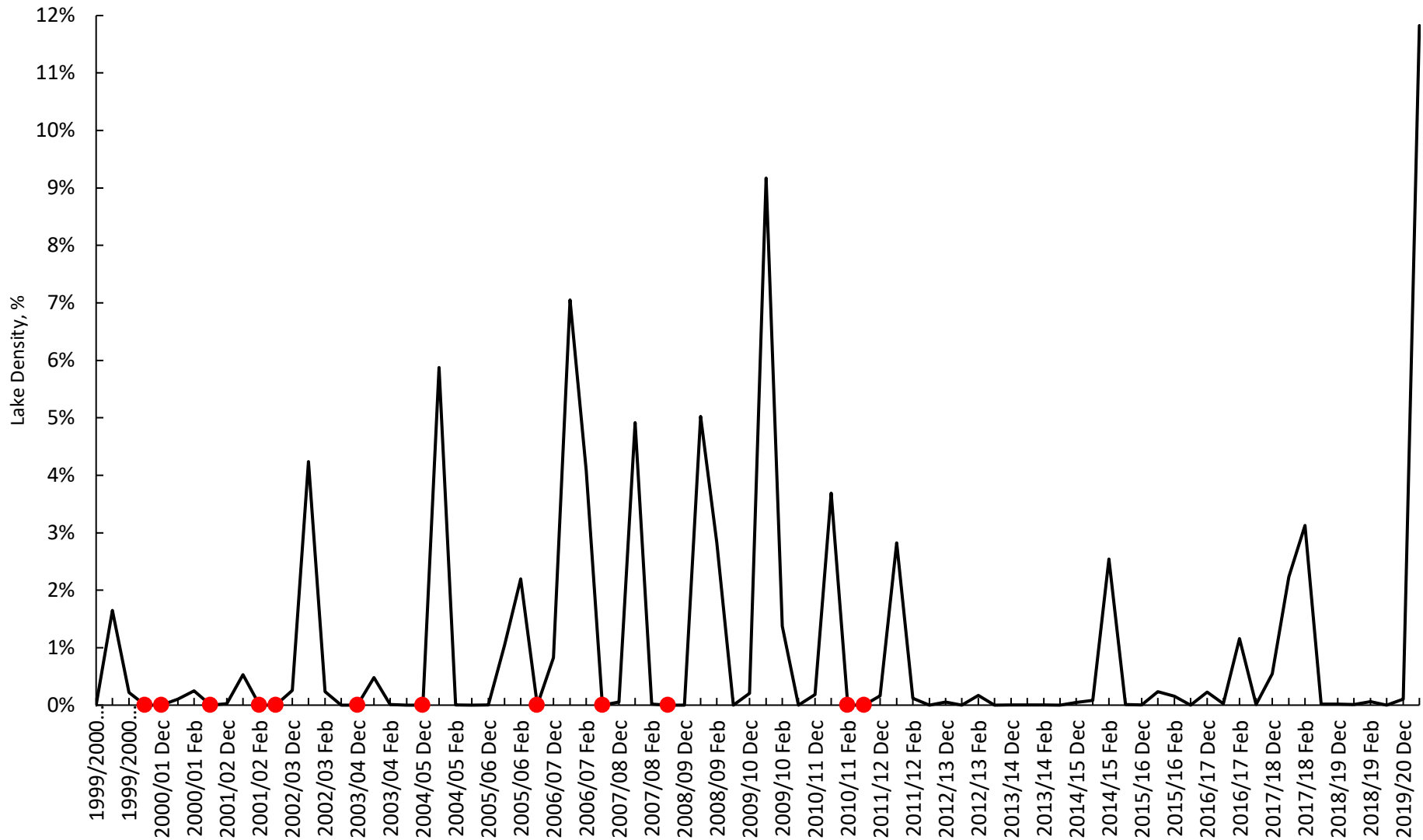
Within a melt season, lakes usually begin to form in December, reach their maximum area in January and have frozen over by the end of March (Figure 12). Typically, lake area increases from zero to peak between December and January, decreases on average by 21% between January and February and decreases by 100% between February and March. This pattern of lake evolution leads to a January peak in lake area in 13/21 of the post-2000 years studied, and a 2-3-month period in which lakes are visible on the ice surface. In approximately one-third of years, lakes reached their maximum area in February, and in one year, 2014, lakes reached their maximum area in December (table 1). In years where lake area peaks in January, lakes shrink more slowly than they grow, as in all but three years lake area has returned to zero before March. In years with a February peak, lakes grow more slowly than they shrink.

These lake density changes closely follow monthly variability in temperature and melting, but not precipitation or wind speed, during 2001-2020 (Figure 13). Lake density follows the rising limb of melt, but starts to decrease while melt is still relatively high. Thus, a lag time is observed between lake density and melt, with more melt occurring later in the season versus decreasing lake density (Figure 13), however due to a paucity of satellite data, the causal process is not clear.

In January-March, there is a close connection between average monthly weather station temperature and lake density (Figure 13c). This is interesting since there is no significant relationship between annual mean temperature and lake density at inter-annual timescales (figure 9). Temperatures increase before lakes start to form, and are already close to peak in December. This suggests that there is a delay between temperatures increasing, melt being produced and lakes beginning to form. While there is no correlation between lake density and precipitation at the intra-annual timescale, towards the end of the melt season lakes shrink as precipitation increases, as refreezing is enhanced through the formation of slush (Stokes et al., 2019).

Mean lake area (i.e. the average size of individual lakes) follows a similar pattern to changes in lake density; lakes grow in size until February when they rapidly shrink. In 2018 however, mean lake area peaks prior to maximum density: December (31950 m<sup>2</sup>), January (48730 m<sup>2</sup>), February (39020 m<sup>2</sup>), March (5840 m<sup>2</sup>). The early peak of lake average area does not correspond to total area, showing a disconnect between the total and average areas of lakes across GVI. As such, on GVI mean lake area does not correspond to total lake area, meaning that lakes stop growing, while lake density continues to increase.

Spatially, lakes typically begin to form around GVI's grounding lines, particularly in the west at Ablation Valley, and then spread southwards to about -71°N, from here they spread across GVI's northern central region. No clear pattern in refreezing is observed, partially due to a lack of high temporal resolution in imagery, though data from 2016 and 2019 suggested that lakes refreeze from North to South. In addition to their spatial distribution, the morphology of lakes evolves over time as the melt season progresses. Typically, early lakes form in a globular style, along the Eastern margin, and develop into a ribbon-like shape over the centre of the ice shelf and along its western margin. Furthermore, lakes across the centre of the ice shelf tend to form arcing bands (Figure 15) as well as a connected lake network, with many globular lakes being connected by narrow sections.



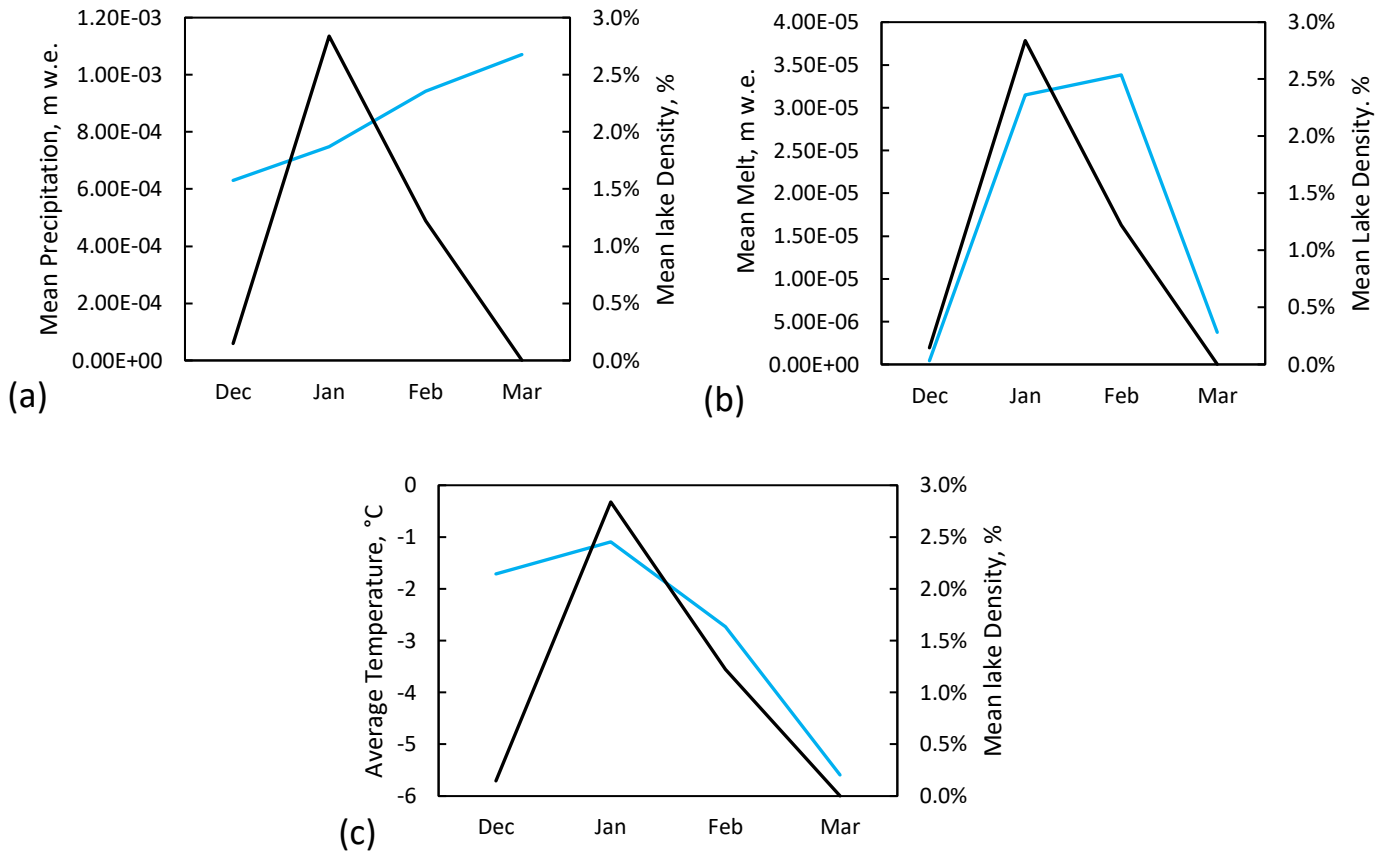


**Figure 13:** (a) Mean melt (combined from 2006 to 2016 for each month) and precipitation from ERA5 data versus mean lake density (b) mean melt (2006-16) from ERA5 data versus mean lake density. (c) weather station temperature data (2006-16) from fossil bluff versus lake density. Within each chart Black indicates lake density, while blue indicates the corresponding climatic variable.

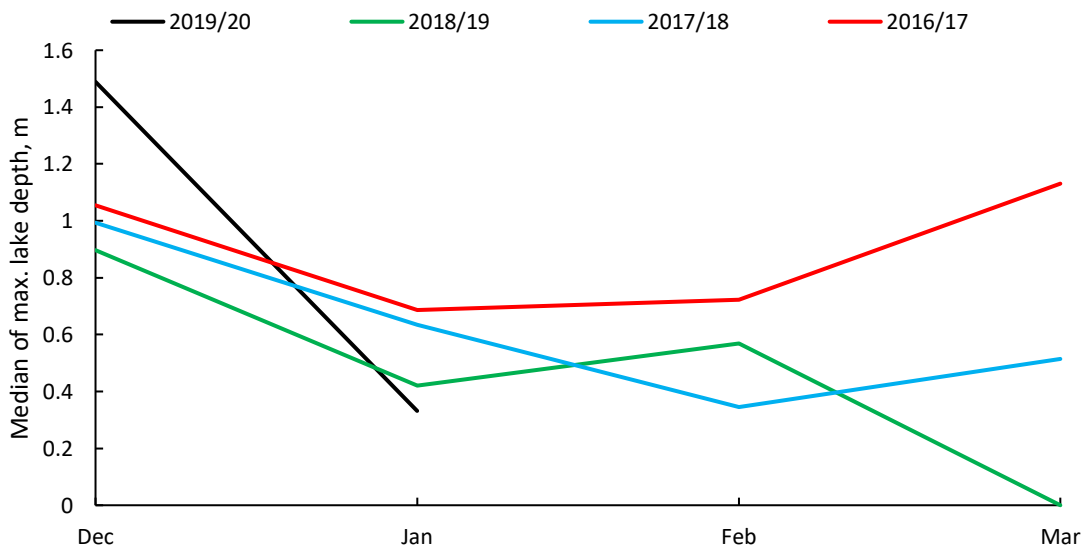


**Figure 14:** Median of maximum lake depth versus month, for years 2015/16 to 2019/20, 2019/20 data ends in January due to time of data collection being mid-melt-season.

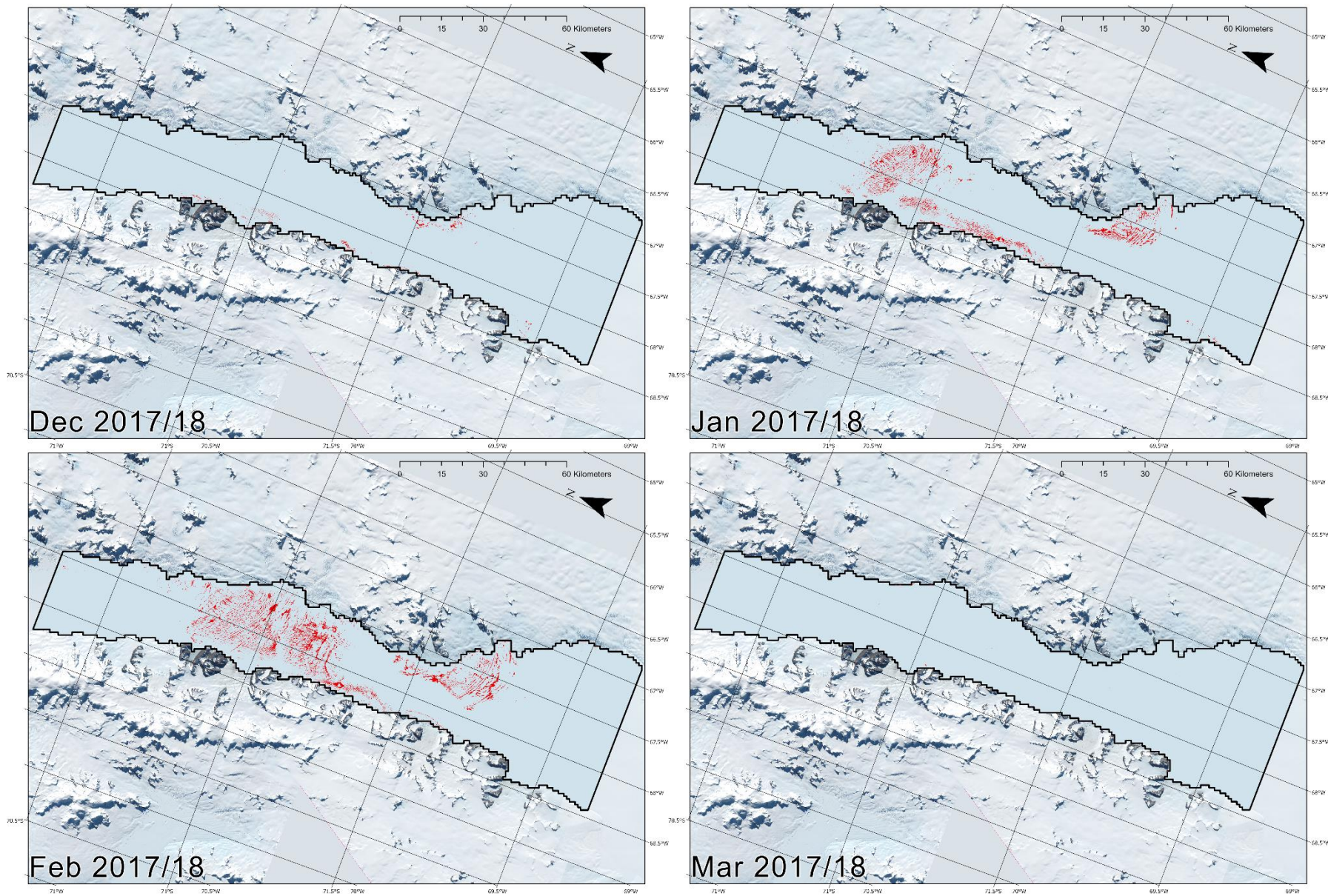


Figure 15: Monthly maximum lake extents in 2017/18. Background is Sentinel-2 imagery acquired 12/2019. Lakes are shown in red.

Year	Maximum Month	Area (km <sup>2</sup> )	Lake Density
2000	Jan	111.44	1.65%
2001	Feb	16.84	0.25%
2002	Jan	36.05	0.53%
2003	Jan	286.92	4.23%
2004	Jan	32.47	0.48%
2005	Jan	398.14	5.88%
2006	Feb	148.89	2.20%
2007	Jan	477.95	7.05%
2008	Jan	333.25	4.92%
2009	Jan	340.39	5.02%
2010	Jan	621.35	9.17%
2011	Jan	250.15	3.69%
2012	Jan	191.12	2.82%
2013	Feb	11.47	0.17%
2014	Dec	0.05	0.00%
2015	Feb	172.06	2.54%
2016	Jan	15.82	0.23%
2017	Feb	78.57	1.16%
2018	Feb	211.70	3.12%
2019	Feb	4.06	0.06%
2020	Jan	801.33	11.83%

**Table 1:** Annual maximum lake density. Values are given in both lake total area, and lake density as a percentage of study area covered.

#### (4.1.3) Pre-2000 climatic influences on SGLs

Prior to 2000 high lake persistence with high lake densities are observed, with imagery from 1989-1991 showing lake densities of 12.09%, 11.48% and 8.49% consecutively (Figure 16a). Lakes additionally extend further southward than in 2020 (Figure 16b), and similar observations are made for 1997, however a lack of imagery makes a numerical value not possible. In addition, the southern expansion of lakes is visually more dense than in 2020. This lake persistence corresponds to a higher decadal mean temperature in 1980-2000, than in 2000-2020 due to the southern annular mode (Turner et al., 2016). Lake density in 1989-91 closely matches mean summer temperature (Figure 16a).

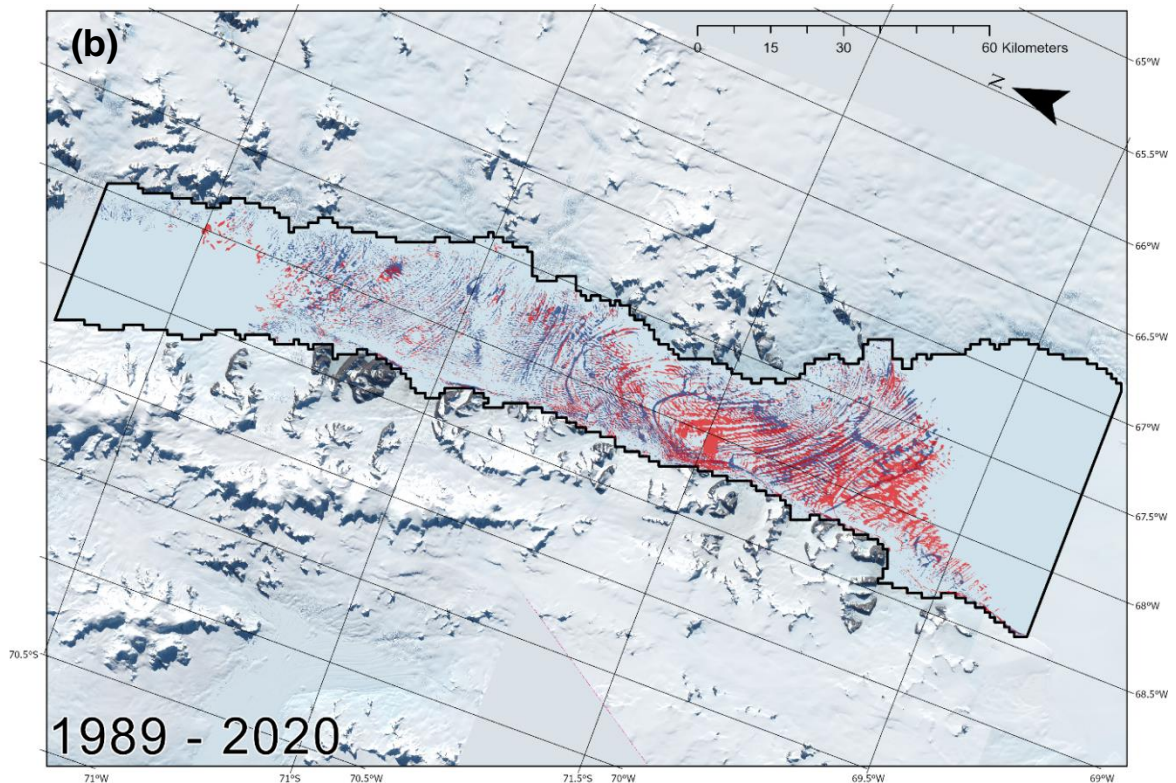
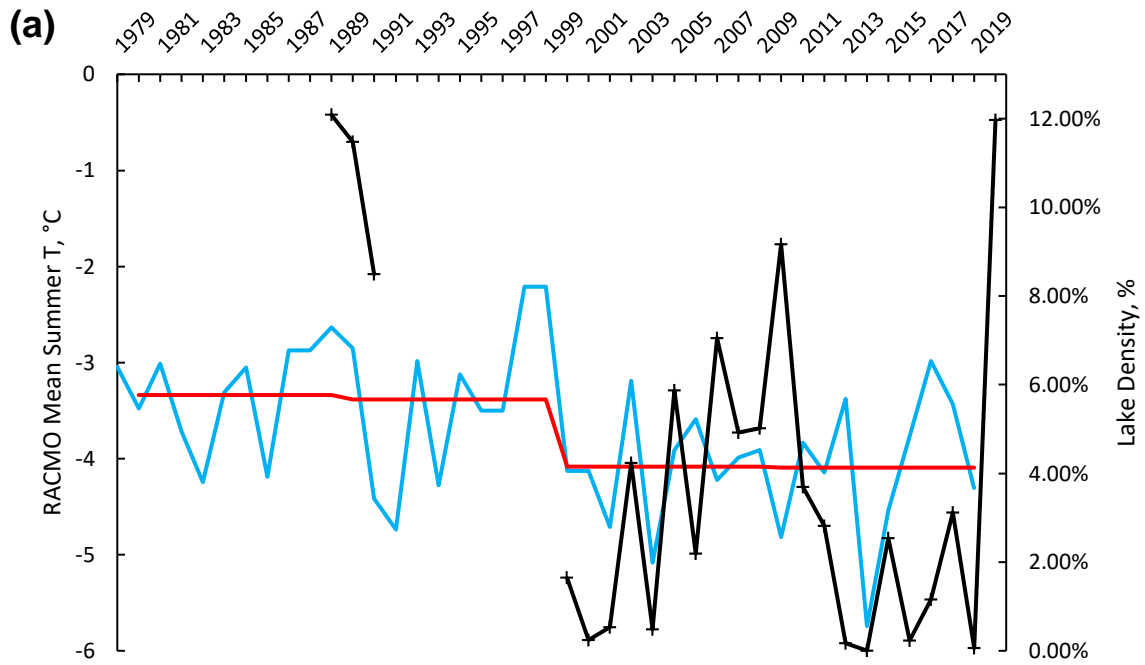


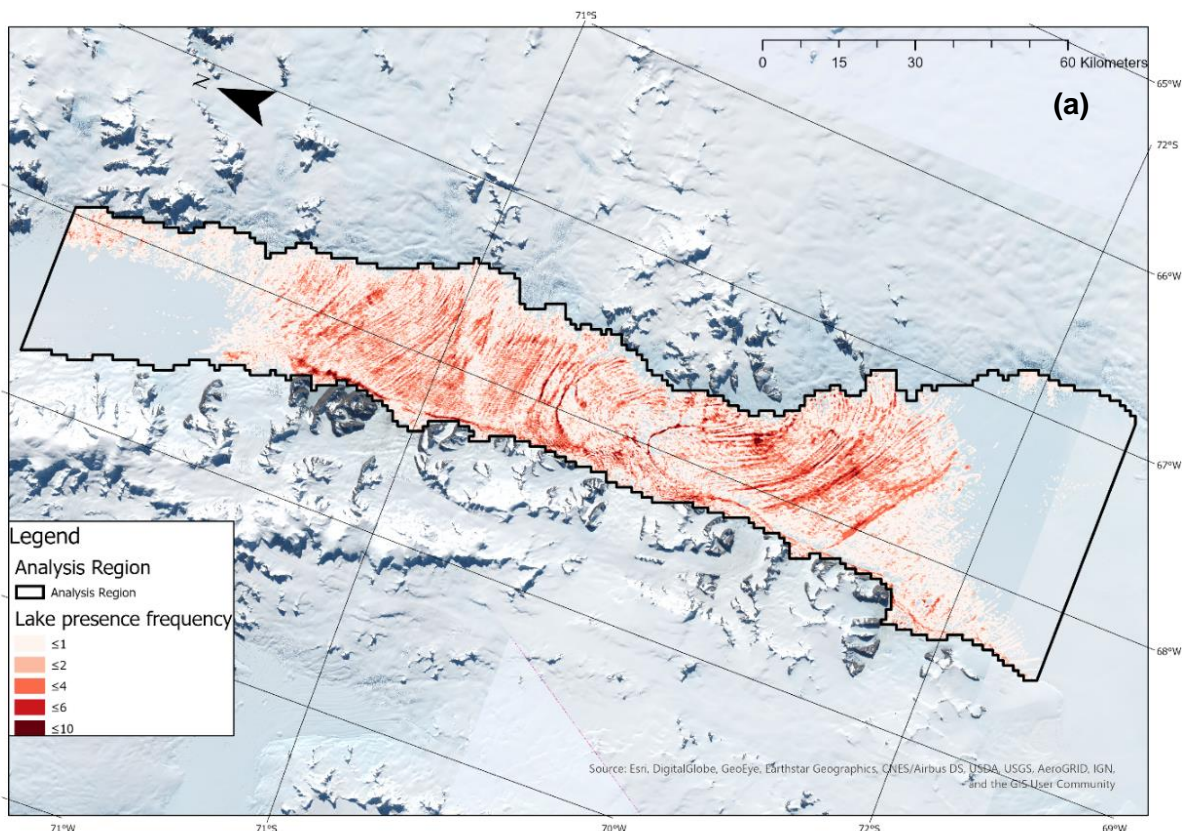
**Figure 16:** (a) RACMO mean summer temperature ( $^{\circ}\text{C}$ ) versus lake density (%) between 1979/2020. Black indicates lake density, blue indicates mean summer temperature, red indicates decadal mean temperature. (b) Comparison of lake coverage on GVI's northern sector between 1989 (red) and 2020 (blue). 1989 extends further south than 2020, with greater coverage, while 2020 shows more significant lake coverage in the north.

#### (4.2) Glaciological controls on lake formation

Glaciological variables, including flow speed, direction and ice shelf elevation, were compared to the observed distribution of lakes (Figure 17). Speed ranges between 0-645 m a<sup>-1</sup> across the study area, with an average of 153 m a<sup>-1</sup>. Flow direction varies through two dominant patterns, with East-West compressional flow from input glaciers towards the western margin, and South-North extensional flow along the western margin to the northern calving front. Elevation relative to sea level is found to range between 9 – 99 m across the study area, with a mean value of 25 m.

Generally, lakes form on the lowest, slowest moving parts of the ice shelf. Within the study area however, lake formation was not found to correlate closely with any single glaciological variable, producing R<sup>2</sup> values between -0.04 and 0.26. Recurrence of lake formation ranges from 0-13 years out of 21. However, hotspots of lake formation (indicated dark red in Figure 17a) occur generally in regions of low elevation and low velocity. Additionally, high speed and high elevation regions, such as the inlet glacier at -72°N, -67°E, show a low degree of lake formation. Glaciological characteristics show more control over lake form; with ribbon lakes being present at the end of the East-West compressional regime and following the South-North extensional flow. Globular lakes appear more commonly within the eastern areas of the ice shelf, where flow is faster (Collins and McCrae, 1985) (Figure 17b).

Arcuate features are notable in the central portion of GVI, with these having high likelihood of lake formation year on year. They are common in the 'low-slow' central region, and arc northwards away from inlets. Comparisons to the BEDMAP2 (Fretwell et al., 2017) grounding line show that these arcuate bands of lakes form most commonly downstream of GVI's narrowest floating section (Figure 17a).



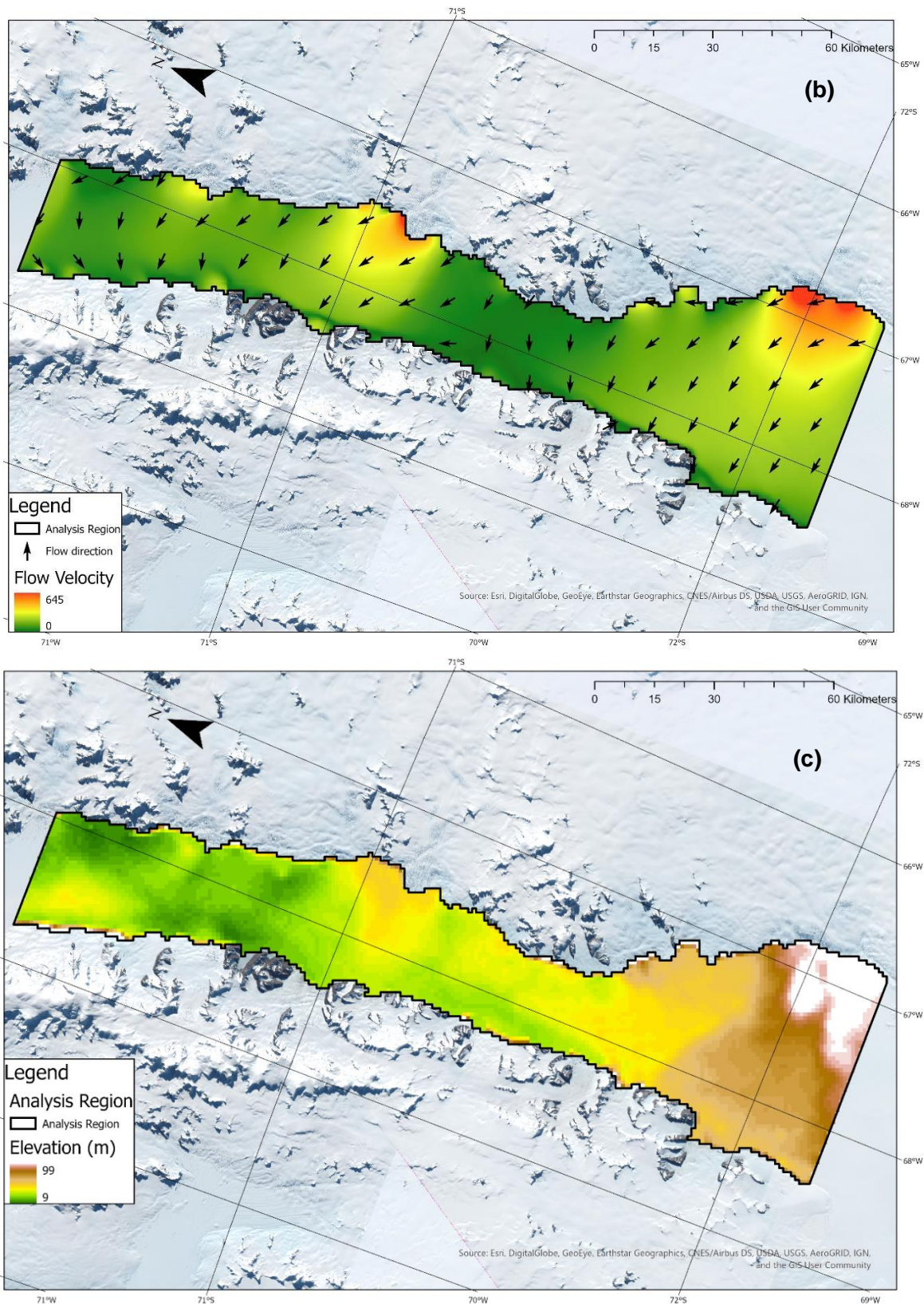


**Figure 17:**(a) Combined lake frequency polygons showing the rate of recurrence at which lakes form over the 21 years studied from 1999/2000 to 2019/20. Maximum value recorded is 13/21, for regions in the South-East of GVI. **(b)** Flow speed is measured across the ice shelf, with red values indicating high, green indicating clear linkages between input glaciers and high flow speed can be seen. Resolution given as 450 m per pixel. Diagram further displays flow direction as a bearing driven vector field. Compressional flow regime is identified from East-West shorelines, data gathered from MEaSUREs (Mouginot et al., 2019 (1 + 2)). **(c)** Elevation values from Bedmap2 (Fretwell et al., 2013). White indicates high, through to green indicating low values. Resolution given at 1000 m per pixel. Basemap produced using Sentinel 2 tiles (ESA, 2019). Grounding line and edge of study area (black) represented using Bedmap2 data.

#### (4.2.1) Evidence of lake drainage

Lake 'dolines', commonly given as evidence of through-ice drainage (MacAyeal, 2015), were present on the ice shelf in 2000 study suggesting that surface lakes have drained on George VI in the past. During 2000-20 however, no through-ice drainage was observed directly and no new dolines were observed to have formed during this period. Further evidence that these features are formed as a result of lake drainage is that some (e.g. Figure 18) are located in the middle of a ring shaped lake, which are attributed to ponding of water in a concentric fracture – known to form when lakes drain (Banwell et al., 2019; 2013). These lakes showed no evidence of lateral drainage into the doline feature, or vertical drainage out, though occasionally small pockets of water were observed at the base of the depression. While no dolines were observed forming between 2000-2020, between 1991-2000 6-8 new dolines were observed in the 1999/2000 imagery versus 1990/91, primarily within the south of the study area.

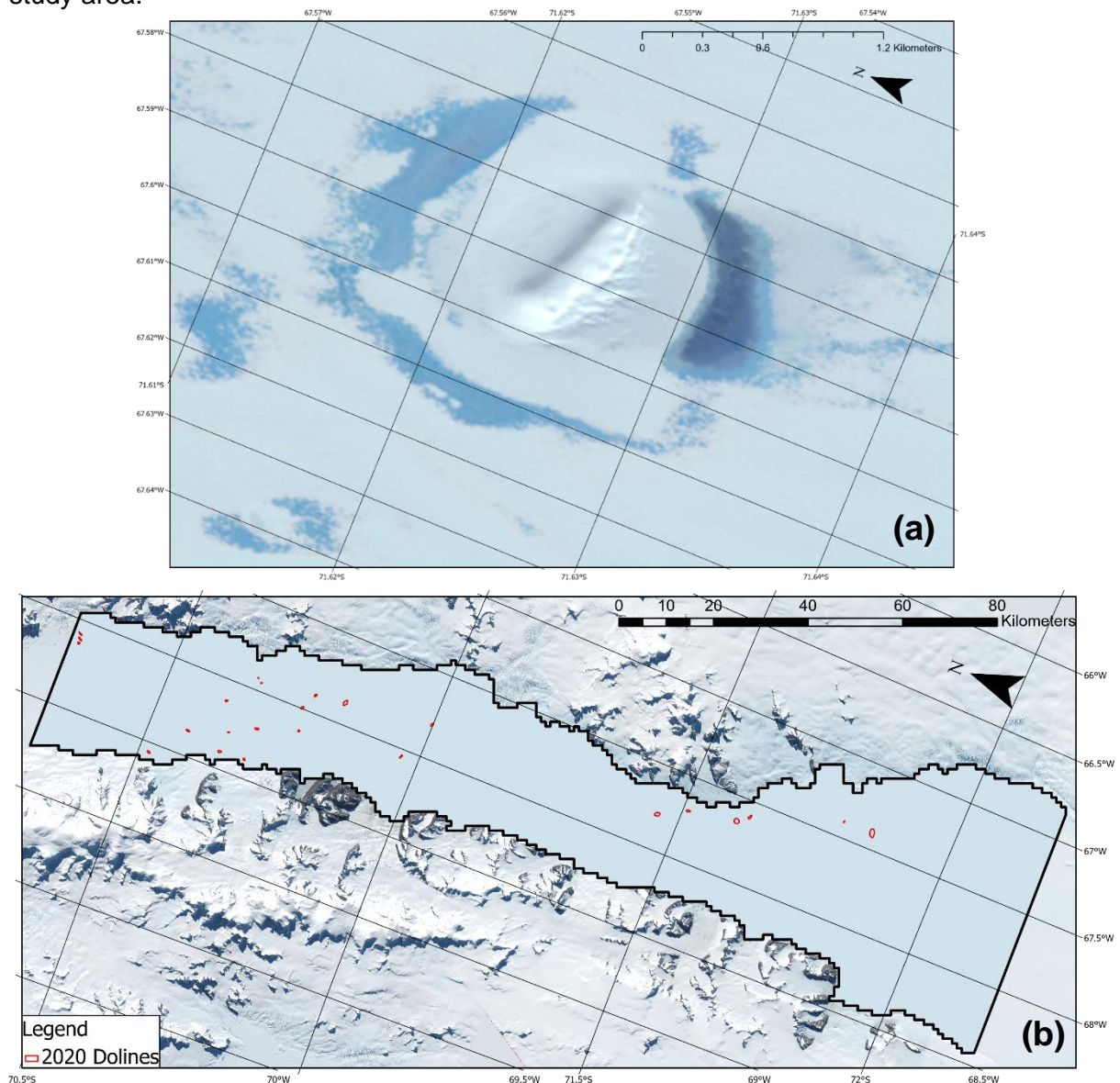


**Figure 18:**(a) Permanent doline on the Eastern margin of GVI in 2017, at (-67.745°E; -71.570°N).

Concentric lake features are clearly observable, along with the doline. No water is observable in the depression. Image acquired by Sentinel 2 on 28-02-2017. (b) Map of dolines recorded in 2020 in the northern sector of GVI through visual observations.

A major lateral supraglacial drainage event was observed in 2019, when a pond within a crevasse spilled over, draining water southwards across a 5.83 km<sup>2</sup> area of the ice shelf surface (Figure 19), showing an increase in lake size of an order of magnitude. The drainage event was first visible on the 25th of January and ended between 17th and 24th February. On 15th February the northernmost drained area began to refreeze, and by 27th February the entire area was frozen. The source of the water for the drainage event appears to have come from within the crevasse field to the east of the initial lake through a series of large channels.

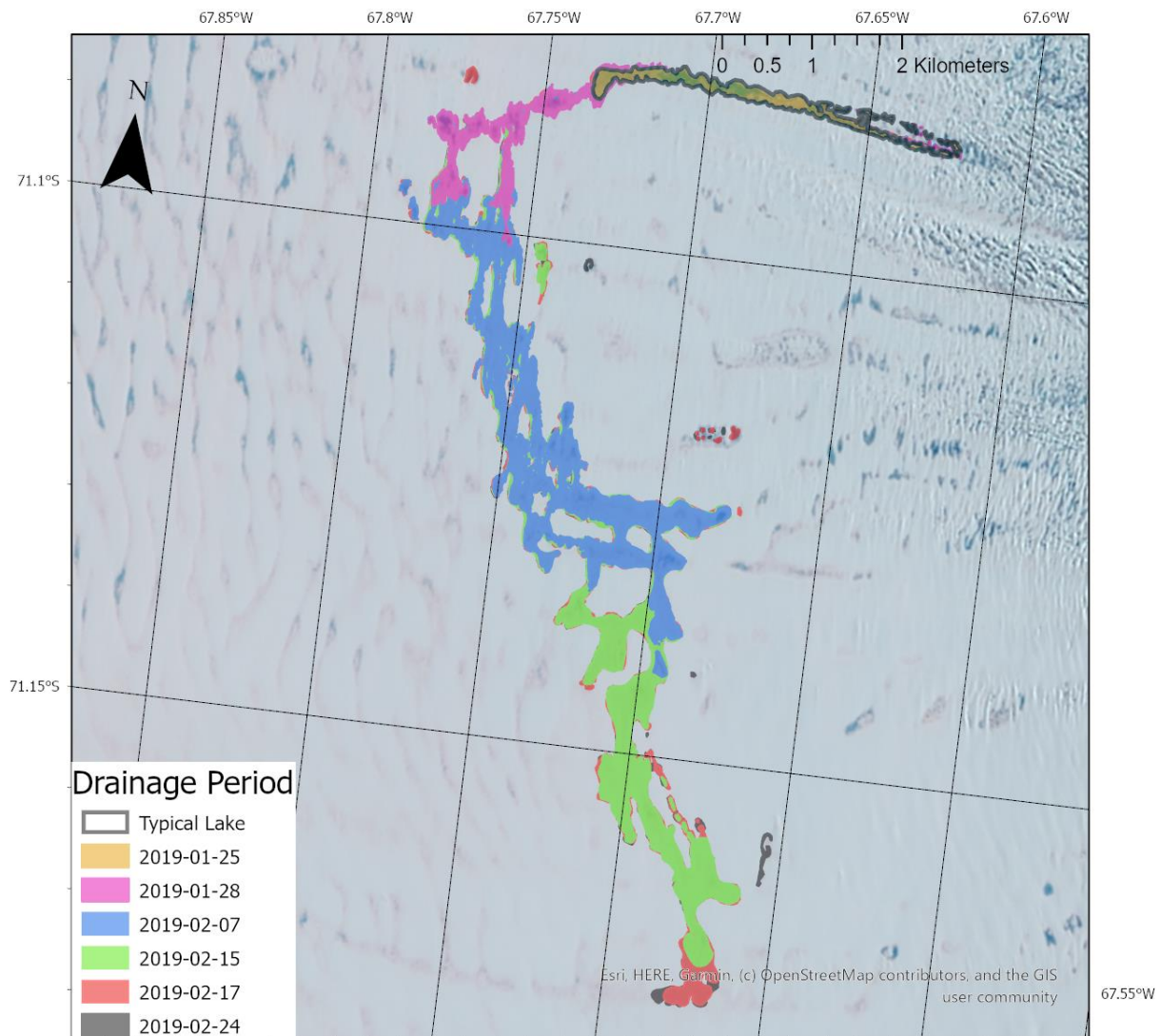


**Figure 19:** Map of the 2019 drainage feature, using S2 and L8 tiles from January – February 2019. Features were manually delineated and extend southwards with time. Underlying colours cover the area associated with regions from prior dates Black outline shows ‘typical’ region covered by the lake in question, extracted from 2019-01-25, and compared to 2019/20’s lake extent. Basemap produced using Sentinel 2 tiles. (ESA, 2019)

From visual inspection of imagery, the dominant mode of lake cessation at the end of the melt season appears to be refreezing on George VI. Lakes freeze either by forming an ice 'lid', which propagates from the centre of the lake out towards its edges and then vertically downward (Langley et al., 2016), or by full uniform freezing of the lake. Based on the interval of imagery, and refreezing duration of the feature in Figure 19, refreezing appears to occur on a scale of 1 – 2 weeks. It is not clear how representative this is however as images with sufficient temporal separation to pinpoint refreezing were not available for other years. Refreezing is often coupled with snow cover (Figure 20), with snow cover changing the appearance of refrozen lakes from pale blue scars, through to white scars, and then uniform with the ice shelf surface. It is not possible to determine whether lakes fully freeze-through using these data, since lakes on George VI are shallow however, it is likely that they do. Shallow lakes require less cooling to refreeze, which is helped by the fact that they tend to have a lower basal temperature (Leppäranta, 2014).

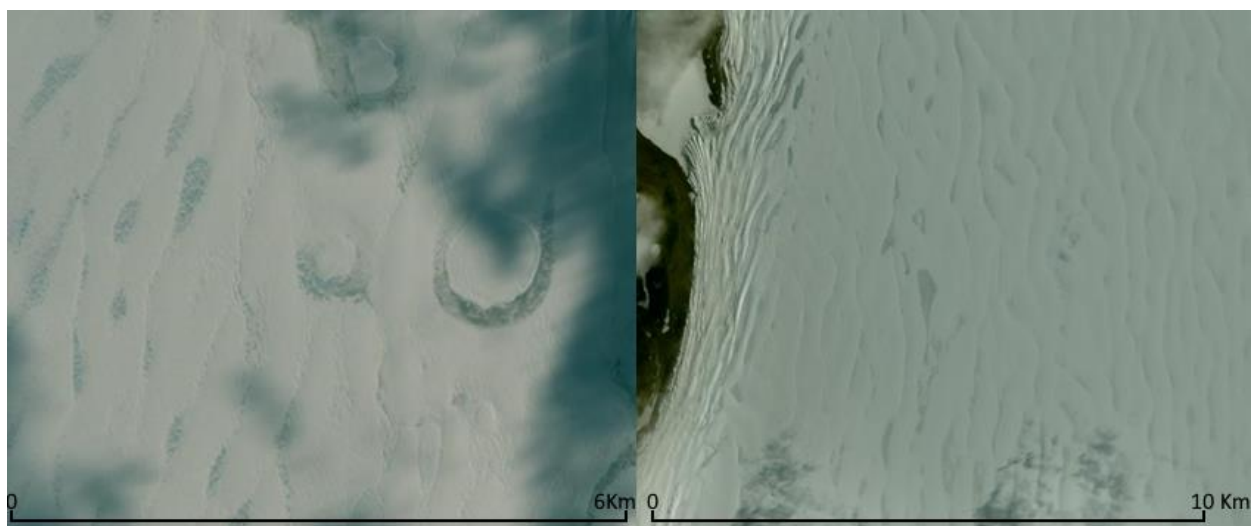


**Figure 20: (a)** (left) Imagery of 'blue scars', showing speckled, blue regions of refrozen lakes on the Eastern margin of George VI, speckles are likely a result of snowdrifts. Refreezing caps are also visible in the top right of the image. Scale: 1:20000 at 71.627°S 67.769°W; 71.585°S 67.596°W. **(b)** (right) Imagery of 'white scars', where lakes have been more heavily influenced by snowfall. Imagery from Sentinel (ESA, 2019), March 2018. Scale 1:35000 at 70.925°S 68.3422141°W; 70.852°S 68.048°W.

### (4.3) Albedo values and associated impacts

Because lakes are darker than the surrounding ice their albedo is lower, and they absorb more solar radiation which can lead to additional melting. Assuming that melting beneath lakes is twice that of the surrounding bare ice (Tedesco et al., 2012), this additional melting is effectively the lake density. On this basis, lakes on GVI can cause up to ~12% additional melt versus a theoretical copy of GVI with no lakes. It is not clear if this assumption is valid for George VI, since it is based on data for Greenland where lakes are deeper, and the surrounding ice is dirtier than in Antarctica. Thus, reflectance information from the satellite images is used to calculate the change in reflectance between GVI with lakes, and GVI without lakes (section 3.3.5). However, due to scanline issues in LS7 imagery prior to 2014, this analysis was restricted to 2014-present.

During 2014-2020, the presence of lakes decreases reflectance integrated over GVI by 0 - 5%, with maximum and minimum values occurring in 2020 and 2014 respectively (Figure 21). The impact of lakes on reflectance is linearly related to lake density ( $R^2=0.95$ ). For every 1% increase in lake density, a change in ice shelf reflectance of 0.4% is observed (Figure 22a). However, if the 2020 value is removed,  $R^2$  drops to 0.45, showing a high degree of leverage from this value. 2015 appears to be an outlier as while lakes are abundant (covering 2.54% of the ice surface), they are also shallow, thus they only reduce reflectance by 0.06%. In general, there is only a weak relationship between change in ice shelf reflectance and lake depth ( $R^2 = 0.37$ ), thus lake density is more significant in changing ice shelf integrated albedo (Figure 22b). It is likely that depth has an impact on melting at the local scale however, since deep water has a lower albedo than shallow water, as more radiation is absorbed and scattered (Pope et al., 2016).

There is a possibility that a smaller quantity of deeper lakes will result in a greater decrease in reflectance, due to deeper lakes having lower reflectance values. To demonstrate the impact that the change in reflectance would have on recorded albedo values, the reflectance decrease values were applied to albedo values given by the ERA5 climate model, which does not account for lakes. The maximum difference in albedo between GVI with lakes and without lakes was a 0.04 decrease, from 0.85-0.81 in 2020, calculated by applying the calculated % decrease to ERA5 albedo values (Appendix 8).

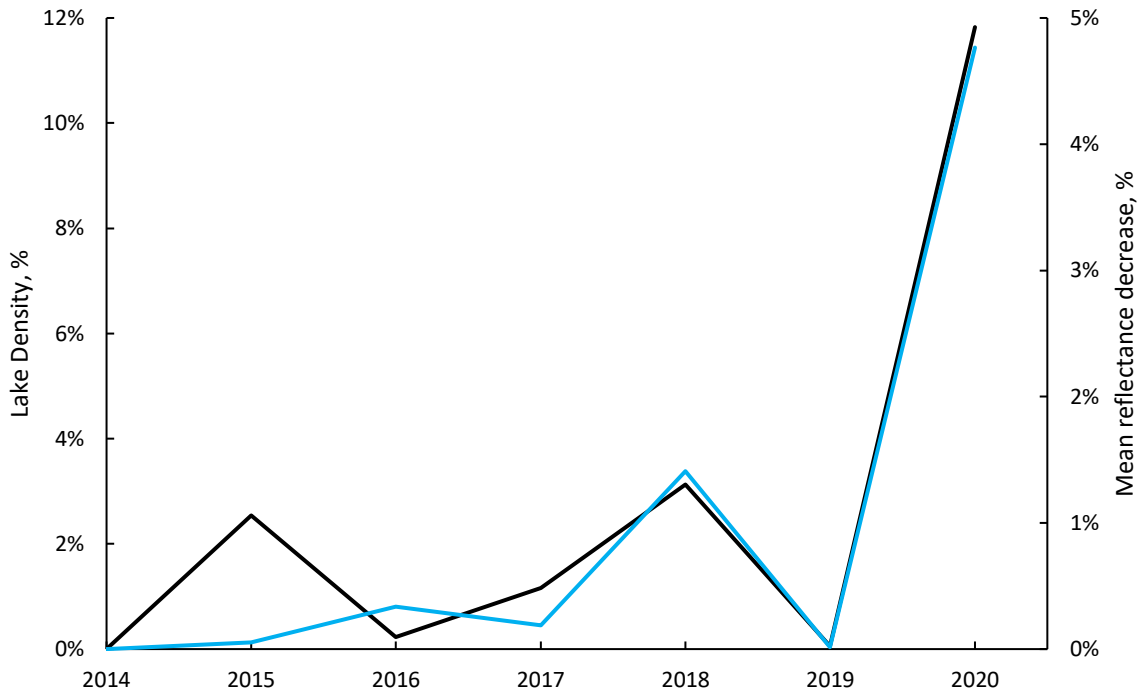


**Figure 21:** Graph of peak annual lake density versus calculated change in reflectance, calculated as the mean decrease in reflectance values of R, G, B, NIR bands between a full mask of GVI (including lakes) and a mask of GVI which has lake polygons removed from it. A moderate relationship is visible along with an anomalous value for 2015. The black line represents lake density, while the blue line represents the mean reflectance decrease.

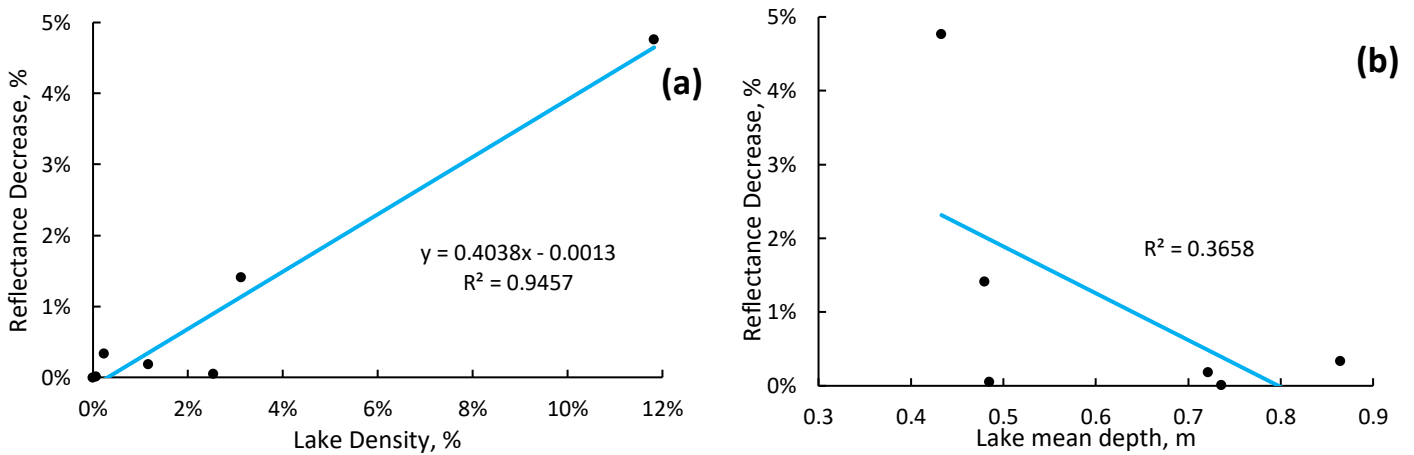


**Figure 22: (a)** (left) Scatter of reflectance decrease versus lake density, showing a strong correlation. With a higher lake density demonstrating greater reflectance decreases. **(b)** Scatter of reflectance decrease versus mean lake depth across the ice shelf at peak (2016-20).

## **(5.0) Discussion**

In this section I discuss the main findings that were presented in chapter 4, considering both the current state of GVI and its lakes, and the impacts that drainage and albedo have upon the ice shelf. In section 5.1, climatic variance is considered, discussing interannual climatological variation in section 5.1.1, and intra-annual climatological variation in section 5.1.2. In section 5.1.3 I consider the findings regarding lakes prior to 2000, and their association with climate. In section 5.2 I discuss the impact of glaciological factors on GVI and its SGLs, covering physical influences such as topography and ice flow characteristics. In section 5.3 I consider observed drainage and its impacts on GVI, while in section 5.4 albedo is considered, discussing how lakes influence the reflectivity of GVI. In section 5.5 I address limitations and alternative approaches for use in future work, and finally in section 5.5.1, I suggest some future developments of the methods used in this study.

### **(5.1) Climatologically induced variation in SGLs on GVI**

#### *(5.1.1) Interannual climatological variation*

Summer precipitation shows a significant but weak inverse relationship with lake density ( $R^2 = 0.51$ ;  $p = 0.04$  (Figure 10a, b), further confirmed as the major factor through multivariate analysis. This means that summer precipitation is a controlling factor on lake density, low summer precipitation corresponds to high lake density, leading to 9.2% lake density in 2010 (the second highest on record between 2000-2020, and ~3 times the mean value), while summer precipitation is 1 standard deviation from average. Increased summer precipitation leading to lower lake densities is reported in prior studies (Dunmire et al., 2020), which indicate liquid water lakes being buried by snowfall. Furthermore, snow cover will increase albedo as fresh snow is more reflective than glacier ice and old snow (0.8 vs. 0.45-0.7 (Mcevoy and Castaner, 2012). This causes the ice shelf to absorb lesser insolation during a year of high snowfall, resulting in lesser energy for melting and hence, fewer lakes. This is important because the western AP records greater snowfall than the eastern AP (Wessem et al., 2017; WWF et al., 2013), further evidenced by the frequent cloud cover on GVI. Thus, the link between summer precipitation and annual lake density is important as it represents a factor of increased stability due to GVI's climate.

GVI's northern sector sits above the  $-9^{\circ}\text{C}$  isotherm (Figure 3), making its climate as warm as the Larsen B ice shelf was at its point of collapse. This leads to the consideration that GVI may be unstable, as it shares average annual temperature with vulnerable ice shelves which have undergone catastrophic collapse in the recent past (Cook and Vaughan, 2010). This is important, as Rebesco et al., (2014) identifies near-surface air temperatures as a factor in the collapse of the Larsen B ice shelf, thus suggesting that GVI could be subject to similar collapse in the near future.

However, this study shows that mean annual, winter and summer temperature has no statistically significant connection to lake density. Additionally, positive degree day values show no significant connection. Yet, in exceptional cases, temperature and lake density showed coupling, with values of  $\sim\pm 2.5\sigma$  from average leading to corresponding high or low lake presence in 2014 and 2020. In 2014 there was an unusually low lake density, with a summer  $2.4\sigma$  colder than average, while in 2020 there was an unusually high lake density, and temperatures were  $2.7\sigma$  warmer. Despite this, decadal averages (Figure 16a) show some coupling between temperature and lake density. The importance of this lack of linkage on an annual scale indicates that temperature is not always a major factor in controlling lake density, contradicting Rebesco et al., (2014). This means that, at least on an annual scale between

2000 and 2020, average temperature as displayed by the  $-9^{\circ}\text{C}$  isotherm and its association with ice shelf instability does not apply to GVI.

Annual lake density is highly variable, from 0% in some years to  $\sim 12\%$  in others and about 2% on average, while maximum coverage is 6 times the mean. This is interesting because, on the Larsen B ice shelf lakes were observed to cover 10% of its surface just prior to its collapse (Banwell et al., 2013) which suggests that GVI supports a population of lakes that is large enough to lead to a similar event. However, lake density at this level was persistent for nearly a decade on Larsen B before collapse (Leeson et al., 2020) and in the twenty-year (2000-2020) record GVI's lake population reaches this level of coverage only twice (2010 and 2020). This therefore suggests that rather than simple lake density, persistence of high lake density values, year-on-year, are more significant in ice shelf collapse, as observed on Larsen B.

In addition to the lack of lake persistence on GVI, the unique topographic setting and compressional flow regime of the ice shelf is likely to stabilise it, thus meaning that even if lakes were persistent, they would not have the catastrophic effect observed on Larsen B in 2002. This is additionally shown by high lake presence on GVI in the pre-2000s, with no major collapse of GVI despite persistent lakes. Persistence is enhanced by refrozen lake ice having a lower albedo and lesser air content than its surroundings, causing it to melt first (Hambrey et al., 2015; Bell et al., 2018). Thus, depressions which previously held lakes will repeatedly hold them in following melt seasons. From this, it is likely these depressions deepen year on year due to enhanced basin melting (Tedesco et al., 2012), thus showing the impact of persistent lakes on ice shelf stability.

GVI's southern sector shows little lake presence throughout the study, with a lack of lakes forming or encroaching south of  $72^{\circ}\text{S}$  within the study period. Stability is implied because lakes are cause of instability on ice shelves and prior to Larsen B's collapse, lakes were observed to encroach southwards (Leeson et al., 2020), while this is not occurring on GVI. Yet, long-term patterns show GVI has had repeated lake formation for at least 31 years, with imagery from as early as 1989 showing lake coverage on the northern sector of the ice shelf. The abundant population of lakes on GVI's northern sector suggests the region may be on the 'edge of climatic stability' (Branson, 2019), meaning there is a possibility of collapse due to climatic factors. If this part of the ice shelf were to collapse, major glaciers on both Alexander Island and Palmer Land would lose the buttressing effect that GVI provides; which would like trigger an increasing glacier flow speed and lead to an increase in iceberg calving (Schannwell, 2017).

#### *(5.1.2) Intra-annual climatological variation*

Temperature values on a monthly scale show a relationship with lake density, with high lake density months corresponding to months with high average temperature (Figure 13c). This shorter-term linkage between temperature and lake density is consistent with Langley et al., (2016), who identifies short term temperature changes on a daily-monthly scale having a significant impact on SGLs. The increase in density alongside temperature comes from the increase in energy available for melting, thus enhancing lake formation as more areas of GVI have surface temperatures brought to above  $0^{\circ}\text{C}$ . The importance of this relationship on a monthly timescale is reflected in literature such as Langley et al., (2016), and identifies monthly temperature averages as a control on lake formation on GVI.

Melt values show a close coupling with lake density; they also show a lag time in which peak melting occurs after peak lake area on average (Figure 13b). This provides evidence for

melt being a control on lake formation in the short term, as it provides the water available for pools to form. Additionally, the lag time indicates a degree of hydrological lag in the values. Lag time indicates water being held in storage, for example, within firn or snowpack commonly seen on Greenland (Harper et al., 2012). A second possibility would be that with increased snowfall, shallower lakes become buried later in the melt season (Dunmire et al., 2020), while the darker, deeper lakes continue to melt, thus increasing their storage capacity as they deepen (Tedesco et al., 2012). This pair of factors would have the effect of a lower lake density as the wide surface area, shallow lakes disappear, while the small surface area, deep lakes remain. The importance of this melt-lake density relationship shows that monthly scale factors are important in SGL formation on GVI, and indicates that multiple climatic factors may combine to drive the complex observed behaviour.

The typical peak in lake density lies in January, with refreezing or lake burial occurring rapidly in the following month, over a duration of less than 2 weeks. Thus, the cessation of GVI's melt season is clearly a rapid process, as with the initial formation of lakes, occurring on a scale of 1-2 weeks. This is a factor of the shallow lakes on GVI, as temperatures during this process drop by 3°C on average, which is unlikely to lead to rapid cooling. Thus, due to low depths, lakes will have a lower required amount of cooling for refreezing to occur, due to the wide surface area of ribbon lakes, and the shallow average depth. Ice-lid formation may also occur, as many lakes appear to refreeze from the centre-outward (Langley et al., 2016). This rapid change in lakes across the melt season occurs alongside changes in climatic variables such as cooling and increased snowfall (Figure 13), further demonstrating the linkage between temperature, melt, precipitation and lake density. Additionally, the rapid disappearance of lakes on GVI can be argued as a product of the increase in snowfall later in the melt season, burying some lakes, while decreased temperatures alongside lesser melt cause others to freeze.

Precipitation shows a minor inverse relationship with lake density at a monthly scale (Figure 13a). The short-term inverse relationship as observed here links back to the correlation between summer precipitation and lake density values on an inter-annual basis ( $R^2 = 0.51$ ;  $p = 0.04$  (Figure 10b)). This inverse relationship has a plausible physical explanation as snow input into lakes would lead to cooling through introduction of cooler material, thus enhancing refreezing through formation of slush via direct input of snow to SGLs (Stokes et al., 2019). Additionally, as with the inter-annual correlation, burying of lakes is likely, as is an increase in albedo as evidenced by snowdrift coverage of lakes in Figure 20a. The links between precipitation and lake density at an intra-annual scale is therefore important as it adds to the concept of multiple factors combining to drive the complex behaviour of SGLs on GVI. Furthermore, the introduction of additional snow later in the melt season helps return albedo to lower values, thus increasing stability due to the lower propensity for melting to occur.

### *(5.1.3) Pre-2000 climatological variation*

In three consecutive years before 2000 (1989-91), and through visual inspection of low-quality, cloud-filled imagery acquired in 1997, a high lake density was observed, with lakes extending further south on GVI than in 2020 (Figure 16a, b). During this time, decadal averages of summer temperature were 0.7°C warmer than the period of 2000-2020 due to changes in the southern annular mode (Turner et al., 2016). It is possible that higher average temperature than the long-term mean led to the collapse of Larsen B ice shelf, through the presence of persistent lakes covering ~12% of its surface (Leeson et al., 2020). This warm period means that it is likely that GVI has had extended periods of melt in the past, at minimum

3 consecutive years of high melt, possibly more as changes in lake density in 1989-91 closely resemble annual changes in temperature (Figure 16a). Additionally, despite having consecutive years with as high lake density as 2020, GVI has remained robust to catastrophic collapse, while neighbouring ice shelves have collapsed catastrophically. Thus, GVI demonstrates a robustness against climatic forcing compared to Larsen B, as it has not collapsed under similar temperatures, with consistent 10%+ melting (Figure 16a, Turner et al., 2016; Banwell et al., 2013). Furthermore, due to cyclic nature of the southern annular mode, it is likely that GVI will experience an extended warming period again, leading to a similar degree of persistent melting, and thus experience similar instability in future.

## (5.2) Glaciologically induced variation in SGLs on GVI

Glaciological characteristics within the study area – which shows lower average elevation and flow speed than GVI's southern sector – show no statistically significant link to SGL formation. However, as no substantial concentrations of lakes are found outside the study area in GVI's southern sector throughout the study, on an ice shelf scale there appears to be a link between glaciological characteristics and lake formation. This implies that on an ice shelf scale, the glaciology is a controlling factor in SGL formation on GVI. However, when narrowed to the scale of the study region (Figure 1), these factors have much less of an impact.

Hotspots of lake formation however do appear to form in areas of low flow speed and elevation, but this is in several isolated cases rather than the statistical norm (Figure 17). These are hotspots of lake formation frequency, particularly along the western margin of GVI, and around permanent dolines (Figure 17; 18). The high frequency of formation in the west in Figure 17a corresponds to a low flow speed region in Figure 17b, and a small trough in Figure 17c. Yet, this connection between elevation and speed in isolated cases may be co-incidental as a result of other factors such as flow direction. Despite this, high formation frequency around these regions is important, as while lakes are observed in these low speed, low elevation regions, they are not observed on faster-flowing and high elevation areas, such as inlet glaciers. Furthermore, literature states that SGLs typically form on relatively low lying, level areas of ice in Greenland (Bell et al., 2018), and thus this may be extended to Antarctica, to a greater extreme (Trusel et al., 2013).

Permanent dolines are also observed to be present in areas of low flow speed on GVI. This means that areas of low flow speed are areas in which englacial drainage has occurred in the past on GVI. These dolines remaining permanently on the ice shelf surface indicates a lack of sufficient differential flow speed to close these depressions, which explains the locations of these dolines. Additionally, the formation of these features on Larsen B was observed to be a result of repeated melt cycles, leading to englacial drainage and hydrofracture. So, it is likely the areas of lowest flow speed on GVI (less than  $10 \text{ m a}^{-1}$ ) (Figure 17b) assisted in maintaining depressions, thus leading to these permanent features forming and being preserved (Matsuoka et al., 2015) as low flow speed leads to less deformation of surface morphology. This can identify regions of GVI, particularly those of extremely low flow speed where deep lakes already exist, as hotspots for englacial drainage.

In addition to glaciological characteristics, mean lake area is effectively unlimited, while lake depth displays an 'upper limit'. However, changes in lake area are not reflected by changes in depth, the latter of which does not extend beyond 4.8m, similarly to Banwell et al., (2014)'s findings. An example of this is 2020, where maximum lake depth is 3.6m, despite having the largest recorded maximum lake area. Statistically, this lack of relationship is clear

with  $R^2$  values ranging between 0.000134 and 0.008629. Additionally, lakes on GVI are shallower than other ice shelves due to the prevalence of ribbon lakes, meaning they are less likely to hydrofracture (Banwell et al., 2013). This is due to shallower lakes having less propensity to melt through the ice shelf and drain englacially as they have a higher albedo than deeper lakes, and thus lesser basal melting. This is a key factor in addressing stability on GVI, as it indicates that englacial drainage is less likely to be common, as observed in this study. This lack of englacial drainage means that large groups of lakes are unlikely to drain in quick succession, as deep lakes on GVI are typically isolated, as evidenced by the locations of permanent dolines across the surface. Therefore, mass hydrofracture and catastrophic failure of the ice shelf not likely.

Ice flow direction adds to the previous point, as it governs the stress patterns of the ice shelf, and therefore the types of lakes which form. George VI's primary East-West flow in the northern sector produces a compressional regime, with South-North secondary flow extending this, producing 'pressure rollers' and ribbon lakes (Collins and McCrae, 1985). These ribbon lakes cover much of the western margin – coincidentally the region of lowest elevation and flow speed – forming an interconnected hydrological network of shallow lakes (Figure 9b), while globular lakes dominate GVI's eastern margin. This shows that flow direction defines lake types on GVI and therefore acts as a factor in enhancing stability, as shallow, widespread ribbon lakes are much less likely to englacially drain as they spread water across a wider area. This leads to fewer deep lakes, and a lesser likelihood of clusters, thus increasing ice shelf stability. This can be extended to other ice shelves, with Amery ice shelf, East Antarctica showing ribbon lakes (Bell et al., 2018), indicating a degree of stability against collapse from englacial drainage.

### (5.3) Drainage related impacts of SGLs on GVI

Between 2000 and 2020, no englacial drainage is observed on GVI, however, between 1991 and 2000, 8 new dolines form, primarily in the south of the study area. This means that, while rare, englacial drainage does occur on GVI in isolated locations during extended warm periods such as 1980-2000 (Figure 16a). Englacial drainage is an important factor in the instability of some ice shelves (Stokes et al., 2019; Banwell et al., 2013), for example, Larsen B, which experienced significant hydrofracture of clustered prior to its collapse at the end of the 1980-2000 warm period (Leeson et al., 2020; Turner et al., 2016). Thus, while uncommon, GVI shows some vulnerability to englacial drainage and hydrofracture. During the 1980-2000 warm period there was a minor increase in vulnerability, with only 8 new dolines appearing over a 9 year period, with possibly more forming and closing due to a lack of imagery between 1991 and 2000, therefore indicating that a greater magnitude of increased temperature would be required for widespread instability to be realised.

Concentric lakes appear on GVI, around the relatively few permanent dolines. Figure 20 shows a clear example of these concentric melt ponds in 2017/18. The formation of concentric lakes indicates englacial drainage through flexure of the ice shelf upon drainage of SGLs (Banwell et al., 2013), thus evidencing that drainage and hydrofracture has occurred on GVI. The fractures from hydrofracturing create further instabilities through increased likelihood of englacial drainage through the rifts underneath concentric lakes, and are coined as an indicator of catastrophic ice shelf collapse on Larsen B (Banwell et al., 2013; Leeson et al., 2020). However, the flexure also uplifts the area immediately surrounding each doline, preventing further drainage through the central depression, evidenced in this study by a lack of water in many permanent dolines on GVI. This is important as it shows that, while englacial

drainage has occurred in the past on GVI, it has been minor and isolated, during a period that neighbouring ice shelves such as Larsen B experienced catastrophic collapse.

Drainage on GVI does appear to occur supraglacially however, as a large-scale event was observed in 2019 (Figure 19). However, this feature rather than influencing stability through eventual englacial drainage, refroze by the end of the melt season. Additionally, large numbers of channels found along the western margin of GVI in the region of predominantly ribbon lakes suggests that this form of drainage, insofar as transmitting water across the surface to other lakes, is relatively common. Supraglacial drainage is an important aspect of hydrology on GVI, however it also indicates stability, as supraglacial flow and drainage is less damaging to the structural integrity of the ice shelf than englacial drainage.

#### (5.4) Albedo related impacts of SGLs on GVI

Albedo relates closely to lake density, producing an  $R^2$  value of 0.95. Decreases in albedo cause increases in lake basin ablation due to the higher degree of absorbed energy. Previous studies have found that deep lakes (> 4 m) result in roughly twice the lake basin ablation of bare ice (Tedesco et al., 2012; Leeson et al., 2015). Therefore, a relationship between ice shelf reflectivity and lake density is indicated, meaning that increases in lake density, lead to decreases in ice shelf reflectivity. This leads to increased melting due to increased insolation being absorbed rather than reflected. The formation of large, shallow areas of ribbon lakes on GVI shows that the average decrease in reflectivity on GVI is relatively low, compared to an ice shelf that shows more deep than shallow lakes. This is evidenced by the maximum change in albedo during 2020 being 0.04, from 0.85 to 0.81 across the northern sector's entire area. A small change in albedo can be significant, leading to increased melt feedback loops (Berlatsky, 2011). However due to the annual cycle of lakes on GVI, this change is temporary on a scale of 1-2 months at peak lake density, and hence unlikely to enhance instability.

Local changes in albedo on GVI are more pronounced, as the small number of deeper lakes reflect much less incoming radiation. Most lakes across GVI are ~1 m deep, with a small number of values exceeding 4 m in each year, typically one or two orders of magnitude fewer than the average. As such, the deepest lakes represent the greatest change in albedo, but on a small scale at several different isolated points. The high melt of these lakes thanks to their low albedo makes them more likely to englacially drain once they have melted through the ice shelf. However, due to the relative rarity of deep lakes on GVI versus shallow ribbon lakes, albedo driven englacial drainage is rare. Thus, the small change in total albedo across the northern sector of GVI may be a symbol of stability, as despite there being ~12% lake density in extreme years such as 2020, very little change in albedo (-0.04) is observed as lakes are shallow.

#### (5.5) Limitations & Avenues for Future Work

Several limitations of this study emerge from a lack of data available at temporal resolutions below the weekly scale. Optical satellite imagery encounters this issue frequently. In more recent years, S2 and L8 has allowed for a roughly weekly return time of imagery, however due to the relatively high propensity for cloud cover on GVI, many of these images are non-viable for identifying lakes. LS7 shows this issue to be exacerbated when only one satellite with a 16-day return period is available, providing even fewer viable tiles for study. Furthermore, the satellite record prior to 1999/2000 displays even patchier data, with no available imagery between 1991 and 1997, with 154 tiles covering the entire 1980-1999 period, of which only 21 are viable for study, and only 8 contain lakes with no major cloud

cover. The temporal limitation of optical imagery has led to a lack of ability to observe short-term events on GVI, particularly englacial drainage, which has been observed to occur on timescales of days, rather than weeks (Banwell et al., 2014). As a result, the lack of observed englacial drainage may be a factor of satellite imagery limitations, rather than a lack of occurrence.

Further limitations of imagery come from LS7, which displayed a scanline error for much of its lifespan, while not being problematic for running NDWI calculations, this error limited the usefulness of LS7 tiles. A significant degree of post-processing was required to remove artefacts from scanlines merging with lake polygons (Figure 5b). Furthermore, division of lakes through scanlines led to lake count values being inaccurate, and made calculations of lake depth and albedo problematic, as interference from scanline artefacts would need to be accounted for. Scanlines particularly limited the albedo calculations, as large quantities of incorrect reflectivity values from misaligned LS7 bands would need to be corrected for. This led to albedo values from 2020 having significant leverage on the calculated albedo dataset.

Resolution of imagery proved sufficient for this study, covering all lakes above 1800 m<sup>2</sup> accurately, with LS4-8's minimum resolution of 30 m<sup>2</sup>. However, pan-sharpening of the Landsat imagery would have increased accuracy on lake areas across the board, as it would have brought the minimum lake area to 450 m<sup>2</sup> (2px at 15 m<sup>2</sup>), increasing the accuracy of the dataset. This was unnecessary for studying lakes; however it would prove useful in a future study considering supraglacial drainage channels in addition to lakes. Such a study would shed more light on the mechanisms of drainage on GVI, identifying if channels narrower than 30 m<sup>2</sup> drain laterally or into dolines, and therefore identifying further aspects of ice shelf stability.

A second approach to this study would involve SAR data, as the main problem was with satellite imagery data collection, particularly due to cloud cover. SAR data would negate this issue as it penetrates cloud, hence improving the usefulness and overall, the temporal resolution of the dataset. Temporal resolution would be improved by SAR data, through adding additional tiles per month (4-5 in addition to optical). This would lessen the impact of cloud on skew in the dataset, allowing more months to have "mid-month" sampling rather than uneven sampling in consecutive years. SAR would further address the LS7 scanline problem by providing full tiles across the study area during the same period. An initial approach would involve using data from Branson, (2019) and Freer, (2020), but taking a multi-decade approach rather than single or few years. Sentinel 3 data would further be useful in albedo change calculations, as it would first expand the data available for albedo calculations into the LS7 era; and provide more accurate point and cross-shelf albedo values with an established methodology (Kokhanovsky et al., 2019).

A future study into the cause of varying peak values on GVI would be an interesting use of greater temporal sampling, as the cause of some years to have peak values in February over January is inconclusive. An analysis of all climatic variables affecting GVI on a daily or weekly temporal scale as opposed to the wider monthly-annual scales used in this study may identify a cause of this variation. This could be coupled with an investigation into the delay in lake density versus melt peak as found in Figure 13b, as there may be a degree of coupling between average melt increasing in February, and a February peak lake density value.

Finally, future study comparing GVI to a neighbouring contemporary ice shelf would be particularly interesting in understanding how the topographic constraints of Alexander Island and the AP influence GVI's stability. Similar processes to those used in this study could

be carried out for Wilkins ice shelf, due to proximity to GVI. This would address the apparent robustness of GVI to climatic forcing not seen on nearby ice shelves such as Larsen B in terms of the atypical, constrained nature of GVI rather than the typical fan-shape of most ice shelves. Particular attention would be on englacial drainage, lake density and year to year persistence of lakes, similarly to Leeson et al., (2020). Thus, the influence of GVI's topographic constraints of Alexander Island and Palmer land on stability could be determined if a difference is observed.

#### *(5.5.1) Method Development*

A key limitation of the methods used involves validation of lake data, as quantifying uncertainty of the automated method is difficult, and only as good as the quality of manual delineation. Unknown areal uncertainty from this, when coupled with depth uncertainties from the depth retrieval methods used (Box and Ski, 2007) can raise questions about the validity of each result. Comparisons versus manual delineation however with an established methodology are a standard practice (Leeson et al., 2020) within this area of study. However, future studies may benefit from having a sample of true lake measurements to standardise automated methods against. Additionally, LiDAR data may prove useful in a future study to determine more accurate lake depths from satellite imagery, nullifying unknown uncertainties (Mitchell et al., 2010).

Another approach within future work would be to use a more advanced NDWI technique to further limit false positives and negatives within data. GVI does not have large quantities of blue ice across its surface, so corrections would be focused on the harshness of lake boundaries, along with misidentification of deep crevasses and flecks of light, patchy cloud. This would be coupled with a more automated approach to the dataset, running NDWI on all available tiles as a single process, rather than a process for each melt season. This would both speed up processing, and with the suggested improvements, increase the accuracy and validity of the output data beyond that of the current methods used.

## **(6.0) Conclusions**

This thesis has demonstrated the value of optical satellite imagery in monitoring SGLs on Antarctic ice shelves over inter-annual, intra-annual and decadal timescales. It has additionally identified the usefulness of additional datasets recording climate, and glaciological variables in analysis of the impact of SGLs observed through imagery. The value of a multiple temporal scale approach is demonstrated, identifying factors such as summer precipitation and decadal temperature averages as controlling factors in SGL formation and persistence, while also producing a catalogue of SGLs over several decades. High decadal average temperatures are found to increase the annual persistence of SGLs, whilst increased summer precipitation limits lake formation.

Results from this study have developed a detailed understanding of GVI's stability on varying temporal scales, showing that in recent years GVI is stable against SGL induced instability, as no new drainage features are observed over the 2000-2020 study. Furthermore, pre-2000 imagery and climate data shows that GVI has experienced persistent lake presence in the past, during the same period as Larsen B (Turner et al., 2016; Leeson et al., 2020). In addition, between this period and 2000, new drainage features are observed to have formed on GVI, showing this as a period of increased drainage and lake presence, corresponding to

a warmer period than present due to changes in the southern annular mode. While this indicates a difference in stability between Larsen B and GVI, as the former collapsed during the same period, further study would be required to understand this.

SGLs on GVI are observed here to be primarily ribbon-like (~80% of observed features), meaning shallow lakes with a large surface area, with low propensity for englacial drainage. These are likely produced due to the compressional flow regime of GVI, forming pressure rollers in the ice flow (Collins and McCrae, 1985). Globular, deeper lakes are much less common, often forming away from compressional flow, making up only 20% of observed lakes. This is an important finding, as ribbon lakes are shallower than globular lakes, and thus less likely to melt through the ice causing hydrofracture, in addition to this, ribbon lakes are relatively rare versus globular lakes in current observations of Antarctica. During melt seasons of high lake density, ribbons form an interconnected lake network, spanning much of GVI's northern sector's surface. High lake density years in this case correspond to over 5% lake coverage, as observed in 1989-1991, 2005, 2007, 2009-2010 and 2020. In particular, 1989-1991 show values as severe as 2010 and 2020, while also being persistent year on year rather than a single occurrence, showing that while the extreme values observed in 2020 are unusual for the time period, they have occurred previously on GVI.

Lake induced instability operates primarily through drainage, causing hydrofracture and ice shelf flexure (Banwell et al., 2013). However, due to the low number of observations of drainage features on GVI, hydrofracture appears rare but present on GVI as dolines and concentric ring lakes are observed around isolated dolines. Thus, this study finds GVI to be currently robust to clustered lake drainage and hydrofracture as observed on Larsen B (Leeson et al., 2020), due to the rarity and isolated nature of dolines. This may change in future, with increased warming, and thus a greater propensity for year-on-year lake persistence. Furthermore, lateral drainage is observed during a single event in 2019 during this study. However, water is not observed leaving the ice shelf surface, laterally or via a doline. Hence, supraglacial hydrology on GVI is found in this study to be an enclosed system, with little meltwater leaving the ice shelf either in a damaging manner (englacially via dolines and hydrofracture) or otherwise.

This thesis is the first long-term, multi-temporal scale analysis of SGLs on GVI using optical imagery. Previous studies have primarily focused on a single or short set of years (Labarbera and Macayeal, 2011), or focused on ice shelf fracturing (Holt et al., 2013). The results of this thesis identify the potential of this approach, as in addition to producing a catalogue of lake features, this study has shown that on ice shelves with low levels of blue ice, simplistic Green and Near Infrared NDWI methods can be used successfully for lake delineation without further modification. Long-term studies of this nature have been carried out for other ice shelves, including Larsen A, Riiser-Larsen, Roi Baudoin, Amery (Arthur et al., 2020; Kingslake et al., 2018), and particularly Larsen B, with studies such as Leeson et al., 2020 covering 1979 to 2002. Hence, this study provides a similar level of detail for GVI. Non-optical studies have been carried out on GVI on short temporal scales, using C-Band SAR data (Branson, 2019; Freer, 2020), however these focus on lake backscatter, rather than the impacts of lakes.

Additionally, previous studies have identified and catalogued lakes across many Antarctic ice shelves, including GVI (Stokes et al., 2019; Kingslake et al., 2017). However, many of these studies focus on a single timescale, rather than a combined approach. Hence, this thesis' combined look at lakes on monthly, annual and decadal scales on GVI is one of few similar studies across Antarctica (Leeson et al., 2020; Arthur et al., 2020; Langley et al.,

2016). This is important as it shows the interlinked nature between each controlling variable, such as temperature, precipitation and glaciological controls across different timescales, hence providing a monthly-scale picture of how GVI's supraglacial hydrology functions. Furthermore, it shows the viability of the processes used, with only some changes needed to be applied to other regions, such as blue-ice correction within NDWI.

The methods developed in this study show great effectiveness in analysing ice shelf properties and supraglacial hydrology in the polar regions and will become increasingly important in the future as warming continues. Melting is projected to increase over the twentieth century (Naughten et al., 2018), and as satellite data improves and becomes more valuable in researching polar environments, the methods developed in this thesis will assist in studying the ongoing change. Hence, this thesis contributes a valuable in-depth analysis of GVI, along with an effective methodology for understanding glacial hydrology.

## **(7.0) References**

- Arthur, J. F., Stokes, C. R., Jamieson, S. S. R., Carr, J. R. and Leeson, A. A. (2020) 'Distribution and seasonal evolution of supraglacial lakes on Shackleton Ice Shelf, East Antarctica', *The Cryosphere*. doi: <https://doi.org/10.5194/tc-2020-101>.
- Arthur, Jennifer F et al., 2020. Recent understanding of Antarctic supraglacial lakes using satellite remote sensing. *Progress in physical geography*, p.30913332091611.
- Banwell, Alison F et al., 2014. Supraglacial lakes on the Larsen B ice shelf, Antarctica, and at Paakitsoq, West Greenland: a comparative study. *Annals of glaciology*, 55(66), pp.1–8.
- Banwell, Alison F & Macayeal, Douglas R, 2015. Ice-shelf fracture due to viscoelastic flexure stress induced by fill/drain cycles of supraglacial lakes. *Antarctic science*, 27(6), pp.587–597.
- Banwell, Alison F, MacAyeal, Douglas R & Sergienko, Olga V, 2013. Breakup of the Larsen B Ice Shelf triggered by chain reaction drainage of supraglacial lakes. *Geophysical research letters*, 40(22), pp.5872–5876.
- Bell, R. E., Banwell, A. F., Trusel, L. D. and Kingslake, J. (2018) 'ice-sheet mass balance', *Nature Climate Change*. Springer US, 8(December). doi: 10.1038/s41558-018-0326-3.
- Bell, R. E., Chu, W., Kingslake, J., Das, I., Tedesco, M., Tinto, K. J., Zappa, C. J., Frezzotti, M., Boghosian, A. and Lee, W. S. (2017) 'of meltwater in surface river', Nature Publishing Group. *Nature Publishing Group*, 544(7650), pp. 344–348. doi: 10.1038/nature22048.
- Benn, D. I. and Evans, D. J. A. (1998) *Glaciers & Glaciation*. 1st edn. Edited by J. Delf. London, New York: Arnold, Oxford University Press.
- Berlatsky, N. (2011) 'The Ice Albedo Feedback Loop', in *Water and Ice*. Detroit: Greenhaven Press, pp. 24–26. Available at: <https://link.gale.com/apps/doc/CX1740500020/GVRL?u=unilanc&sid=GVRL&xid=8532773d>.
- Berthier E. , Scambos, Ted A. & Shuman, Christopher A., 2012. Mass loss of Larsen B tributary glaciers (Antarctic Peninsula) unabated since 2002. *Geophysical research letters*, 39(13), pp.L13501-n/a.

- Box, Jason E & Ski, Kathleen, 2007. Remote sounding of Greenland supraglacial melt lakes: implications for subglacial hydraulics. *Journal of glaciology*, 53(181), pp.257–265.
- Branson, H. (2019) A multi-satellite investigation into the evolution and SAR signature of surface lakes on George VI ice shelf, West Antarctic peninsula.
- Cape, M. R et al., 2015. Foehn winds link climate-driven warming to ice shelf evolution in Antarctica. *Journal of geophysical research. Atmospheres*, 120(21), pp.11,037–11,057.
- Collins, I. F & McCrae, I. R, 1985. Creep Buckling of Ice Shelves and the Formation of Pressure Rollers. *Journal of glaciology*, 31(109), pp.242–252.
- Cook, A. J & Vaughan, D. G, 2010. Overview of areal changes of the ice shelves on the Antarctic Peninsula over the past 50 years. *The cryosphere*, 4(1), pp.77–98.
- Copernicus Climate Change Service (C3S) (2017): ERA5: Fifth generation of ECMWF atmospheric reanalyses of the global climate. Copernicus Climate Change Service Climate Data Store (CDS), *January 2020*. <https://cds.climate.copernicus.eu/cdsapp#!/home>
- Das, S. B et al., 2008. Fracture Propagation to the Base of the Greenland Ice Sheet During Supraglacial Lake Drainage. *Science (American Association for the Advancement of Science)*, 320(5877), pp.778–781.
- Dell, R., Willis, I., Arnold, N., Banwell, A., Pritchard, H. and Ruth, A. (2020) ‘Temporal variations in the surface hydrology across Antarctic ice shelves’, p. 9856.
- Dunmire, D., Lenaerts, J. T. M., Banwell, A. F., Wever, N. and Shragge, J. (2020) ‘Observations of buried lake drainage on the Antarctic Ice Sheet’. doi: 10.1029/2020GL087970.
- ESA (2019) ESA Sentinel Online Technical Guides, Sentinel Online. Available at: <https://sentinel.esa.int/web/sentinel/sentinel-technicalguides;jsessionid=BA00EE6776881B0A733487743C3F5BDB.jvm1> (Accessed: 2 December 2019).
- Freer, B. (2020) A multi-year assessment of the extent and evolution of surface lakes on the George VI ice shelf, Antarctic Peninsula, as detected by Synthetic Aperture Radar (SAR).
- Hambrey, Michael J et al., 2015. Structure and sedimentology of George VI Ice Shelf, Antarctic Peninsula: implications for ice-sheet dynamics and landform development. *Journal of the Geological Society*, 172(5), pp.599–613.
- Harper, J., Humphrey, N., Pfeffer, W. T., Brown, J. and Fettweis, X. (2012) ‘Greenland ice-sheet contribution to sea-level rise buffered by meltwater storage in firn’. *Nature*, (V) pp. 3–6. doi: 10.1038/nature11566.
- Holt, T. O., Glasser, N. F., Quincey, D. J. and Siegfried, M. R. (2013) ‘Speedup and fracturing of George VI Ice Shelf, Antarctic Peninsula’, *The cryosphere* 7(1), pp. 797–816. doi: 10.5194/tc-7797-2013.
- Humbert, A., 2007. Numerical simulations of the ice flow dynamics of George VI Ice Shelf, Antarctica. *Journal of glaciology*, 53(183), pp.659–664.
- Ihlen, V. and Zanter, K. (2019) ‘Landsat 8 (L8) Data Users Handbook’, 8(November). IPCC (2014) Climate Change 2014: Synthesis Report. Contribution of Working Groups I, II, and III to the Fifth Assessment Report of the Intergovernmental panel on Climate Change. Geneva.

- Ji, L., Zhang, L. and Wylie, B. (2009) 'Analysis of Dynamic Thresholds for the Normalized Difference Water Index', 75(11), pp. 1307–1317.
- Jun, C., Changqing, K. E., Xiaobing, Z. and Zhude, S. (2016) 'Surface velocity estimations of ice shelves in the northern Antarctic Peninsula derived from MODIS data', *Journal of geographical sciences*, 26(2), pp. 243– 256. doi: 10.1007/s11442-016-1266-3.
- Kingslake, Jonathan et al., 2017. Widespread movement of meltwater onto and across Antarctic ice shelves. *Nature* (London), 544(7650), pp.349–352.
- Kokhanovsky, A., Box, J. E., Vandecrux, B., Manko, K. D., Lamare, M., Smirnov, A. and Kern, M. (2020) 'The Determination of Snow Albedo from Satellite Measurements Using Fast Atmospheric Correction Technique', *Remote Sensing (Basel, Switzerland)*, 12, 2, p.234.
- Labarbera, C. H. and Macayeal, D. R. (2011) 'Traveling supraglacial lakes on George VI Ice Shelf, Antarctica', *Geophysical research letters* 38(24), pp. 1–5. doi: 10.1029/2011GL049970.
- Langley, E. S., Leeson, A. A., Stokes, C. R. and Jamieson, S. S. R. (2016) 'Seasonal evolution of supraglacial lakes on an East Antarctic outlet glacier', *Geophysical research letters*, 43(16), pp. 8563– 8571. doi: 10.1002/2016GL069511.
- Leeson, A. A., Shepherd, A., Briggs, K., Howat, I., Fettweis, X., Morlighem, M. and Rignot, E. (2015) 'Supraglacial lakes on the Greenland ice sheet advance inland under warming climate', *Nature climate change*, 5(1) pp. 18–23. doi: 10.1038/nclimate2463.
- Leeson, A. A., Foster, E., Rice, A., Gourmelen, N., van Wessem., J. M. (2020) 'Evolution of supraglacial lakes on the Larsen B ice shelf in the decades before it collapsed', *Geophysical research letters*, 47(4).
- Leeson, A. A., Shepherd, A., Sundal, A. V, Johansson, A. M., Selmes, N., Briggs, K., Hogg, A. E. and Fettweis, X. (2013) 'A comparison of supraglacial lake observations derived from MODIS imagery at the western margin of the Greenland ice sheet', *Journal of glaciology*, 59(218), pp. 1179–1188. doi: 10.3189/2013JoG13J064.
- Leppäranta, M. (2014) *Freezing of Lakes and the Evolution of their Ice Cover*. 1st edn. Berlin: Springer Science & Business Media. Available at: <https://books.google.co.uk/books?id=Gj2gBQAAQBAJ>.
- Li, W., Du, Z., Ling, F., Zhou, D., Wang, H., Gui, Y., Sun, B. and Zhang, X. (2013) 'A Comparison of Land Surface Water Mapping Using the Normalized Difference Water Index from TM, ETM+ and ALI', *Remote sensing (Basel, Switzerland)*, 5(11) pp. 5530–5549. doi: 10.3390/rs5115530.
- Liu, Z., Yao, Z. and Wang, R. (2016) 'Assessing methods of identifying open water bodies using Landsat 8 OLI imagery', *Environmental Earth Sciences*. Springer Berlin Heidelberg, 75(10), pp. 1–13. doi: 10.1007/s12665-016-5686-2.
- Macayeal, D. R., Sergienko, O. V and Banwell, A. F. (2015) 'A model of viscoelastic ice-shelf flexure', *Journal of glaciology*, 61(228), pp. 635–645. doi: 10.3189/2015JoG14J169.
- Machguth, H., Box, J. E., Fausto, R. S. and Pfeffer, W. T. (2018) 'Melt Water Retention Processes in Snow and Firn on Ice Sheets and Glaciers: Observations and Modeling', *Frontiers in earth science*, 6(July), pp. 1–3. doi: 10.3389/feart.2018.00105.

- Marshall, G. J., Orr, A., Nicole, P. M. van L. and King, J. C. (2006) 'The Impact of a Changing Southern Hemisphere Annular Mode on Antarctic Peninsula Summer Temperatures', *Journal of climate*, 19(20), pp. 5388–5404.
- Matsuoka, K., Hindmarsh, R. C. A., Moholdt, G., Bentley, M. J., Pritchard, H. D., Brown, J., Conway, H., Drews, R., Durand, G., Goldberg, D., Hattermann, T., Kingslake, J., Lenaerts, J. T. M., Martín, C., Mulvaney, R., Nicholls, K. W., Pattyn, F., Ross, N., Scambos, T., (2015) 'Earth-Science Reviews Antarctic ice rises and rumples : Their properties and significance for ice-sheet dynamics and evolution', *Earth Science Reviews*. The Authors, 150, pp. 724–745. doi: 10.1016/j.earscirev.2015.09.004.
- Mcevoy, M. and Castaner, L. (2012) 'The Role of Solar-Radiation Climatology in the Design of Photovoltaic Systems', in *Practical Handbook of Photovoltaics: Fundamentals and Applications*. 2nd edn. San Diego, p. 637. Available at: <https://ebookcentral.proquest.com/lib/lancaster/reader.action?docID=788017#>.
- Miles, K. E., Willis, I. C., Benedek, C. L., Williamson, A. G., Tedesco, M. and Miles, K. E. (2017) 'Toward Monitoring Surface and Subsurface Lakes on the Greenland Ice Sheet Using Sentinel-1 SAR and Landsat-8 OLI Imagery', *Frontiers in earth science*, 5(July), pp. 1–17. doi: 10.3389/feart.2017.00058.
- Mitchell, S., Adler, J., Thayer, J., and Hayman, M. (2010). Polarization Lidar for Shallow Water Supraglacial Lake Depth Measurement. AGU Fall Meeting Abstracts.
- Moffat, C. and Meredith, M. (2018) 'Shelf – ocean exchange and hydrography west of the Antarctic Peninsula: a review', *Philosophical Transactions of the Royal Society of London*
- Mouginot, J., Rignot, E. and Scheuchl, B. (2019) 'Continent - Wide, Interferometric SAR Phase, Mapping of Antarctic Ice Velocity.' *Geophysical Research Letters*, 46(16) pp. 9710–9718. doi: 10.1029/2019GL083826.
- Mouginot, J., E. Rignot, and B. Scheuchl. (2019). *MEaSURES Phase-Based Antarctica Ice Velocity Map, Version 1*. nsidc-0754. Boulder, Colorado USA. NASA National Snow and Ice Data Center Distributed Active Archive Center. doi: <https://doi.org/10.5067/PZ3NJ5RXRH10>. January, 2020
- Moussavi, M., Pope, A., Halberstadt, A. R. W. and Trusel, L. D. (2020) 'Antarctic Supraglacial Lake Detection Using Landsat 8 and Sentinel-2 Imagery: Towards Continental Generation of Lake Volumes'. *Remote Sensing (Basel, Switzerland)*, 12(1), p.134
- Nagler, T., Helmut, R., Ripper, E., Bippus, G. and Hetzenecker, M. (2016) 'Advancements for Snowmelt Monitoring by Means of Sentinel-1 SAR', *Remote Sensing (Basel, Switzerland)* 8(4), pp. 348. doi: 10.3390/rs8040348.
- Naughten, K. A., Meissner, K. J., Galton-Fenzi, B. K., England, M. H., Timmerman, R. and Hellmer, H. H. (2018) 'Future Projections of Antarctic Ice Shelf Melting Based on CMIP5 Scenarios', *Journal of Climate*, 31(13), pp. 5243–5261. doi: 10.1175/JCLI-D-17-0854.1.
- Pope, A., Scambos, T. A., Moussavi, M., Tedesco, M., Willis, M., Shean, D. and Grigsby, S. (2016) 'Estimating supraglacial lake depth in West Greenland using Landsat 8 and comparison with other multispectral methods', *The cryosphere*, 10(1) pp. 15–27. doi: 10.5194/tc-10-15-2016.

- Quincey, D. J., Luckman, A., Park, S. and Sa, S. (2009) 'Progress in satellite remote sensing of ice sheets', *Progress in Physical Geography* 33(4), pp. 547–567. doi: 10.1177/0309133309346883.
- Rebesco, M., Domack, E., Zgur, F., Lavoie, C., Leventer, A., Brachfeld, S., Willmott, V., Halverson, G., Truffer, M., Scambos, T., Smith, J. and Pettit, E. (2014) 'Boundary condition of grounding lines prior to collapse, Larsen-B Ice Shelf, Antarctica', *Science* 345(6202) pp.1354-1358.
- Schannwell, C., Cornford, S., Pollard, D. and Barrand, N. E. (2018) 'Dynamic response of Antarctic Peninsula Ice Sheet to collapse of Larsen C and George VI ice shelves', *The cryosphere discussions*, (February), pp. 1–30.
- Schannwell, C. (2017) 'Modelling ice dynamic sea-level rise from the Antarctic Peninsula Ice Sheet', (May).
- Steig, E. J. and Schneider, D. P. (2009) 'Warming of the Antarctic ice-sheet surface since the 1957 International Geophysical Year', *Nature* 460(7256) pp. 766
- Stokes, Chris R., Sanderson, Jack E., Miles, Bertie W. J., Jamieson, Stewart S. R., Leeson, A. A. (2019) 'Widespread distribution of supraglacial lakes around the margin of the East Antarctic Ice Sheet', *Scientific Reports*, 9(13823). doi: doi:10.1038/s41598-019-50343-5.
- Talbot, M. H. (1988) 'Oceanic environment of George vi ice shelf. Antarctic peninsula', *Annals of Glaciology*, 11, pp. 161-164.
- Tedesco, M., Lüthje, M., Steffen, K., Steiner, N., Fettweis, X., Willis, I., Bayou, N. and Banwell, A. (2012) 'Measurement and modeling of ablation of the bottom of supraglacial lakes in western Greenland', *Geophysical research letters* 39(2), pp. 1–5. doi: 10.1029/2011GL049882.
- Trusel, L. D., Frey, K. E., Das, S. B., Munneke, P. K. and Broeke, M. R. Van Den (2013) 'Satellite-based estimates of Antarctic surface meltwater fluxes', *Geophysical research letters*, 40(23), pp. 6148–6153. doi: 10.1002/2013GL058138.
- Tuckett, P. A., Ely, J. C., Sole, A. J., Wessem, J. M. Van, Howard, J., Livingstone, S. J. and Davison, B. J. (2019) 'Rapid accelerations of Antarctic Peninsula outlet glaciers driven by surface melt', *Nature Communications*. Springer US, 10(4311), pp. 1–8. doi: 10.1038/s41467-019-12039-2.
- UK Polar Data Centre, <https://data.bas.ac.uk/metadata.php?id=GB/NERC/BAS/PDC/00794>, date accessed: January 2020
- Van den Broeke, M. R. Van Den and Bamber, J. (2011) 'Ice Sheets and Sea Level: Thinking Outside the Box', *Surveys in geophysics* 32(4) pp. 495–505. doi: 10.1007/s10712-011-9137-z.
- Vaughan, D. G. (1993) 'A synthesis of reDlote sensing data on Wilkins Ice Shelf, Antarctica', (1989), *Annals of Glaciology*, pp. 211–218.
- Vaughan, D., Marshall, G., Connolley, W., Parkinson, C., Mulvaney, R., Hodgson, D., King, J., Pudsey, C. and Turner, J. (2003) 'Recent Rapid Regional Climate Warming on The Antarctic Peninsula', *Climatic Change* 60(3) BAS, NERC, pp. 243–274.

Watson, C. S., King, O., Miles, E. S. and Quincey, D. J. (2018) 'Remote Sensing of Environment Optimising NDWI supraglacial pond classification on Himalayan debris-covered glaciers', *Remote Sensing of Environment*. Elsevier, 217(August), pp. 414–425. doi:10.1016/j.rse.2018.08.020.

Wessem, J. M. Van, Meredith, M. P., Reijmer, C. H., Broeke, M. R. Van Den and Cook, A. J. (2017) 'Deep – Sea Research II Characteristics of the modelled meteoric freshwater budget of the western Antarctic Peninsula', *Deep-Sea Research Part II*. Elsevier Ltd, 139(November 2016), pp. 31–39. doi: 10.1016/j.dsr2.2016.11.001.

Williamson, A. G., Arnold, N. S., Banwell, A. F. and Willis, I. C. (2017) 'Remote Sensing of Environment A Fully Automated Supraglacial lake area and volume Tracking (“ FAST ”) algorithm : Development and application using MODIS imagery of West Greenland', *Remote Sensing of Environment*. 196, pp. 113–133. doi: 10.1016/j.rse.2017.04.032.

Williamson, A. G., Banwell, A. F., Willis, I. C. and Arnold, N. S. (2018) 'Dual-satellite (Sentinel-2 and Landsat 8) remote sensing of supraglacial lakes in Greenland', *The cryosphere* 12(9) pp. 3045– 3065.

Yang, K. and Smith, L. C. (2013) 'Supraglacial Streams on the Greenland Ice Sheet Delineated From Combined Spectral – Shape Information in High-Resolution Satellite Imagery'. *IEEE Geoscience and Remote Sensing Letters*, 10(4), pp. 801–805.

Zhiqiang Du, Wenbo Li, Dongbo Zhou, Liqiao Tian, Feng Ling, Hailei Wang, Yuanmiao Gui & Bingyu Sun (2014) Analysis of Landsat-8 OLI imagery for land surface water mapping, *Remote Sensing Letters*, 5:7, 672-681, DOI: 10.1080/2150704X.2014.960606

Wessem, J. M. Van, Berg, W. J. Van De, Noël, B. P. Y., Meijgaard, E. Van, Jakobs, C. L., Krüger, K., Lenaerts, J. T. M., Lhermitte, S., Ligtenberg, S. R. M., Medley, B., Reijmer, C. H., Tricht, K. Van, Trusel, L. D., Ulft, L. H. Van, Wouters, B., Wuite, J. and Broeke, M. R. Van Den (2017) 'Modelling the climate and surface mass balance of polar ice sheets using RACMO2 , part 2 : Antarctica ( 1979 – 2016 ).', *The Cryosphere* 12(4), pp. 1479-1498.

World Wildlife Fund, Hogan, C. M. and Draggan, S. (2013) 'World and Wildlife Fund', *The Encyclopedia of Earth*. Available at: [https://editors.eol.org/eoearth/wiki/Antarctic\\_Peninsula](https://editors.eol.org/eoearth/wiki/Antarctic_Peninsula).

**APPENDIX 1** - Tiles used during the study, including designation and date of retrieval. Data sourced from USGS data store (USGS, <https://earthexplorer.usgs.gov>, January 2020)

YEAR	DESIGNATION	MONTH/DAY	FULL DESIGNATION	SATELLITE
2019/20	215110	2019-12-27	LC08_L1GT_215110_20191227_20200110_01_T2	LS8
2019/20	215111	2019-12-27	LC08_L1GT_215111_20191227_20200110_01_T2	LS8
2019/20	218110	2019-12-26	LC08_L1GT_218110_20191216_20191226_01_T2	LS8
2019/20	T19DEA	2020-01-19	L1C_T19DEA_A014993_20200119T131902	S2
2019/20	T19DEB	2020-01-19	L1C_T19DEB_A014993_20200119T131902	S2
2018/19	T19DEA	2018-12-15	L1C_T19DEA_A009273_20181215T131902	S2
2018/19	T19DEB	2018-12-15	L1C_T19DEB_A009273_20181215T131902	S2
2018/19	T19DEA	2019-01-04	L1C_T19DEA_A009559_20190104T131907	S2
2018/19	T19DEB	2019-01-04	L1C_T19DEB_A009559_20190104T131907	S2
2018/19	215111	2019-01-25	LC08_L1GT_215111_20190125_20190206_01_T2	LS7
2018/19	T19DEB	2019-01-28	L1C_T19DEB_A009902_20190128T125904	S2
2018/19	218110	2019-02-15	LC08_L1GT_218110_20190215_20190222_01_T2	LS7
2018/19	T19DEB	2019-02-17	L1C_T19DEB_A010188_20190217T130138	S2
2018/19	216111	2019-02-17	LC08_L1GT_216111_20190217_20190222_01_T2	LS7
2018/19	T19DEB	2019-02-27	L1C_T19DEB_A010331_20190227T125953	S2
2018/19	217110	2019-02-24	LC08_L1GT_217110_20190224_20190308_01_T2	LS8
2018/19	T19DEA	2019-02-07	L1C_T19DEA_A010045_20190207T125904	S2
2018/19	T19DEB	2019-02-07	L1C_T19DEB_A010045_20190207T125904	S2
2018/19	216111	2019-03-21	LC08_L1GT_216111_20190321_20190403_01_T2	LS8
2018/19	216110	2019-03-21	LC08_L1GT_216110_20190321_20190403_01_T2	LS8
2017/18	216111	2017-12-28	LC08_L1GT_216111_20171228_20180103_01_T2	LS8
2017/18	218109	2017-12-26	LC08_L1GT_218109_20171226_20180103_01_T2	LS8
2017/18	218110	2017-12-26	LC08_L1GT_218110_20171226_20180103_01_T2	LS8
2017/18	T19DEA	2018-01-14	L1C_T19DEA_A013391_20180114T132158	S2
2017/18	T19DEB	2018-01-14	L1C_T19DEB_A013391_20180114T132158	S2
2017/18	T19DEA	2018-02-07	L1C_T19DEA_A013734_20180207T125900	S2
2017/18	T19DEA	2018-02-04	L1C_T19DEA_A013691_20180204T124902	S2
2017/18	T19DEB	2018-02-07	L1C_T19DEB_A013734_20180207T125900	S2
2017/18	T19DEB	2018-02-21	L1C_T19DEB_A005026_20180221T133139	S2
2017/18	T19DEA	2018-03-14	L1C_T19DEA_A005326_20180314T125856	S2
2017/18	T19DEB	2018-03-30	L1C_T19DEB_A005555_20180330T131905	S2
2016/17	218109	2016-12-23	LC08_L1GT_218109_20161223_20170315_01_T2	LS8
2016/17	218110	2016-12-23	LC08_L1GT_218110_20161223_20170315_01_T2	LS8
2016/17	T19DEA	2016-12-20	L1C_T19DEA_A007814_20161220T131902	S2
2016/17	T19DEB	2016-12-20	L1C_T19DEB_A007814_20161220T131902	S2
2016/17	216110	2017-01-10	LC08_L1GT_216110_20170110_20170311_01_T2	LS8
2016/17	216111	2017-01-10	LC08_L1GT_216111_20170110_20170311_01_T2	LS8
2016/17	T19DEA	2017-02-28	L1C_T19DEA_20170228T131902	S2
2016/17	T19DEB	2017-02-28	L1C_T19DEB_20170228T131902	S2
2016/17	T19DEB	2017-03-30	L1C_T19DEB_A009244_20170330T131904	S2
2016/17	T19DEB	2017-03-30	L1C_T19DEB_A009244_20170330T132212	S2
2016/17	219109	2017-03-04	LC08_L1GT_219109_20170304_20170316_01_T2	LS8
2016/17	219110	2017-03-04	LC08_L1GT_219110_20170304_20170316_01_T2	LS8
2016/17	214111	2017-03-01	LC08_L1GT_214111_20170301_20170316_01_T2	LS8
2015/16	218109	2015-12-05	LC08_L1GT_218109_20151205_20170401_01_T2	LS8
2015/16	2108110	2015-12-05	LC08_L1GT_218110_20151205_20170401_01_T2	LS8
2015/16	219109	2016-01-13	LC08_L1GT_219109_20160113_20170405_01_T2	LS8

2015/16	219110	2016-01-13	LC08_L1GT_219110_20160113_20170405_01_T2	LS8
2015/16	216111	2016-01-08	LC08_L1GT_216111_20160108_20170405_01_T2	LS8
2015/16	217112	2016-02-16	LC08_L1GT_217112_20160216_20170329_01_T2	LS8
2015/16	216111	2016-02-09	LC08_L1GT_216111_20160209_20170330_01_T2	LS8
2015/16	216110	2016-02-09	LC08_L1GT_216110_20160209_20170330_01_T2	LS8
2015/16	217110	2016-02-16	LC08_L1GT_217110_20160216_20170329_01_T2	LS8
2015/16	215111	2016-03-21	LC08_L1GT_215111_20160321_20170327_01_T2	LS8
2015/16	217110	2016-03-19	LC08_L1GT_217110_20160319_20170328_01_T2	LS8
2014/15	217110	2014-12-27	LC08_L1GT_217110_20141227_20170415_01_T2	LS8
2014/15	218110	2015-01-03	LC08_L1GT_218110_20150103_20170415_01_T2	LS8
2014/15	218109	2015-01-03	LC08_L1GT_218109_20150103_20170415_01_T2	LS8
2014/15	217110	2015-01-28	LC08_L1GT_217110_20150128_20170413_01_T2	LS8
2014/15	219109	2015-02-27	LC08_L1GT_219109_20150227_20170412_01_T2	LS8
2014/15	218110	2015-02-04	LC08_L1GT_218110_20150204_20170413_01_T2	LS8
2014/15	218110	2015-03-08	LC08_L1GT_218110_20150308_20170412_01_T2	LS8
2014/15	217110	2015-03-17	LC08_L1GT_217110_20150317_20170412_01_T2	LS8
2013/14	218110	2013-12-31	LC08_L1GT_218110_20131231_20170427_01_T2	LS8
2013/14	215111	2013-12-26	LC08_L1GT_215111_20131226_20170427_01_T2	LS8
2013/14	218109	2013-12-31	LC08_L1GT_218109_20131231_20170427_01_T2	LS8
2013/14	214111	2014-01-04	LC08_L1GT_214111_20140104_20170427_01_T2	LS8
2013/14	219110	2014-01-07	LC08_L1GT_219110_20140107_20170427_01_T2	LS8
2013/14	215111	2014-02-10	LC08_L1GT_215111_20140212_20170425_01_T2	LS8
2013/14	217110	2014-02-10	LC08_L1GT_217110_20140210_20170425_01_T2	LS8
2013/14	219109	2014-02-08	LC08_L1GT_219109_20140208_20170426_01_T2	LS8
2013/14	215111	2014-03-16	LC08_L1GT_215111_20140316_20170425_01_T2	LS8
2013/14	219109	2014-03-12	LC08_L1GT_219109_20140312_20180528_01_T2	LS8
2013/14	219110	2014-03-28	LC08_L1GT_219110_20140328_20170424_01_T2	LS8
2013/14	218110	2014-03-05	LC08_L1GT_218110_20140305_20170425_01_T2	LS8
2012/13	215111	2012-12-15	LE07_L1GT_215111_20121215_20161128_01_T2	LS7
2012/13	216110	2012-12-22	LE07_L1GT_216110_20121222_20190516_01_T2	LS7
2012/13	218109	2012-12-04	LE07_L1GT_218109_20121204_20161127_01_T2	LS7
2012/13	218110	2012-12-04	LE07_L1GT_218110_20121204_20161127_01_T2	LS7
2012/13	216110	2013-01-07	LE07_L1GT_216110_20130107_20161126_01_T2	LS7
2012/13	216111	2013-01-07	LE07_L1GT_216111_20130107_20161126_01_T2	LS7
2012/13	218110	2013-02-22	LE07_L1GT_218110_20130222_20161125_01_T2	LS7
2012/13	218110	2013-03-10	LE07_L1GT_218110_20130310_20161125_01_T2	LS7
2012/13	216110	2013-03-12	LE07_L1GT_216110_20130312_20161126_01_T2	LS7
2011/12	216111	2011-12-20	LE07_L1GT_216111_20111220_20161204_01_T2	LS7
2011/12	216110	2011-12-20	LE07_L1GT_216110_20111220_20161204_01_T2	LS7
2011/12	218109	2012-01-03	LE07_L1GT_218109_20120103_20161203_01_T2	LS7
2011/12	218110	2012-01-03	LE07_L1GT_218110_20120103_20161203_01_T2	LS7
2011/12	215111	2012-02-15	LE07_L1GT_215111_20120215_20161203_01_T2	LS7
2011/12	217110	2012-02-13	LE07_L1GT_217110_20120213_20161203_01_T2	LS7
2011/12	220109	2012-02-18	LE07_L1GT_220109_20120218_20161203_01_T2	LS7
2011/12	216111	2012-03-09	LE07_L1GT_216111_20120309_20161203_01_T2	LS7
2010/11	217110	2010-12-24	LE07_L1GT_217110_20101224_20161211_01_T2	LS7
2010/11	217111	2010-12-24	LE07_L1GT_217111_20101224_20161211_01_T2	LS7
2010/11	220109	2010-12-29	LE07_L1GT_220109_20101229_20161211_01_T2	LS7
2010/11	217109	2011-01-25	LE07_L1GT_217109_20110125_20161210_01_T2	LS7
2010/11	217110	2011-01-25	LE07_L1GT_217110_20110125_20161210_01_T2	LS7

2010/11	217111	2011-01-25	LE07_L1GT_217111_20110125_20161211_01_T2	LS7
2009/10	215111	2009-12-23	LE07_L1GT_215111_20091223_20161216_01_T2	LS7
2009/10	217110	2010-01-06	LE07_L1GT_217110_20100106_20161216_01_T2	LS7
2009/10	216111	2010-01-15	LE07_L1GT_216111_20100115_20161217_01_T2	LS7
2009/10	218110	2010-01-29	LE07_L1GT_218110_20100129_20161217_01_T2	LS7
2009/10	214111	2010-02-02	LE07_L1GT_214111_20100202_20161215_01_T2	LS7
2009/10	215111	2010-02-09	LE07_L1GT_215111_20100209_20161216_01_T2	LS7
2009/10	218109	2010-02-14	LE07_L1GT_218109_20100214_20161216_01_T2	LS7
2009/10	220109	2010-02-12	LE07_L1GT_220109_20100212_20161215_01_T2	LS7
2009/10	217110	2010-03-11	LE07_L1GT_217110_20100311_20161215_01_T2	LS7
2009/10	217111	2010-03-11	LE07_L1GT_217111_20100311_20161216_01_T2	LS7
2008/09	217110	2008-12-18	LE07_L1GT_217110_20081218_20161223_01_T2	LS7
2008/09	217111	2008-12-18	LE07_L1GT_217111_20081218_20161223_01_T2	LS7
2008/09	220109	2008-12-07	LE07_L1GT_220109_20081207_20161223_01_T2	LS7
2008/09	217110	2009-01-19	LE07_L1GT_217110_20090119_20161222_01_T2	LS7
2008/09	218110	2009-01-10	LE07_L1GT_218110_20090110_20161223_01_T2	LS7
2008/09	215111	2009-01-05	LE07_L1GT_215111_20090105_20161223_01_T2	LS7
2008/09	216110	2009-02-13	LE07_L1GT_216110_20090213_20161222_01_T2	LS7
2008/09	216111	2009-02-13	LE07_L1GT_216111_20090213_20161222_01_T2	LS7
2008/09	218110	2009-02-11	LE07_L1GT_218110_20090211_20161222_01_T2	LS7
2008/09	219109	2009-03-06	LE07_L1GT_219109_20090306_20161221_01_T2	LS7
2008/09	219110	2009-03-06	LE07_L1GT_219110_20090306_20161221_01_T2	LS7
2007/08	215110	2007-12-18	LE07_L1GT_215110_20071218_20161231_01_T2	LS7
2007/08	215111	2007-12-18	LE07_L1GT_215111_20071218_20170101_01_T2	LS7
2007/08	216110	2007-12-09	LE07_L1GT_216110_20071209_20170101_01_T2	LS7
2007/08	218110	2007-12-23	LE07_L1GT_218110_20071223_20161231_01_T2	LS7
2007/08	216111	2008-01-10	LE07_L1GT_216111_20080110_20161231_01_T2	LS7
2007/08	218109	2008-01-08	LE07_L1GT_218109_20080108_20161231_01_T2	LS7
2007/08	218110	2008-01-08	LE07_L1GT_218110_20080108_20161231_01_T2	LS7
2007/08	214111	2008-02-29	LE07_L1GT_214111_20080229_20161230_01_T2	LS7
2006/07	217110	2006-12-13	LE07_L1GT_217110_20061213_20170106_01_T2	LS7
2006/07	217110	2006-12-29	LE07_L1GT_217110_20061229_20170105_01_T2	LS7
2006/07	217111	2006-12-29	LE07_L1GT_217111_20061229_20170105_01_T2	LS7
2006/07	216110	2007-01-07	LE07_L1GT_216110_20070107_20170105_01_T2	LS7
2006/07	216111	2007-01-07	LE07_L1GT_216111_20070107_20170105_01_T2	LS7
2006/07	217110	2007-01-30	LE07_L1GT_217110_20070130_20170105_01_T2	LS7
2006/07	216110	2007-02-08	LE07_L1GT_216110_20070208_20170104_01_T2	LS7
2006/07	216111	2007-02-08	LE07_L1GT_216111_20070208_20170104_01_T2	LS7
2006/07	220109	2007-02-04	LE07_L1GT_220109_20070204_20170105_01_T2	LS7
2005/06	216110	2005-12-03	LE07_L1GT_216110_20051203_20170111_01_T2	LS7
2005/06	216111	2005-12-03	LE07_L1GT_216111_20051203_20170112_01_T2	LS7
2005/06	218109	2005-12-17	LE07_L1GT_218109_20051217_20170111_01_T2	LS7
2005/06	218110	2005-12-17	LE07_L1GT_218110_20051217_20170112_01_T2	LS7
2005/06	217110	2006-01-27	LE07_L1GT_217110_20060127_20170110_01_T2	LS7
2005/06	218109	2006-01-18	LE07_L1GT_218109_20060118_20170111_01_T2	LS7
2005/06	218110	2006-01-18	LE07_L1GT_218110_20060118_20170111_01_T2	LS7
2005/06	217110	2006-02-28	LE07_L1GT_217110_20060228_20170110_01_T2	LS7
2005/06	218109	2006-02-03	LE07_L1GT_218109_20060203_20170110_01_T2	LS7
2005/06	218110	2006-02-19	LE07_L1GT_218110_20060219_20170110_01_T2	LS7
2004/05	218110	2005-01-15	LE07_L1GT_218110_20050115_20170116_01_T2	LS7

2004/05	218111	2005-01-15	LE07_L1GT_218111_20050115_20170116_01_T2	LS7
2004/05	218109	2005-01-15	LE07_L1GT_218109_20050115_20170117_01_T2	LS7
2004/05	219110	2005-02-23	LE07_L1GT_219110_20050223_20170116_01_T2	LS7
2004/05	216110	2005-03-22	LE07_L1GT_216110_20050322_20170116_01_T2	LS7
2004/05	219109	2005-03-11	LE07_L1GT_219109_20050311_20170115_01_T2	LS7
2004/05	219110	2005-03-11	LE07_L1GT_219110_20050311_20170115_01_T2	LS7
2003/04	218110	2004-01-29	LE07_L1GT_218110_20040129_20170123_01_T2	LS7
2003/04	220109	2004-01-27	LE07_L1GT_220109_20040127_20170122_01_T2	LS7
2003/04	216110	2004-02-16	LE07_L1GT_216110_20040216_20170122_01_T2	LS7
2003/04	216111	2004-02-16	LE07_L1GT_216111_20040216_20170122_01_T2	LS7
2003/04	219110	2004-02-05	LE07_L1GT_219110_20040205_20170122_01_T2	LS7
2003/04	218110	2004-03-17	LE07_L1GT_218110_20040317_20170122_01_T2	LS7
2003/04	218111	2004-03-17	LE07_L1GT_218111_20040317_20170122_01_T2	LS7
2003/04	216110	2004-03-03	LE07_L1GT_216110_20040303_20170122_01_T2	LS7
2002/03	216111	2002-12-11	LE07_L1GT_216111_20021211_20170127_01_T2	LS7
2002/03	216110	2002-12-11	LE07_L1GT_216110_20021211_20170128_01_T2	LS7
2002/03	218109	2002-12-25	LE07_L1GT_218109_20021225_20170127_01_T2	LS7
2002/03	218110	2002-12-25	LE07_L1GT_218110_20021225_20170127_01_T2	LS7
2002/03	218110	2003-01-26	LE07_L1GT_218110_20030126_20170126_01_T2	LS7
2002/03	218111	2003-01-26	LE07_L1GT_218111_20030126_20170126_01_T2	LS7
2002/03	219109	2003-01-17	LE07_L1GT_219109_20030117_20170127_01_T2	LS7
2002/03	219110	2003-01-17	LE07_L1GT_219110_20030117_20170127_01_T2	LS7
2002/03	215111	2003-01-05	LE07_L1GT_215111_20030105_20170128_01_T2	LS7
2002/03	215111	2003-02-22	LE07_L1GT_215111_20030222_20170126_01_T2	LS7
2002/03	216110	2003-02-13	LE07_L1GT_216110_20030213_20170126_01_T2	LS7
2002/03	216111	2003-02-13	LE07_L1GT_216111_20030213_20170126_01_T2	LS7
2002/03	218110	2003-02-11	LE07_L1GT_218110_20030211_20170126_01_T2	LS7
2002/03	216110	2003-03-01	LE07_L1GT_216110_20030301_20170127_01_T2	LS7
2001/02	216110	2001-12-24	LE07_L1GT_216110_20011224_20170201_01_T2	LS7
2001/02	216111	2001-12-24	LE07_L1GT_216111_20011224_20170201_01_T2	LS7
2001/02	219109	2001-12-29	LE07_L1GT_219109_20011229_20170201_01_T2	LS7
2001/02	219110	2001-12-29	LE07_L1GT_219110_20011229_20170201_01_T2	LS7
2001/02	215110	2002-01-18	LE07_L1GT_215110_20020118_20170201_01_T2	LS7
2001/02	216111	2002-01-09	LE07_L1GT_216111_20020109_20170201_01_T2	LS7
2001/02	218109	2002-01-07	LE07_L1GT_218109_20020107_20170201_01_T2	LS7
2001/02	218110	2002-01-07	LE07_L1GT_218110_20020107_20170201_01_T2	LS7
2000/01	218109	2001-01-04	LE07_L1GT_218109_20010104_20170208_01_T2	LS7
2000/01	218110	2001-01-04	LE07_L1GT_218110_20010104_20170208_01_T2	LS7
2000/01	219109	2001-01-27	LE07_L1GT_219109_20010127_20170207_01_T2	LS7
2000/01	215111	2001-01-31	LE07_L1GT_215111_20010131_20170207_01_T2	LS7
2000/01	217110	2001-02-14	LE07_L1GT_217110_20010214_20170206_01_T2	LS7
2000/01	217111	2001-02-14	LE07_L1GT_217111_20010214_20170206_01_T2	LS7
2000/01	220109	2001-02-19	LE07_L1GT_220109_20010219_20170206_01_T2	LS7
1999/2000	214111	2000-01-22	LE07_L1GT_214111_20000122_20170213_01_T2	LS7
1999/2000	217110	2000-01-27	LE07_L1GT_217110_20000127_20170213_01_T2	LS7
1999/2000	218110	2000-01-02	LE07_L1GT_218110_20000102_20170215_01_T2	LS7
1999/2000	217110	2000-02-28	LE07_L1GT_217110_20000228_20170213_01_T2	LS7
1996/97	214111	1997-01-21	LT05_L1GS_214111_19970121_20170102_01_T2	LS5
1996/97	215111	1997-01-28	LT05_L1GS_215111_19970128_20170102_01_T2	LS5
1990/91	216111	1991-02-04	LT05_L1GS_216111_19910204_20170128_01_T2	LS5

1990/91	216110	1991-02-04	LT05_L1GS_216110_19910204_20170128_01_T2	LS5
1989/90	217111	1990-01-15	LT04_L1GS_217111_19900115_20170131_01_T2	LS4
1989/90	217110	1990-01-15	LT04_L1GS_217110_19900115_20170131_01_T2	LS4
1988/99	217111	1989-01-28	LT04_L1GS_217111_19890128_20170204_01_T2	LS4
1988/99	217110	1989-01-28	LT04_L1GS_217110_19890128_20170204_01_T2	LS4
1988/99	215111	1989-01-30	LT04_L1GS_215111_19890130_20170204_01_T2	LS4
1988/99	215110	1989-01-30	LT04_L1GS_215110_19890130_20170204_01_T2	LS4

**APPENDIX 2** - Table of thresholding test process with comments describing difficulties with each corresponding method.

Cleanup refers to removal of features greater to or less than 1800m<sup>2</sup> in area.

2020 - January - T19DEA - T19DEB

Threshold	Feature Count	Area Total, m	Count (Cleanup)	Area, m (Cleanup)	Comments
0.1	258034	1384549229	17438	1308163616	Large quantities of slush and crevasse false +ves
0.2	120262	916609168	10349	884085673	Numerous crevasse false +ves + outcrops
0.3	72438	749003204	8913	729612224	Some false +ves (crevasse + outcrop)
0.4	56197	634585570	8426	619588541	Many false -ves, lakes ignored
0.5	48443	528160750	7791	515291981	Low detail, many false -ves

**APPENDIX 3** - Data removal table, representing count of polygons removed due to errors in NDWI/residual polygons from overlapping imagery, clouds, scanlines etc. Process carried out manually.

Month	Type of Data Removal						Totals
	Polycount	Scanline	Scanline Residuals	Batch Dissolve	Clouds	Calving Fronts	
Mar	182234	13907	13652	13045	8124	7126	
Feb	421608	33075	32200	28018	27685	26508	
Jan	439026	125404	125518	105947	104587	103342	
Dec	314765	16347	15584	13036	9266	9198	
Total	1357633	188733	186954	160046	149662	146174	
Percentage change (total)	0%	-86%	-86%	-88%	-89%	-89%	-89%
Features Removed since last	0	1168900	1779	26908	10384	3488	1211459
Percentage change since last	0%	-86%	-1%	-14%	-6%	-2%	

Period	Original Count	Original Area	Clip09Count	Clip09Area	Clip07Count	Clip07Area	Clip05Count	Clip05Area
Jan-20	8886	811231172.7	8056	505060903.2	8766	732475912.9	8289	605258048.2
Jan-18	3103	193865900	2804	132516651.3	3069	181582740.7	2937	147311178.4
Feb-18	5430	324645800.3	4868	210647216.9	5368	304905647.8	5101	244402577.6
			Clip09Count%	Clip09Area%	Clip07Count%	Clip07Area%	Clip05Count%	Clip05Area%
Jan-20			90.66%	62.26%	98.65%	90.29%	93.28%	74.61%
Jan-18			90.36%	68.35%	98.90%	93.66%	94.65%	75.99%
Feb-18			89.65%	64.89%	98.86%	93.92%	93.94%	75.28%
Average			90.22%	65.17%	98.80%	92.63%	93.96%	75.29%
			09Count %Δ	09Area %Δ	07Count %Δ	07Area %Δ	05Count %Δ	05Area %Δ
			-9.34%	-37.74%	-1.35%	-9.71%	-6.72%	-25.39%
			-9.64%	-31.65%	-1.10%	-6.34%	-5.35%	-24.01%
			-10.35%	-35.11%	-1.14%	-6.08%	-6.06%	-24.72%
Average			-9.78%	-34.83%	-1.20%	-7.37%	-6.04%	-24.71%

Average Data Loss	% Retained	%Δ
Area	77.69%	-22.31%
Count	94.33%	-5.67%

#### APPENDIX 4

Top Table shows the lakes removed per period using the Landast 7 masking technique. The second table shows the remaining lakes as a percentage of the original total value. The third table down thus represents the change in lake values as a percentage. Addon table (bottom) shows the average data loss, as % change in area. Areal retention is close to the figure provided by USGS for Landast 7 as given by USGS, of 78% (USGS, 2003).

Areas given in m, while count refers to the count of features observed in the ArcGIS attribute table.

## APPENDIX 5

Demonstration of the climate bias found between RACMO and real/ERA5 data. There is a clear cold bias in RACMO of  $\sim 4^{\circ}\text{C}$ . This is assumed to not affect additional data such as snowfall and melt. During the studied period, average seasonal temperatures did not surpass  $0^{\circ}\text{C}$ , however shorter-term warm periods were identified on daily to weekly scales. This bias is likely a product of RACMO 2 using a large grid size than ERA5, and due to the varying values of topographic forcing in each model.



MonoVariate	R2	X1 p
Mean Summer T (MST)	0.1645	0.0761
Mean Winter T (MWT)	0.0126	0.6468
Mean Summer P (MSP)	0.2136	0.0402
Mean Winter P (MWP)	0.0573	0.3238
Total Summer P (TSP)	0.5092	0.0006
Total Winter P (TWP)	0.0004	0.9392
Summer PDD (SPD)	0.1246	0.1383
Winter PDD (WPD)	0.0112	0.6661

BiVariate	R2	X1 P	X2 P	F sgf
MST + MSP	0.5226	0.1056	0.0029	0.0027
MST + MWP	0.1583	0.1024	0.7902	0.2520
MST + TSP	0.5526	0.2305	0.0017	0.0016
MST + TWP	0.1583	0.1024	0.7902	0.2520
MWT + MSP	0.4849	0.2300	0.0014	0.0050
MWT + MWP	0.0094	0.7078	0.9510	0.9275
MWT + TSP	0.5610	0.1882	0.0004	0.0014
MWT + TWP	0.0094	0.7078	0.9510	0.9275
MSP + MWP	0.4455	0.0025	0.5860	0.0089
TSP + TWP	0.5184	0.0008	0.5878	0.0029
MSP + SPD	0.4778	0.0046	0.2679	0.0055
MSP + WPD	0.4640	0.0020	0.3638	0.0068
MWP + SPD	0.1247	0.9669	0.1512	0.3446
MWP + WPD	0.0171	0.7613	0.6089	0.8712
TSP + SPD	0.5288	0.0019	0.4263	0.0024
TSP + WPD	0.5346	0.0006	0.3640	0.0022
TWP + SPD	0.1247	0.9669	0.1512	0.3446
TWP + WPD	0.0171	0.7613	0.6089	0.8712

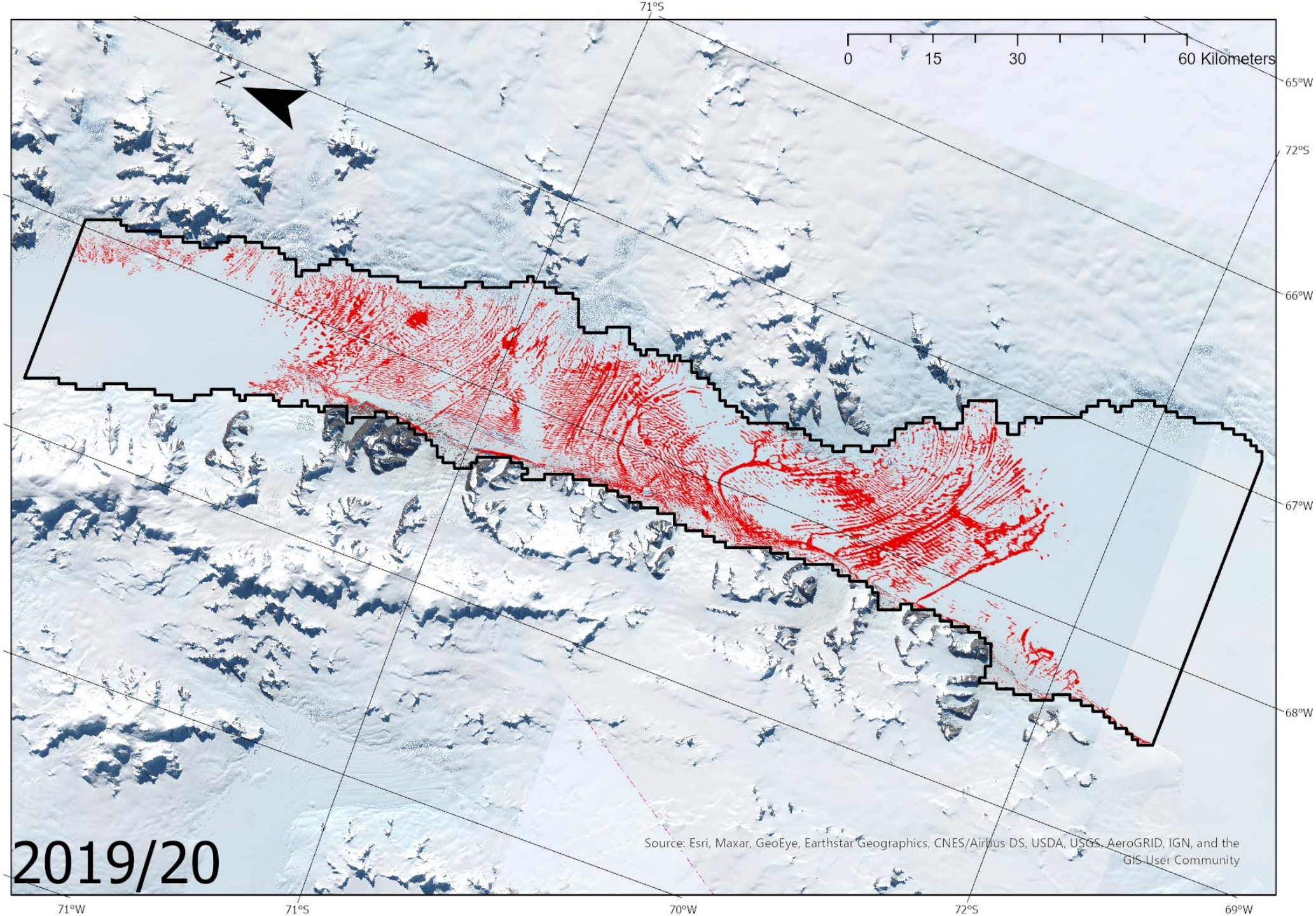
TriVariate	R2	X1 p	X2 p	X3 p	F sgf
MST + MWT + MSP	0.6144	0.0403	0.0782	0.0011	0.0021
MST + MWT + MWP	0.1962	0.0815	0.4131	0.9778	0.3365
MST + MWT + TSP	0.6317	0.1105	0.0930	0.0008	0.0015
MST + MWT + TWP	0.1962	0.0815	0.4131	0.9778	0.3365
MST + MSP + MWP	0.5398	0.1000	0.0031	0.4654	0.0074
MST + TSP + TWP	0.5656	0.2212	0.0019	0.5137	0.0049
MWT + MSP + MWP	0.4858	0.2949	0.0020	0.8711	0.0163
MWT + TSP + TWP	0.5615	0.2437	0.0006	0.9064	0.0052
SPD + MSP + MWP	0.4862	0.2926	0.0054	0.6265	0.0162
WPD + MSP + MWP	0.4645	0.4770	0.0030	0.9136	0.0217
SPD + TWP + TSP	0.5365	0.4563	0.6259	0.0024	0.0078
WPD + TWP + TSP	0.5350	0.4755	0.9093	0.0010	0.0080
SPD + WPD + TSP	0.5365	0.4563	0.6259	0.0024	0.0078
SPD + WPD + TWP	0.1292	0.1849	0.7839	0.8701	0.5435
SPD + WPD + MSP	0.4966	0.3404	0.4658	0.0047	0.0140
SPD + WPD + MWP	0.1292	0.1849	0.7839	0.8701	0.5435

QuadVariate	R2	X1 p	X2 p	X3 p	X4 p	F sgf
MST + MWT + MSP + MWP	0.6156	0.0473	0.1187	0.0016	0.8337	0.0066
MST + MWT + TSP + TWP	0.6322	0.1231	0.1337	0.0011	0.8891	0.0049
SPD + WPD + TSP + TWP	0.5476	0.5427	0.5668	0.0029	0.9542	0.0187
SPD + WPD + MSP + MWP	0.4966	0.3606	0.5997	0.0065	0.9810	0.0367

**APPENDIX 6** - Tables of results from multivariate climate analysis versus lake density. Acronyms are defined in the monivariate analysis, and values in red show significant relationships. All other values are non-significant. R<sup>2</sup> values are in the first column, while "Xn p" represents each variable. F sgf is the F value from regression analysis output.

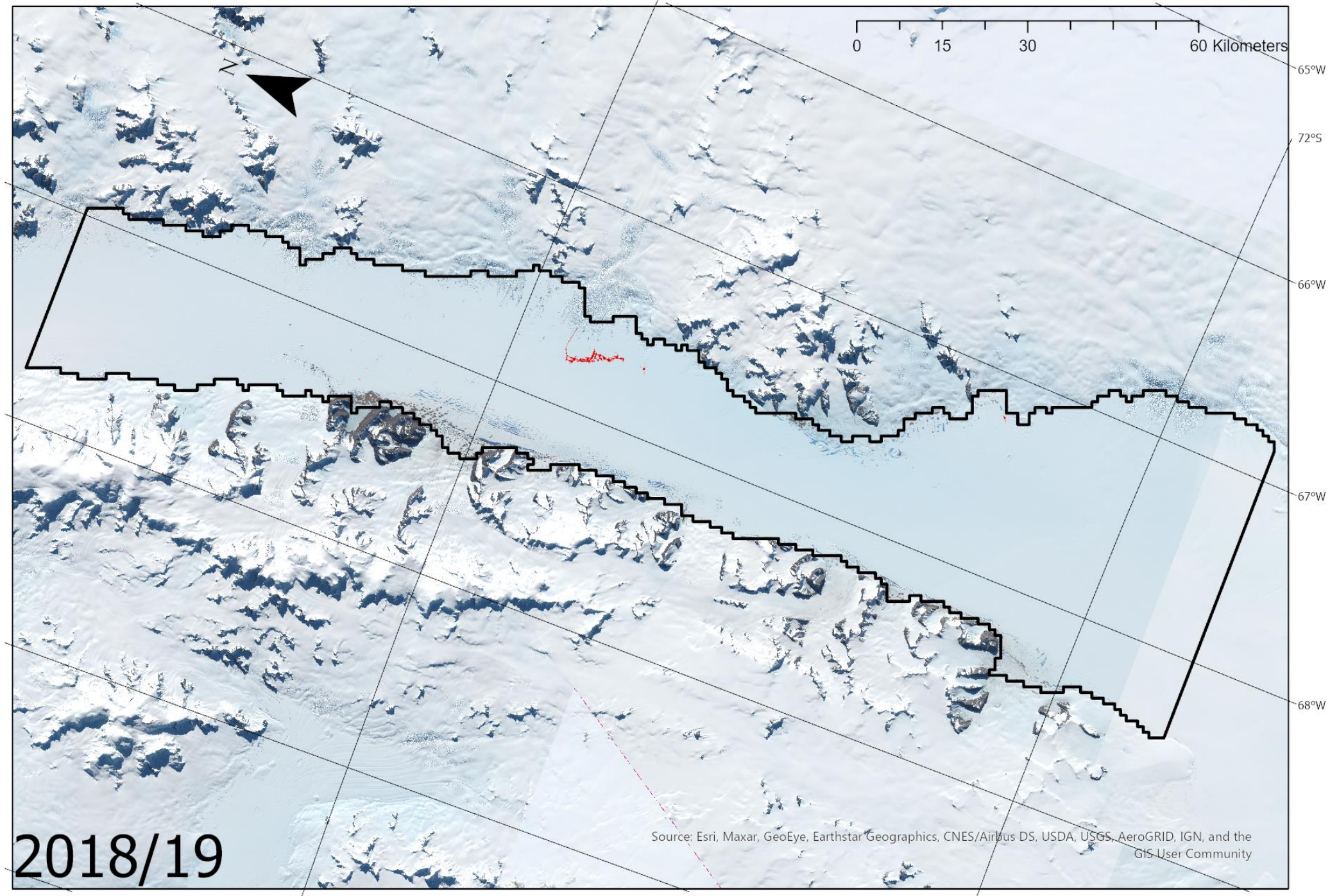
## APPENDIX 7 – Overview Imagery (High Detail)

A series of images representing the total presence of lakes in each year. Imagery presented from USGS data store (USGS, <https://earthexplorer.usgs.gov>, January 2020), with background imagery from Sentinel 2 tiles. Lakes were determined using a simple Green – NIR NDWI method, and overlain on the basemap as polygon vector features represented here in red. Images here displayed at 300dpi, and 32bit colour (1872x1309 px).



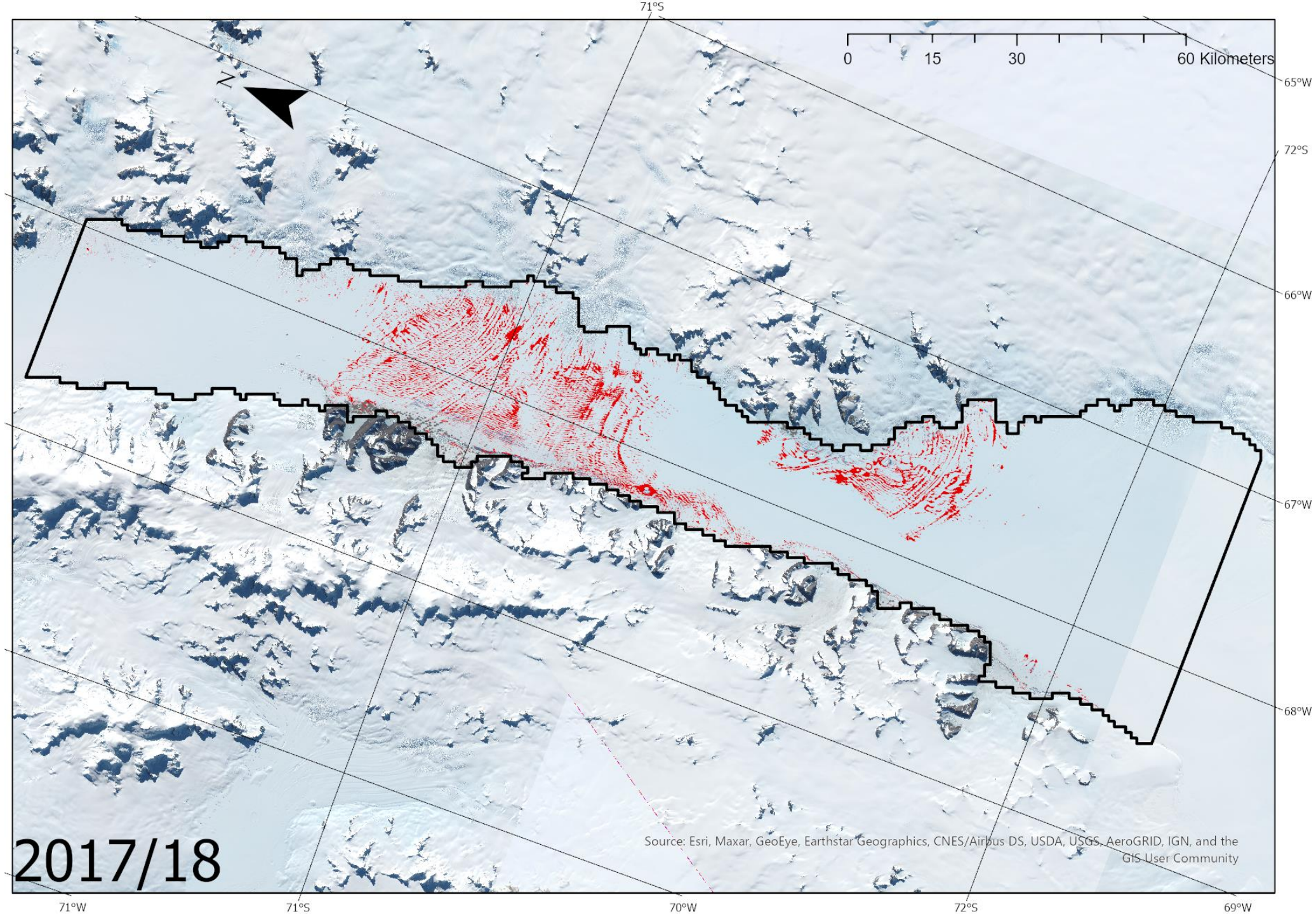
2019/20

Source: Esri, Maxar, GeoEye, Earthstar Geographics, CNES/Airbus DS, USDA, USGS, AeroGRID, IGN, and the GIS User Community



2018/19

Source: Esri, Maxar, GeoEye, Earthstar Geographics, CNES/Airbus DS, USDA, USGS, AeroGRID, IGN, and the GIS User Community



0 15 30 60 Kilometers

65°W

72°S

66°W

67°W

68°W

Source: Esri, Maxar, GeoEye, Earthstar Geographics, CNES/Airbus DS, USDA, USGS, AeroGRID, IGN, and the GIS User Community

2017/18

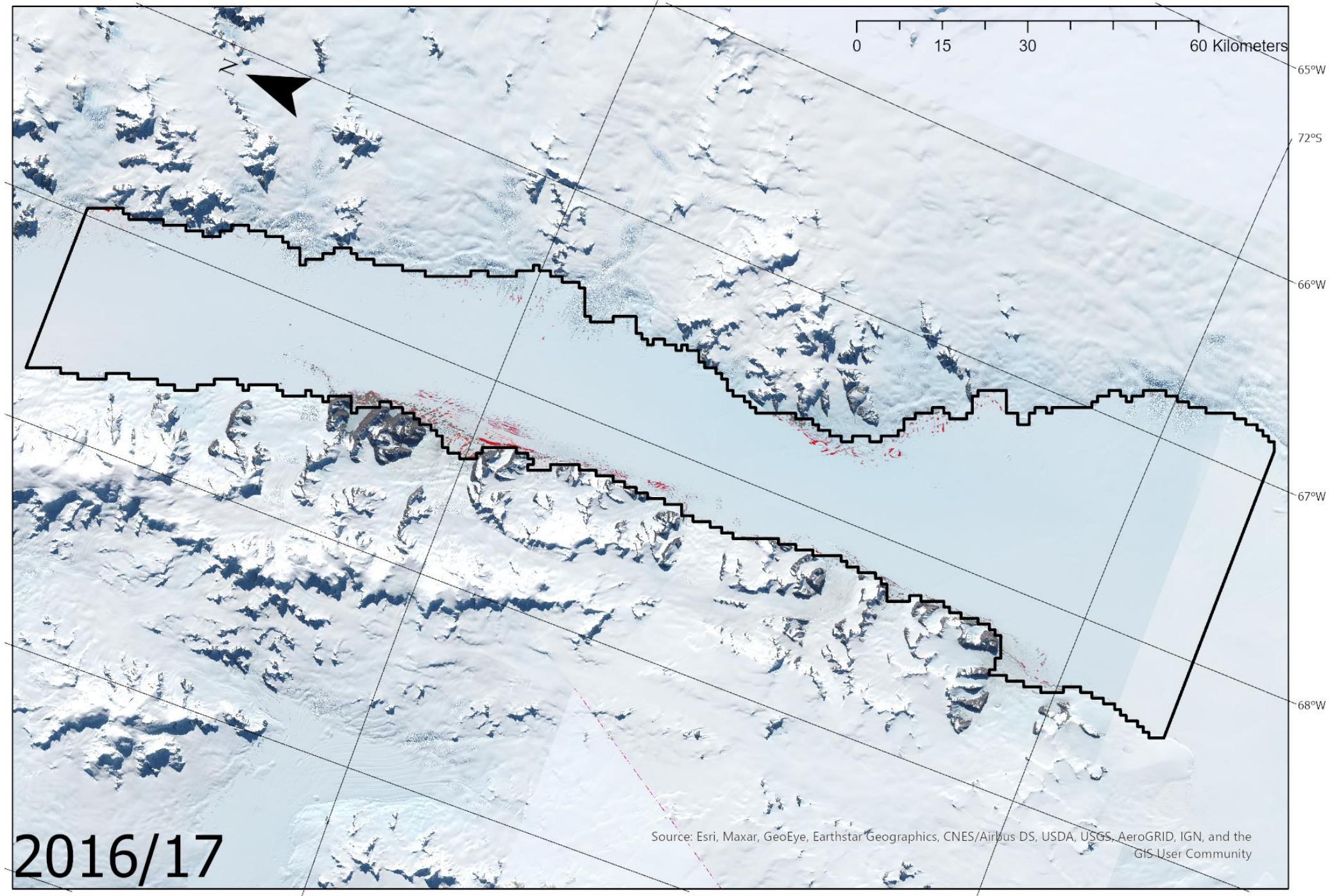
71°W

71°S

70°W

72°S

69°W



0 15 30 60 Kilometers

65°W

72°S

66°W

67°W

68°W

Source: Esri, Maxar, GeoEye, Earthstar Geographics, CNES/Airbus DS, USDA, USGS, AeroGRID, IGN, and the GIS User Community

2016/17

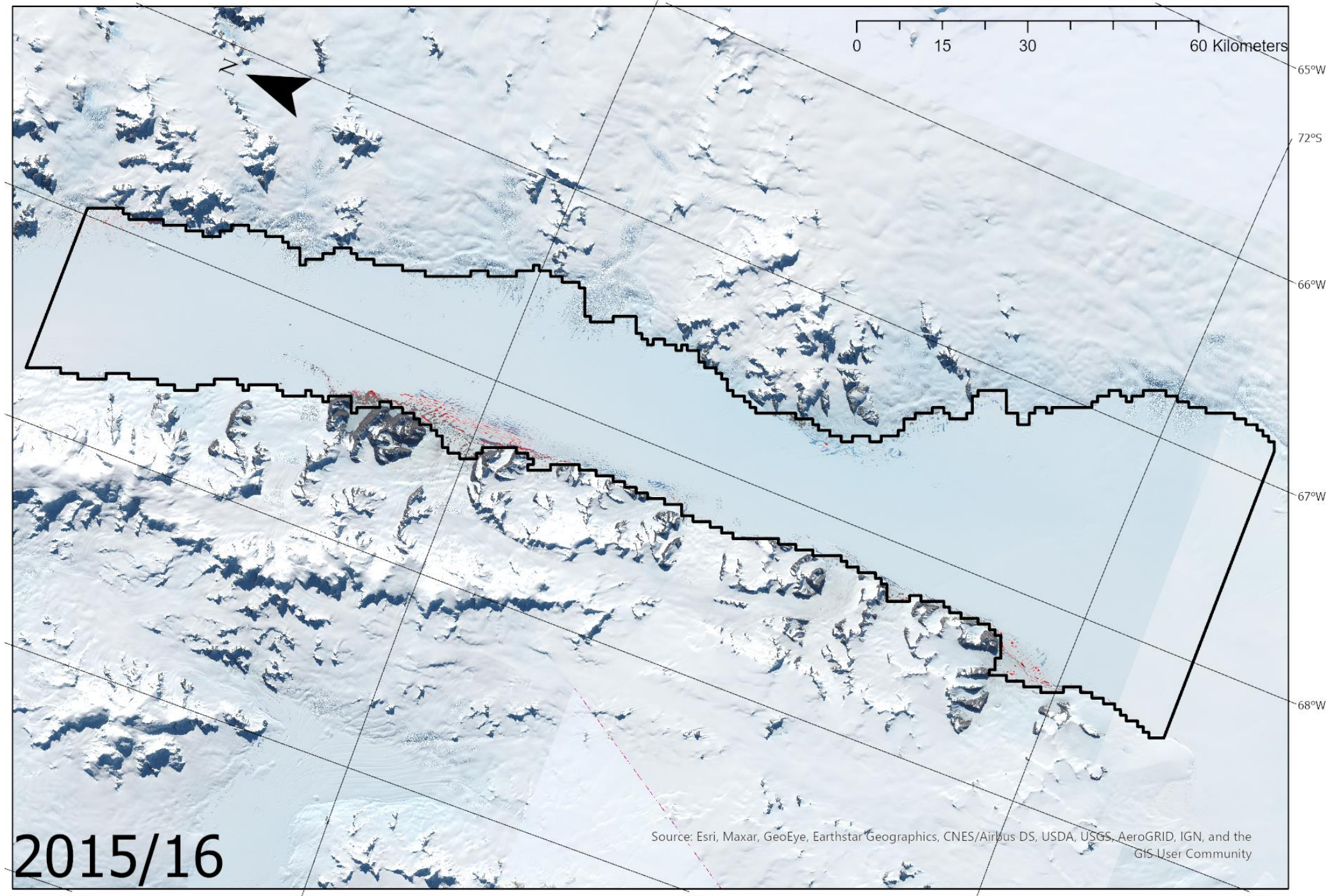
71°W

71°S

70°W

72°S

69°W



0 15 30 60 Kilometers

65°W

72°S

66°W

67°W

68°W

Source: Esri, Maxar, GeoEye, Earthstar Geographics, CNES/Airbus DS, USDA, USGS, AeroGRID, IGN, and the GIS User Community

2015/16

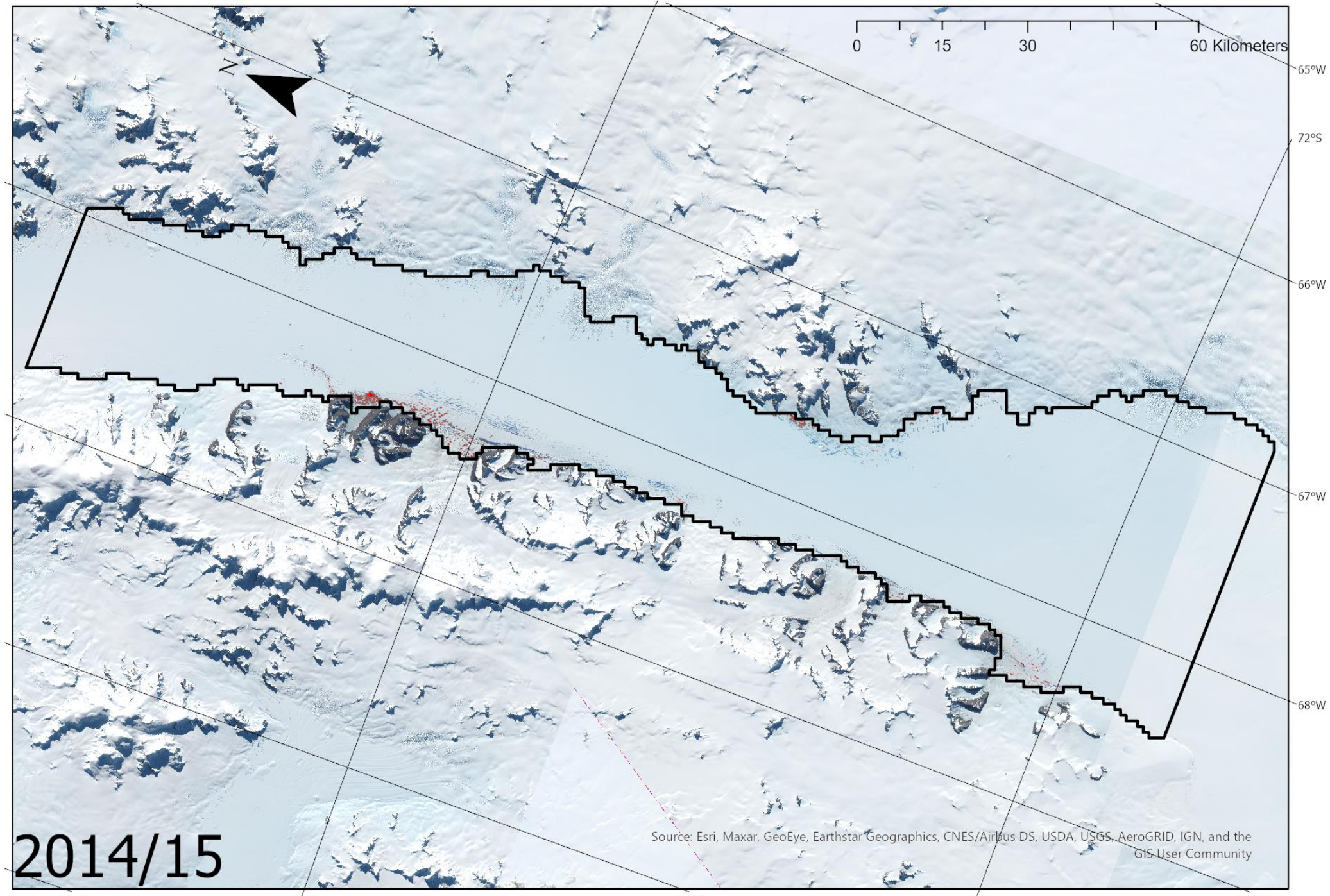
71°W

71°S

70°W

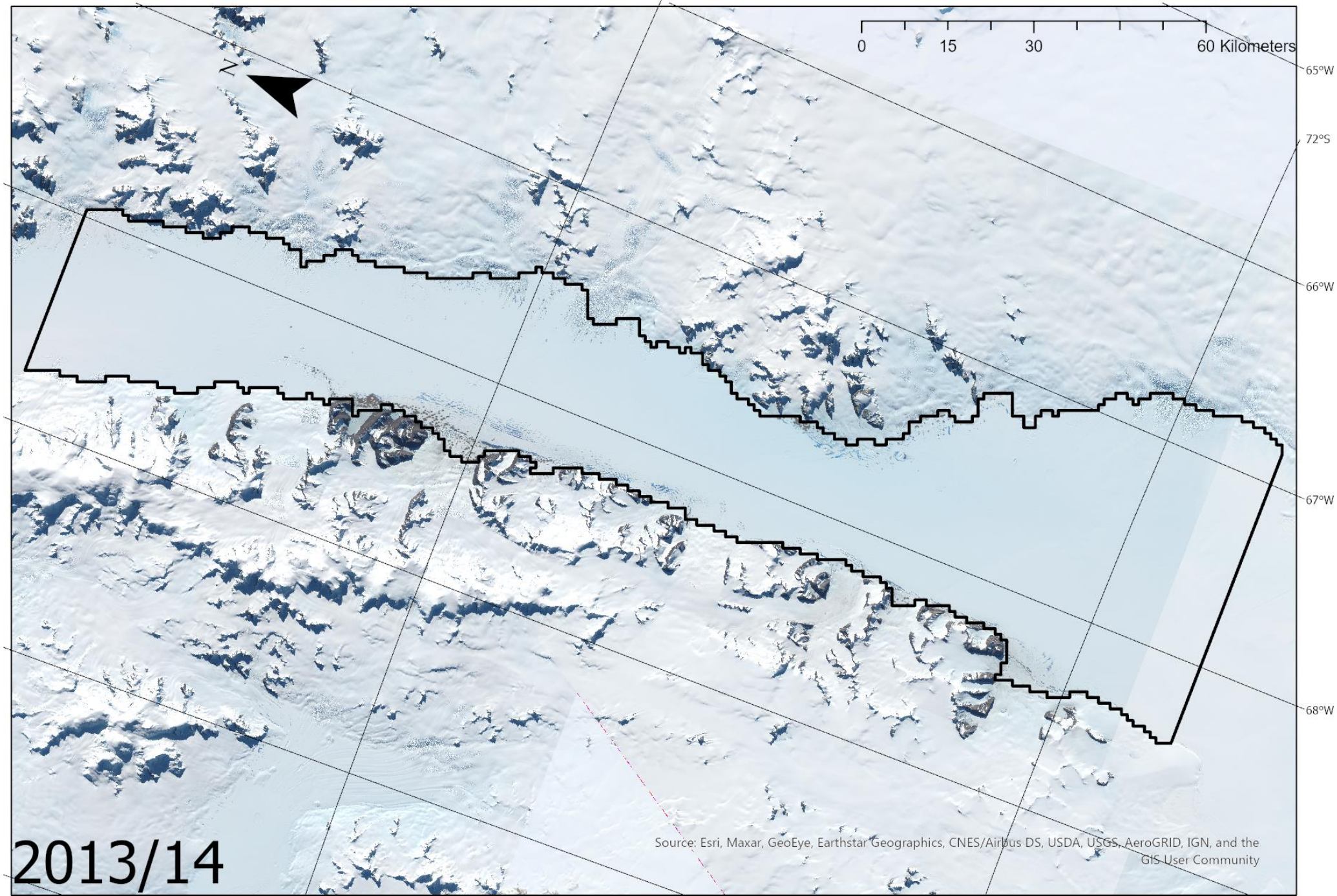
72°S

69°W



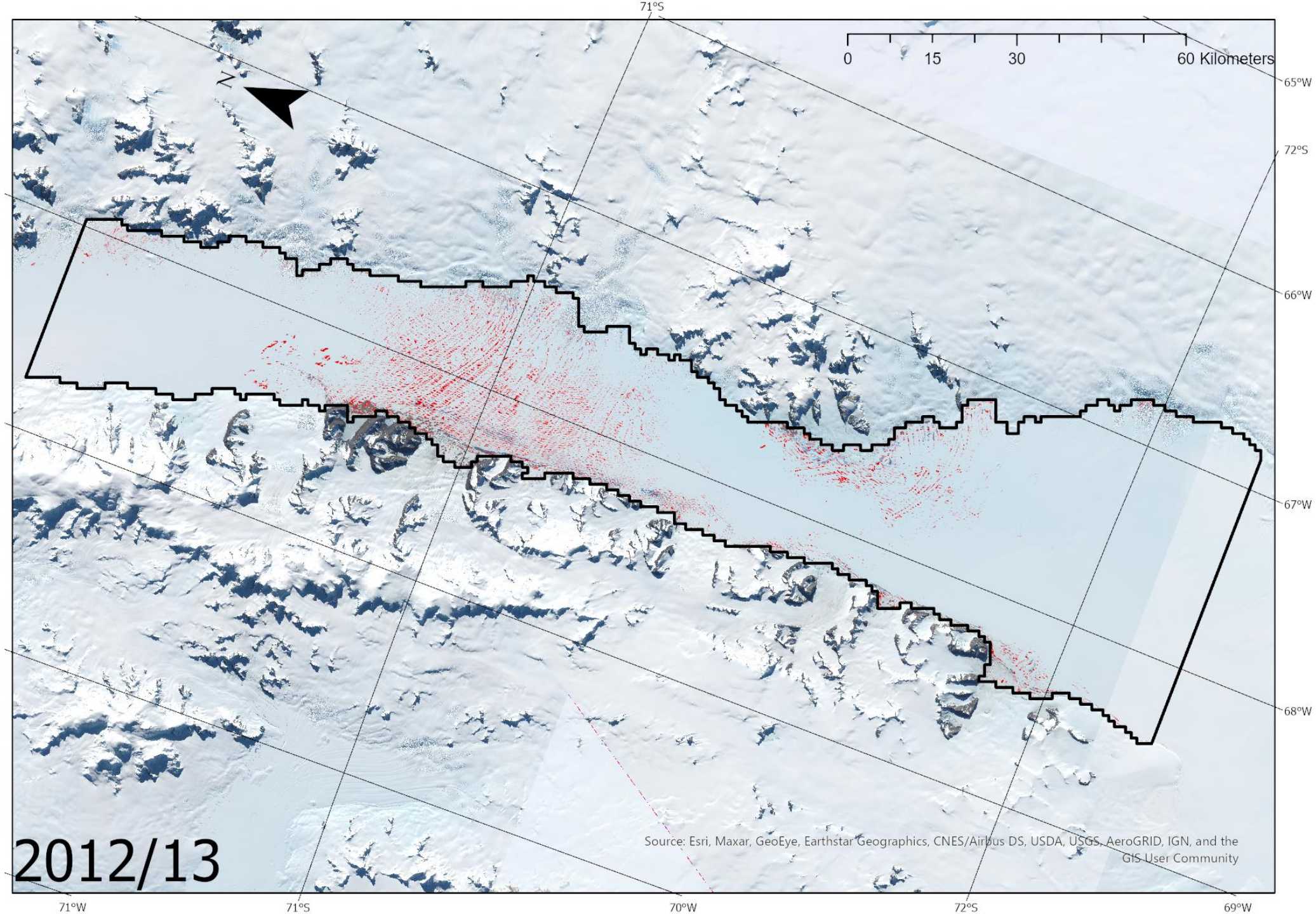
2014/15

Source: Esri, Maxar, GeoEye, Earthstar Geographics, CNES/Airbus DS, USDA, USGS, AeroGRID, IGN, and the GIS User Community



2013/14

Source: Esri, Maxar, GeoEye, Earthstar Geographics, CNES/Airbus DS, USDA, USGS, AeroGRID, IGN, and the GIS User Community



0 15 30 60 Kilometers

65°W

72°S

66°W

67°W

68°W

Source: Esri, Maxar, GeoEye, Earthstar Geographics, CNES/Airbus DS, USDA, USGS, AeroGRID, IGN, and the GIS User Community

2012/13

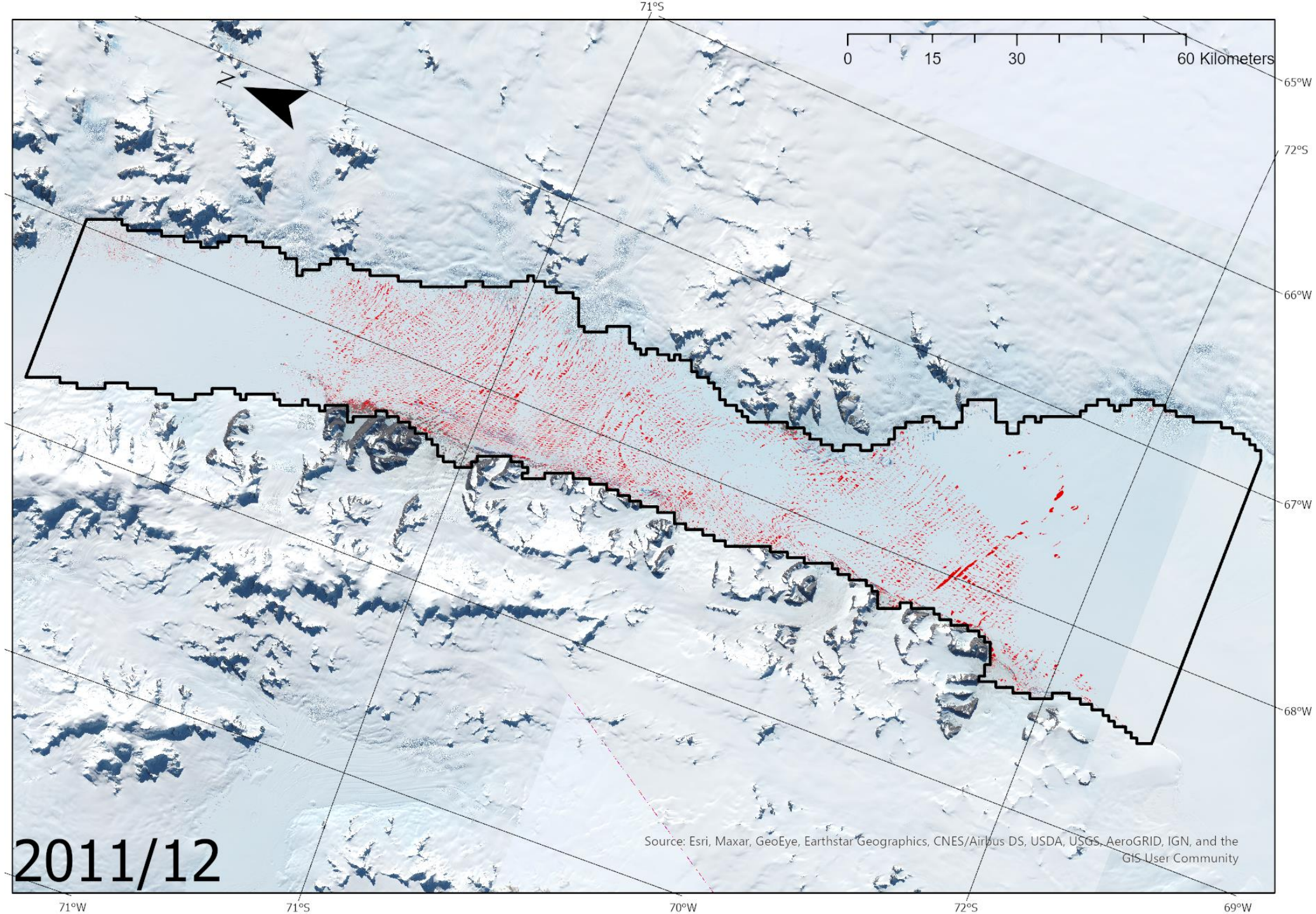
71°W

71°S

70°W

72°S

69°W



0 15 30 60 Kilometers

65°W

72°S

66°W

67°W

68°W

Source: Esri, Maxar, GeoEye, Earthstar Geographics, CNES/Airbus DS, USDA, USGS, AeroGRID, IGN, and the GIS User Community

2011/12

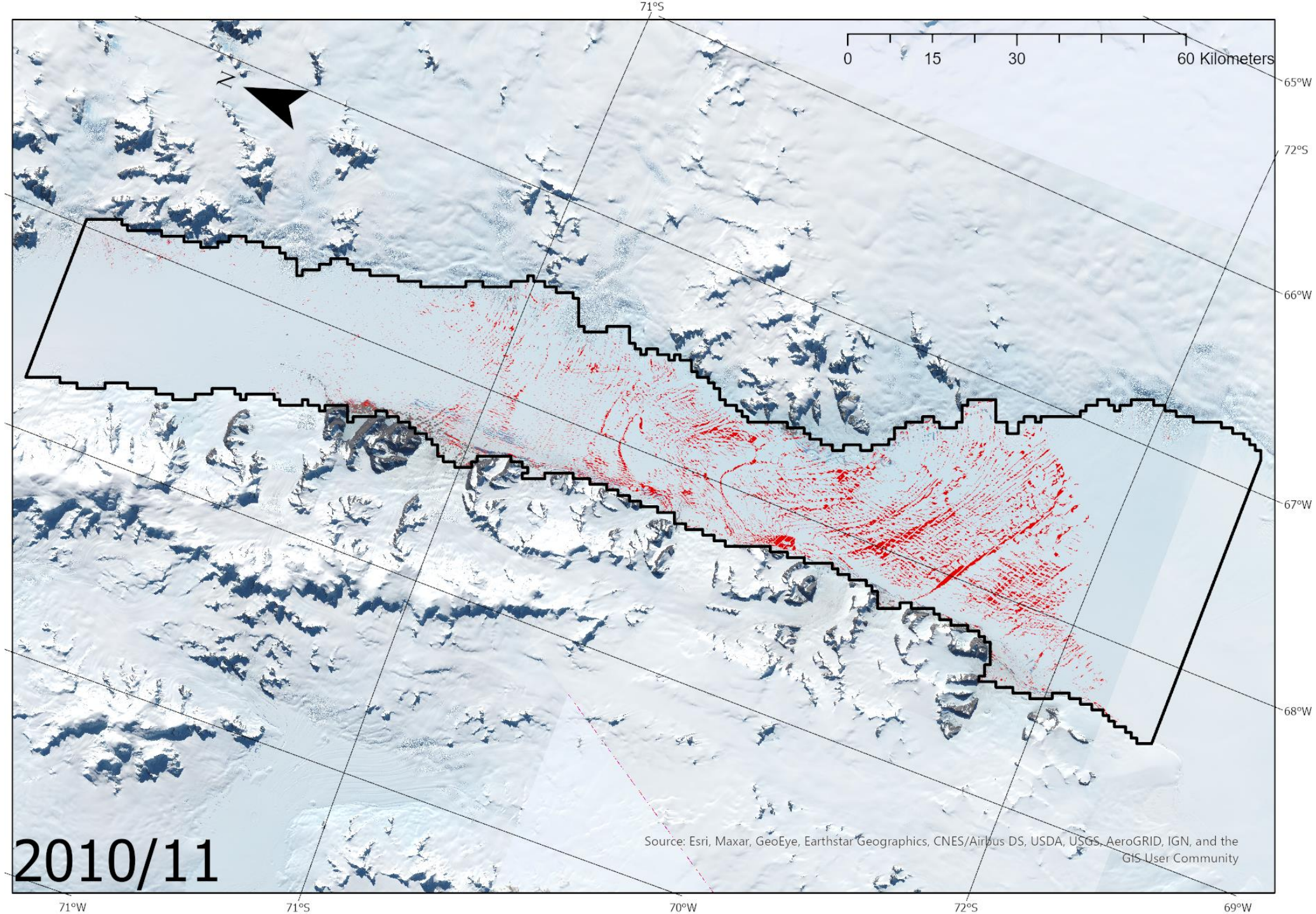
71°W

71°S

70°W

72°S

69°W



0 15 30 60 Kilometers

65°W

72°S

66°W

67°W

68°W

Source: Esri, Maxar, GeoEye, Earthstar Geographics, CNES/Airbus DS, USDA, USGS, AeroGRID, IGN, and the GIS User Community

2010/11

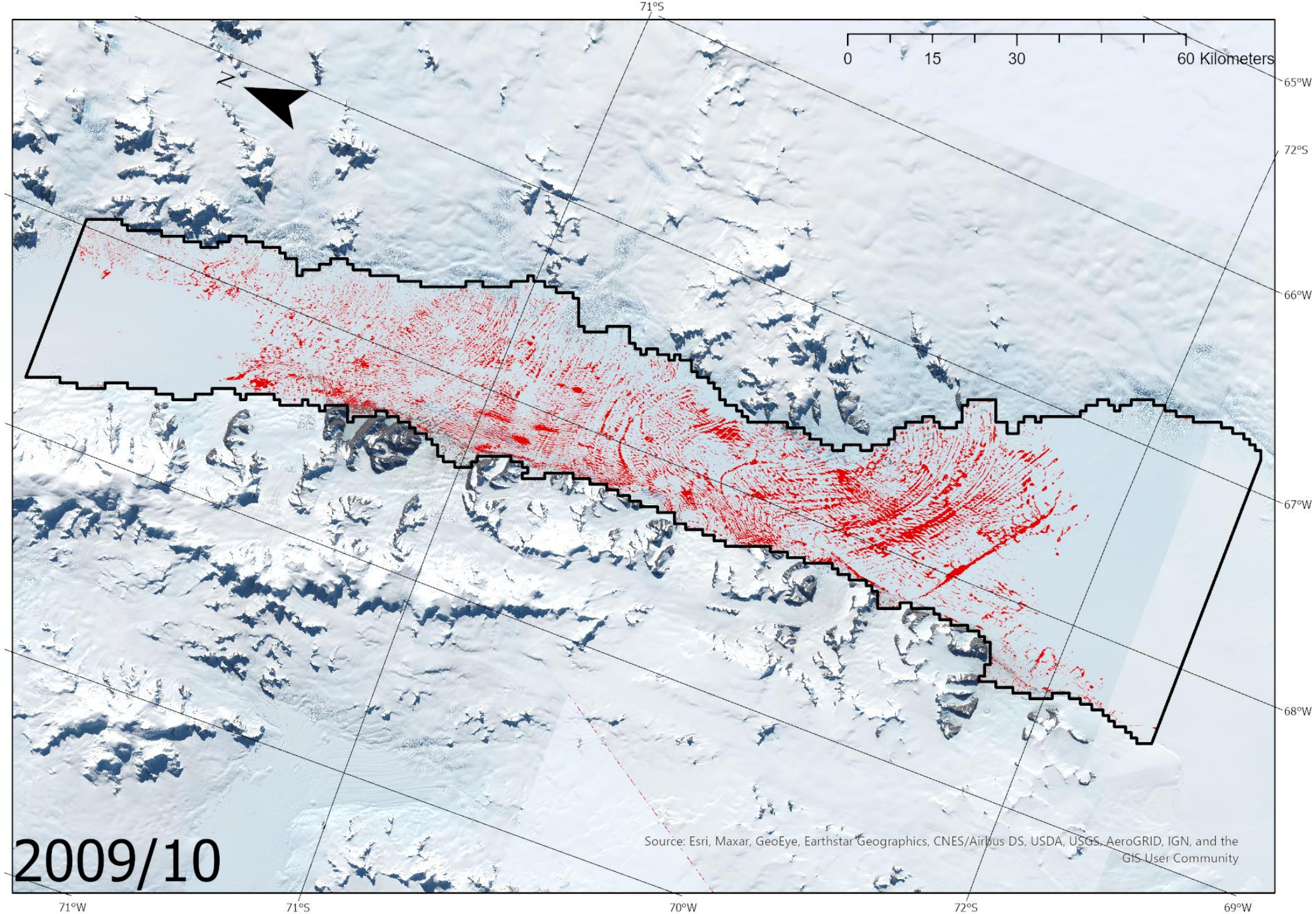
71°W

71°S

70°W

72°S

69°W



0 15 30 60 Kilometers

65°W

72°S

66°W

67°W

68°W

Source: Esri, Maxar, GeoEye, Earthstar Geographics, CNES/Airbus DS, USDA, USGS, AeroGRID, IGN, and the GIS User Community

2009/10

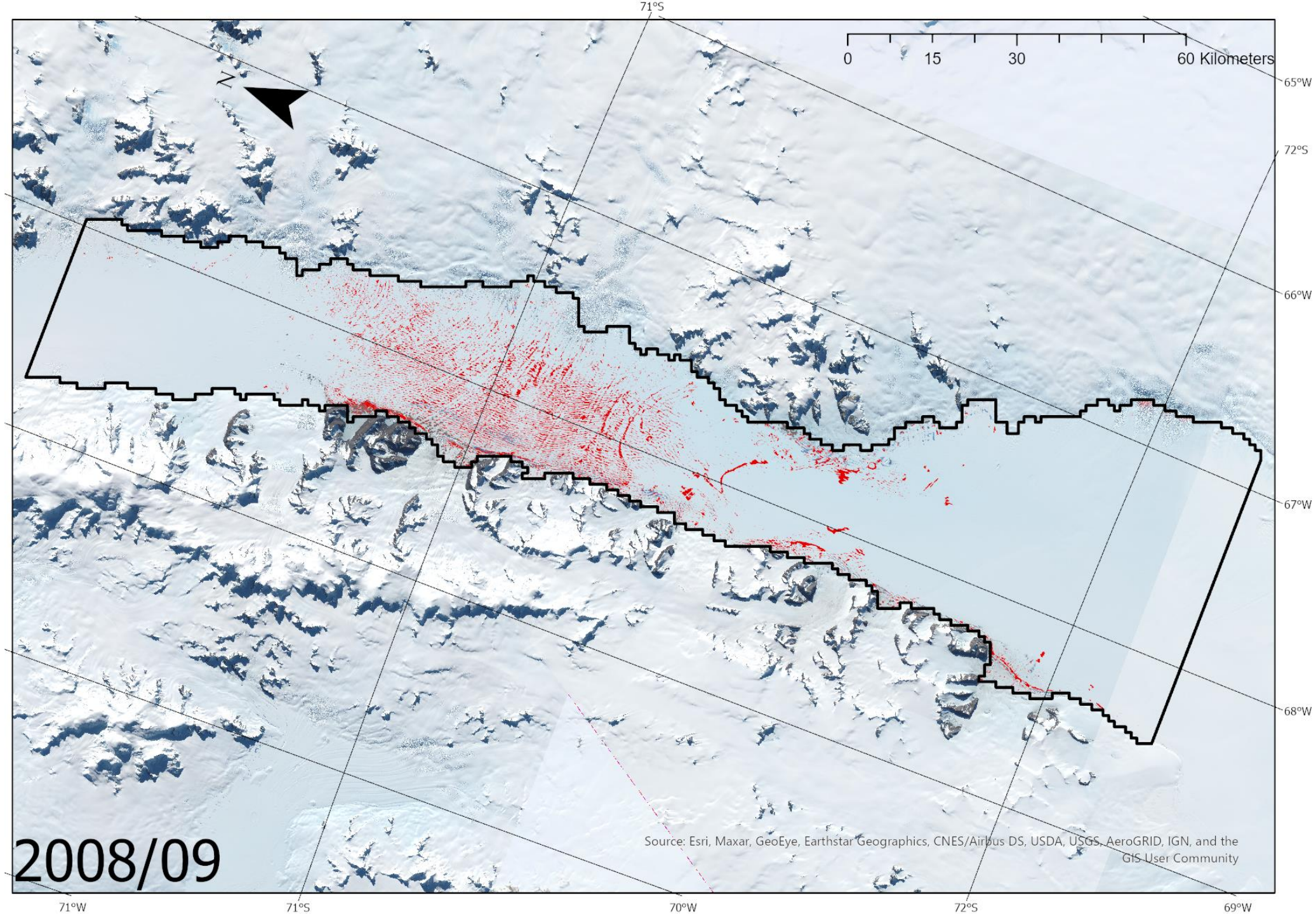
71°W

71°S

70°W

72°S

69°W



0 15 30 60 Kilometers

65°W

72°S

66°W

67°W

68°W

Source: Esri, Maxar, GeoEye, Earthstar Geographics, CNES/Airbus DS, USDA, USGS, AeroGRID, IGN, and the GIS User Community

2008/09

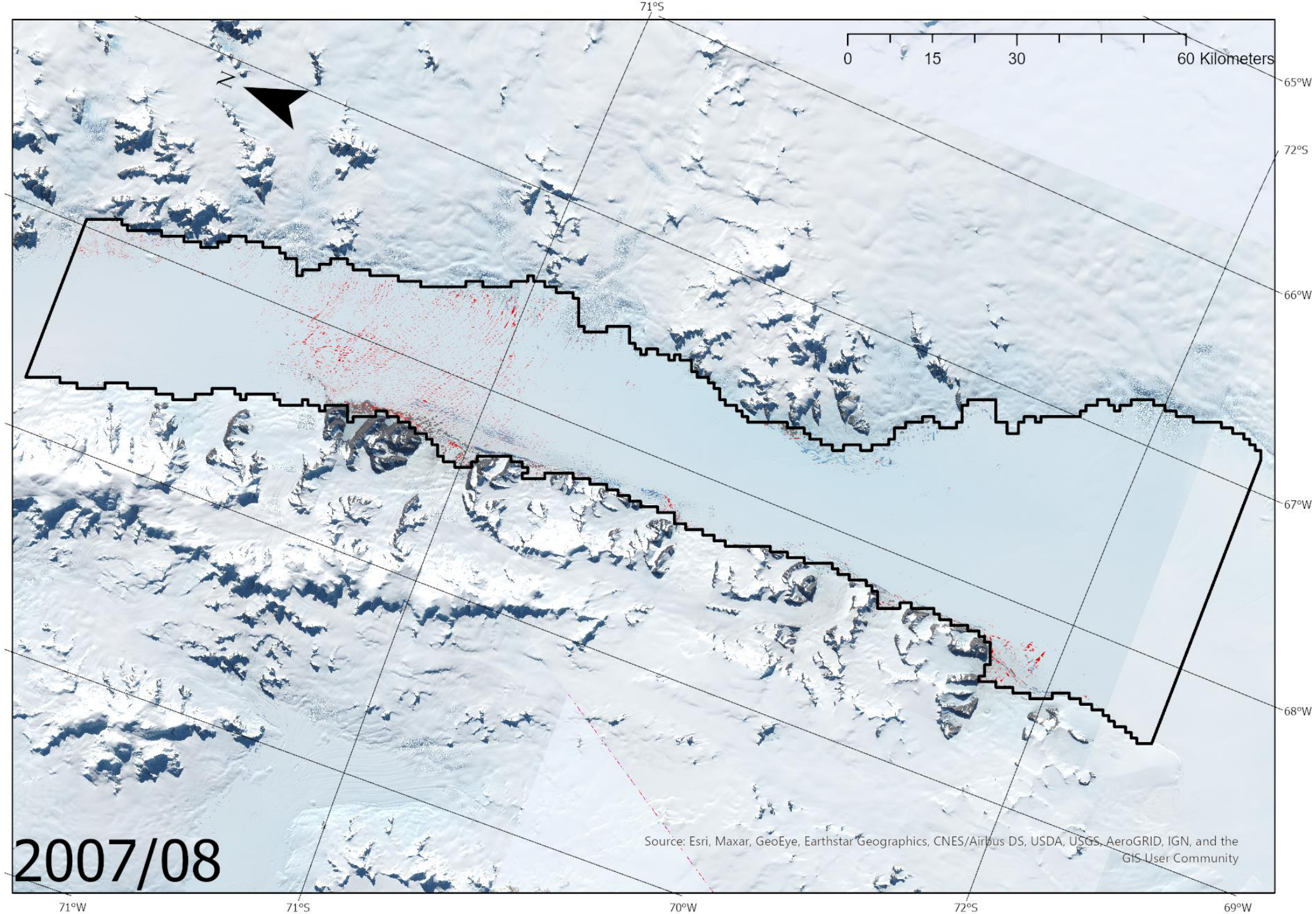
71°W

71°S

70°W

72°S

69°W



0 15 30 60 Kilometers

65°W

72°S

66°W

67°W

68°W

Source: Esri, Maxar, GeoEye, Earthstar Geographics, CNES/Airbus DS, USDA, USGS, AeroGRID, IGN, and the GIS User Community

2007/08

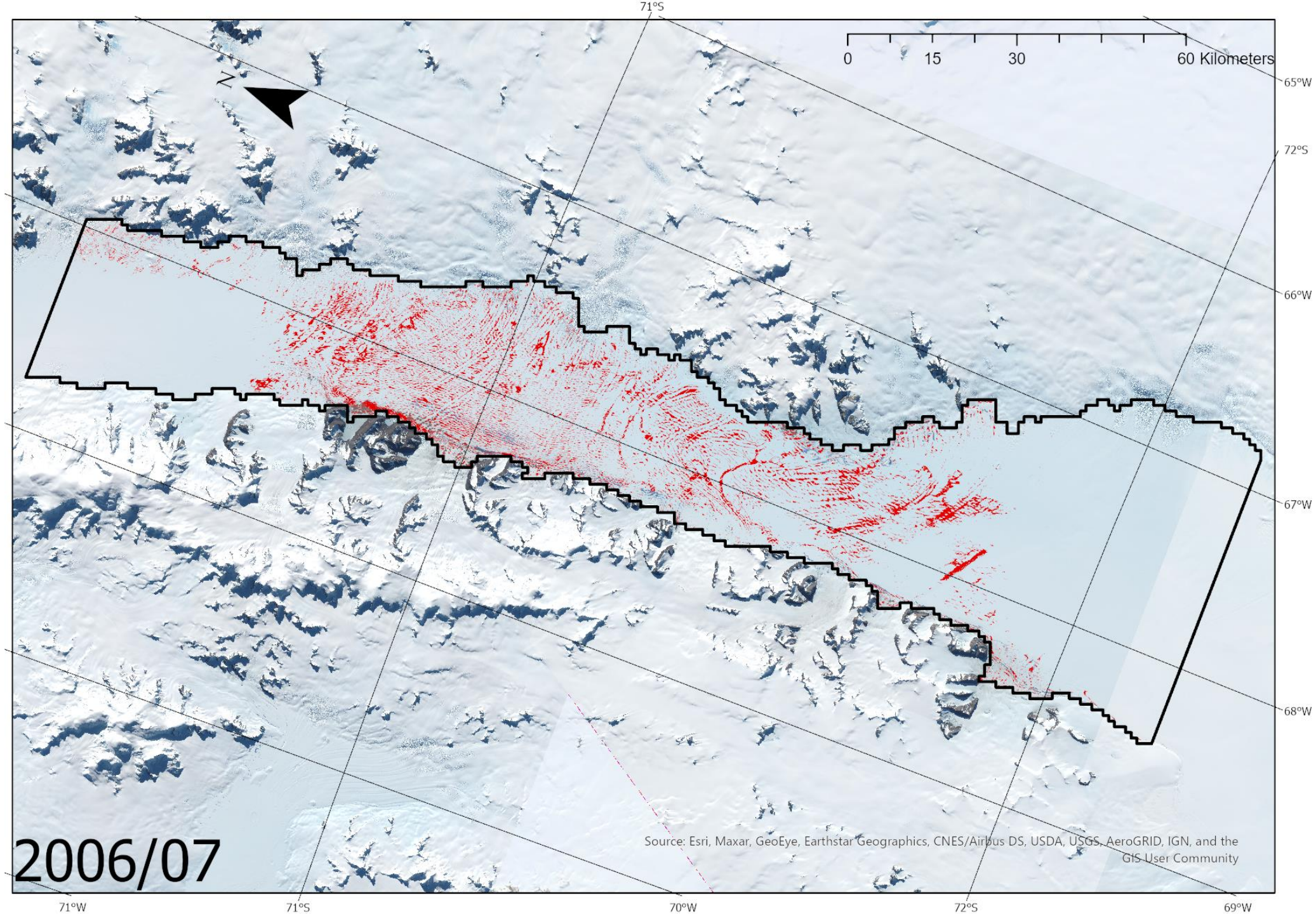
71°W

71°S

70°W

72°S

69°W



0 15 30 60 Kilometers

65°W

72°S

66°W

67°W

68°W

Source: Esri, Maxar, GeoEye, Earthstar Geographics, CNES/Airbus DS, USDA, USGS, AeroGRID, IGN, and the GIS User Community

2006/07

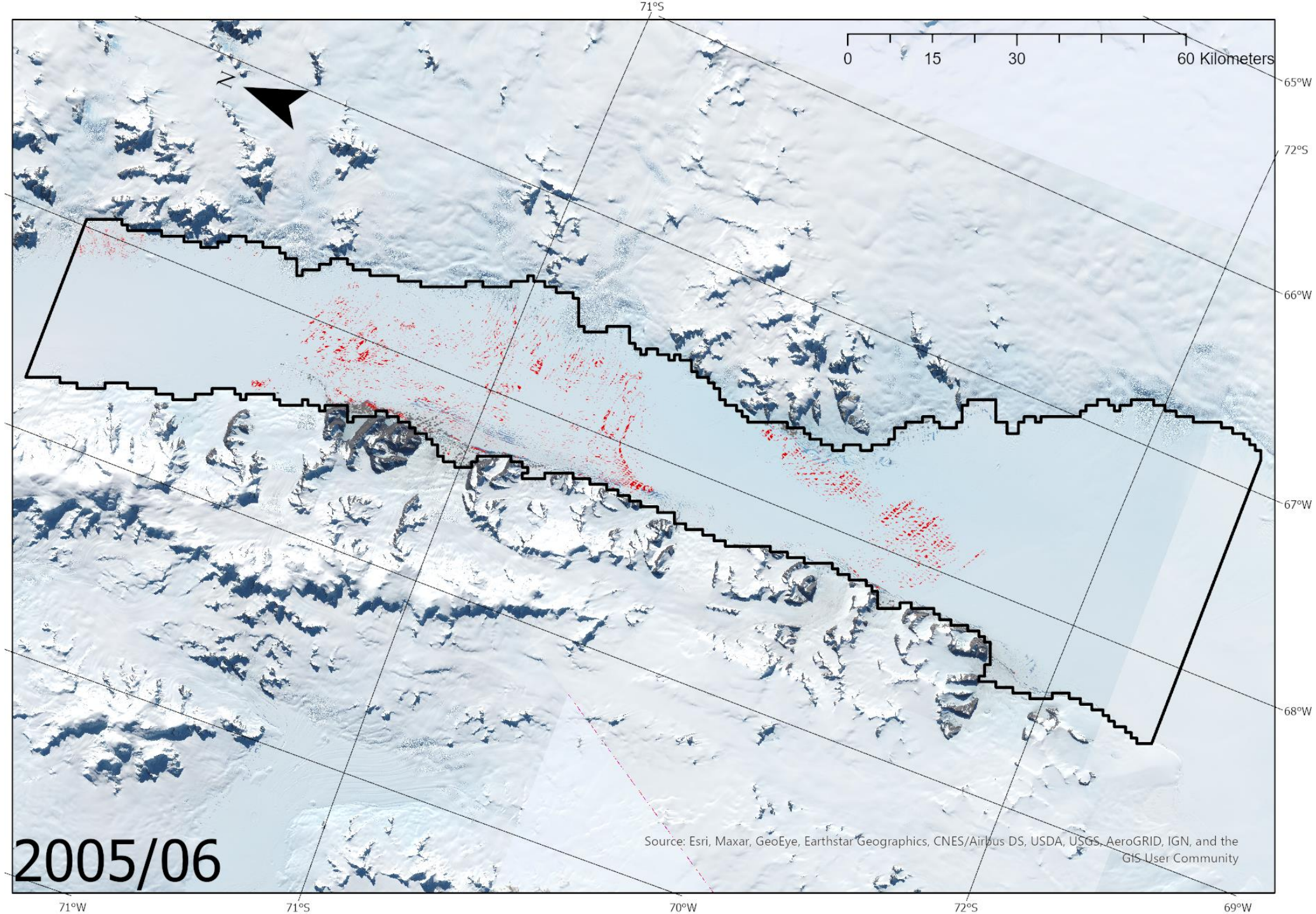
71°W

71°S

70°W

72°S

69°W



0 15 30 60 Kilometers

65°W

72°S

66°W

67°W

68°W

Source: Esri, Maxar, GeoEye, Earthstar Geographics, CNES/Airbus DS, USDA, USGS, AeroGRID, IGN, and the GIS User Community

2005/06

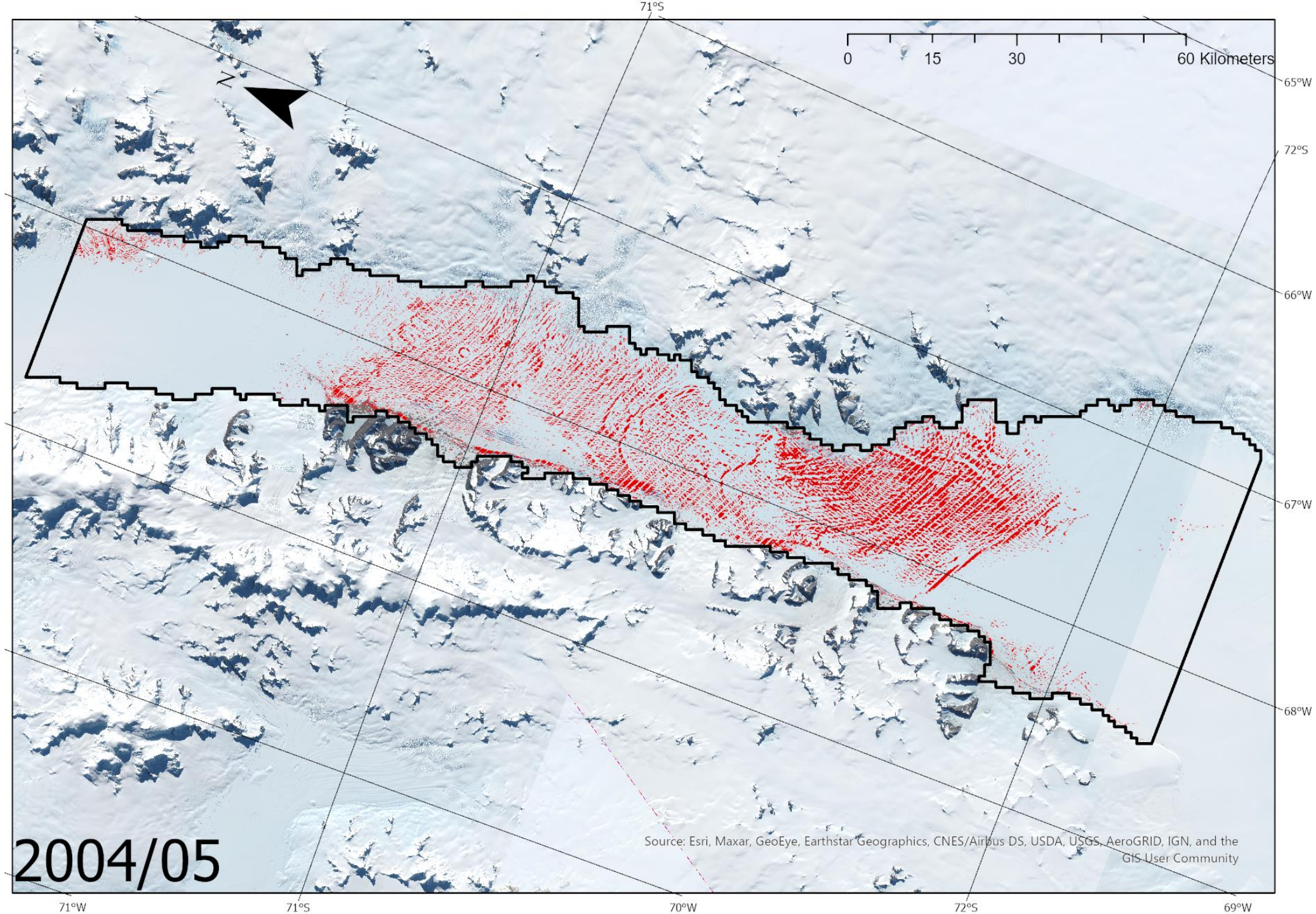
71°W

71°S

70°W

72°S

69°W



0 15 30 60 Kilometers

65°S

66°S

67°S

68°S

71°W

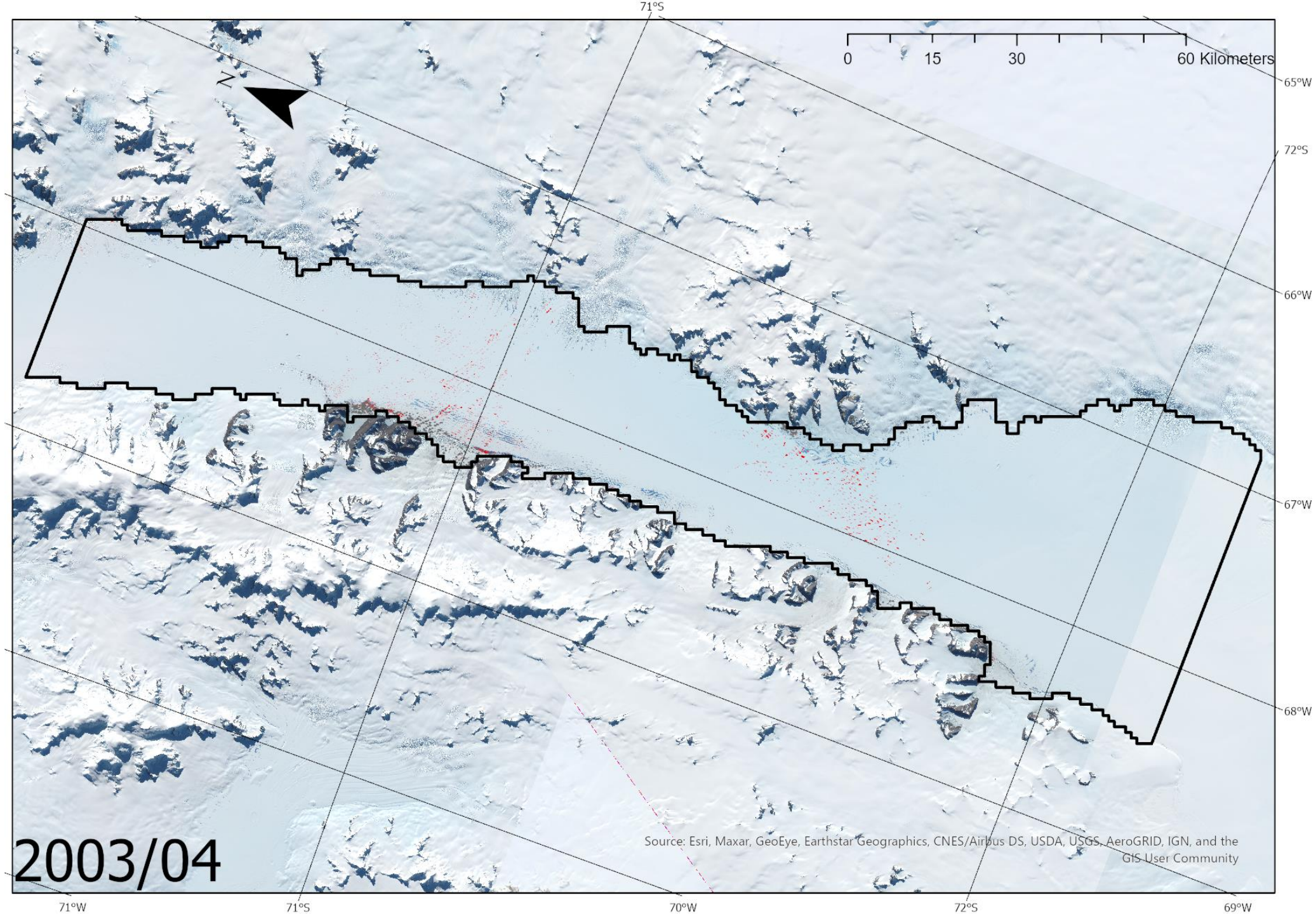
70°W

72°W

69°W

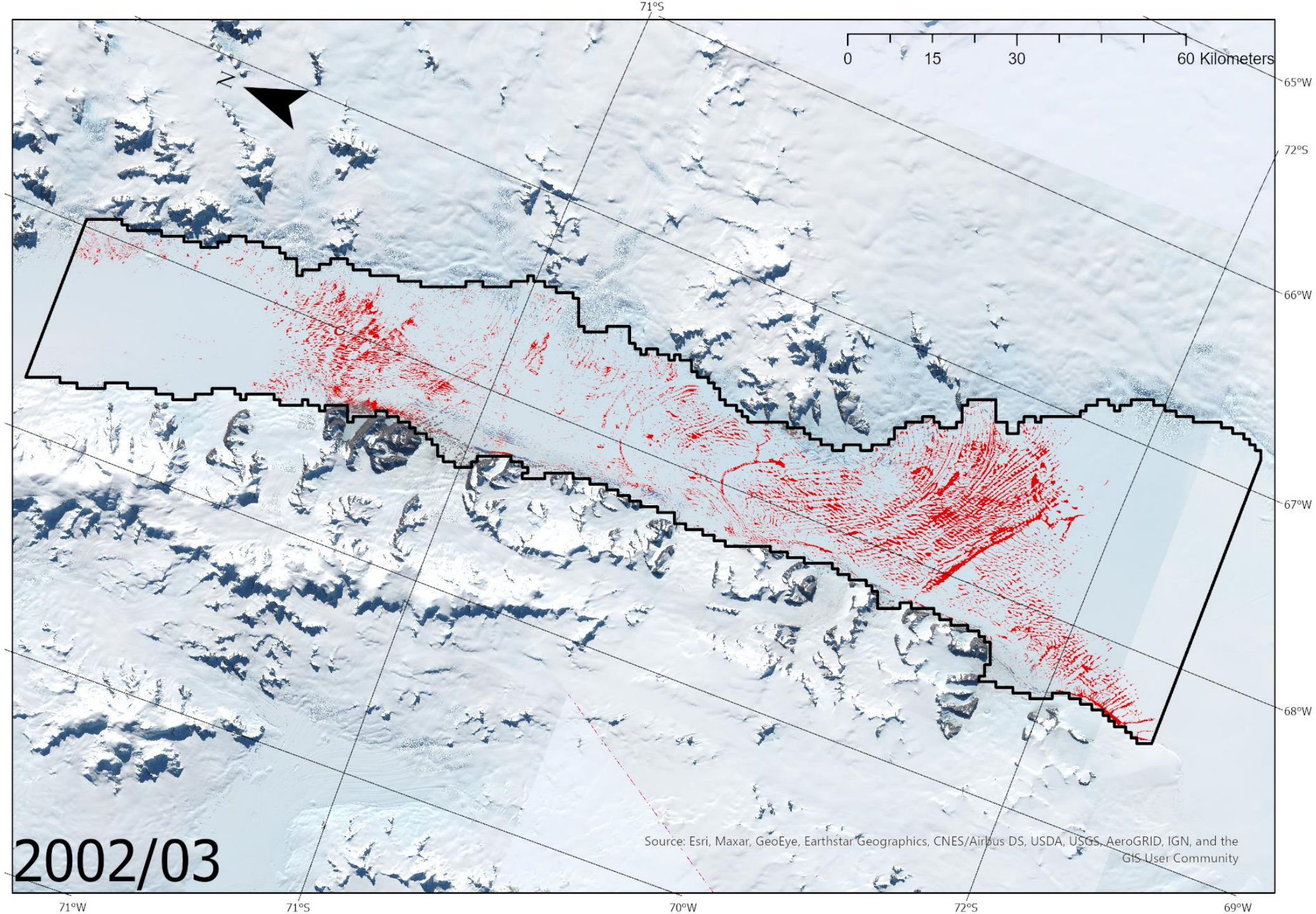
2004/05

Source: Esri, Maxar, GeoEye, Earthstar Geographics, CNES/Airbus DS, USDA, USGS, AeroGRID, IGN, and the GIS User Community



2003/04

Source: Esri, Maxar, GeoEye, Earthstar Geographics, CNES/Airbus DS, USDA, USGS, AeroGRID, IGN, and the GIS User Community



0 15 30 60 Kilometers

65°W

72°S

66°W

67°W

68°W

Source: Esri, Maxar, GeoEye, Earthstar Geographics, CNES/Airbus DS, USDA, USGS, AeroGRID, IGN, and the GIS User Community

2002/03

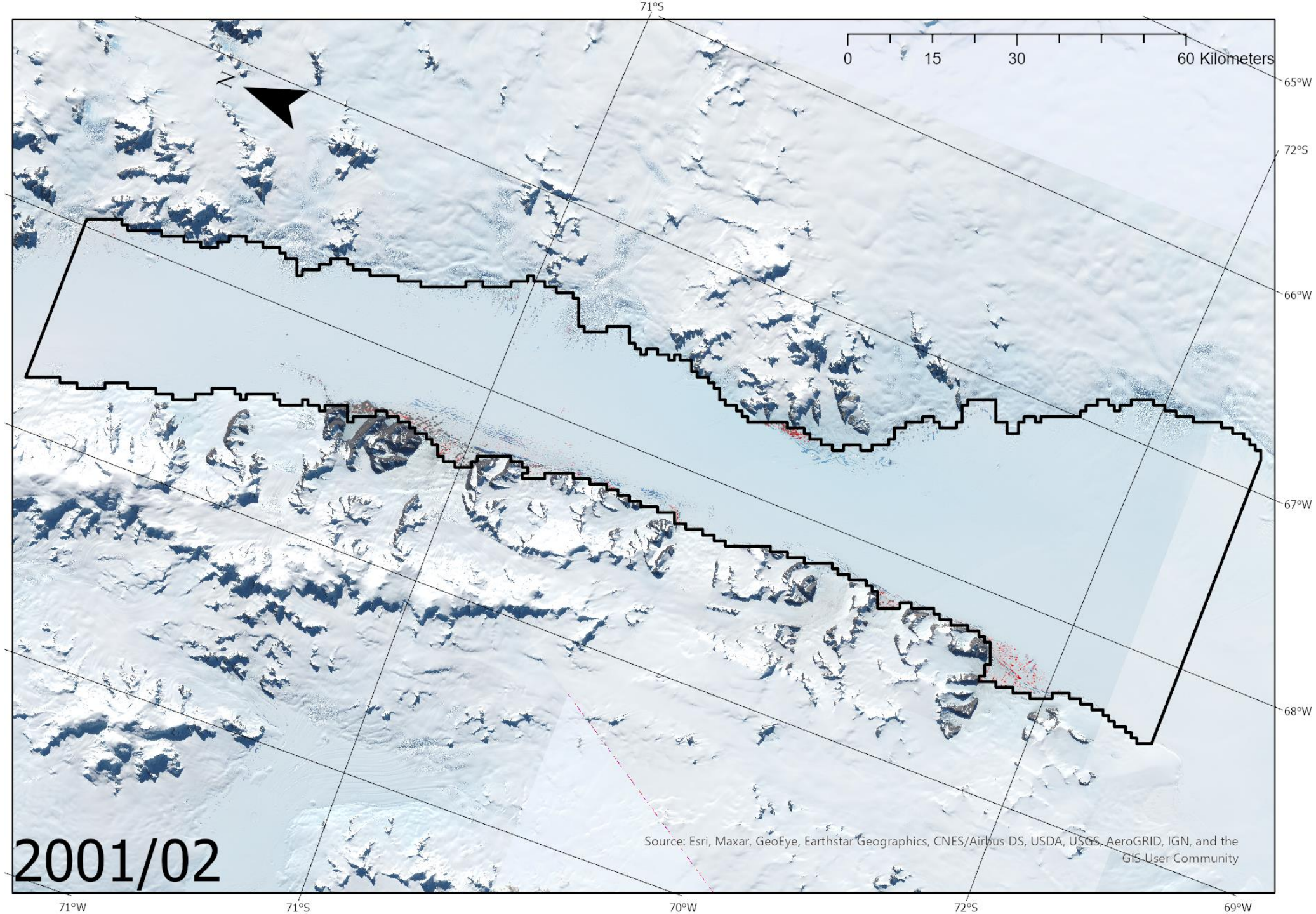
71°W

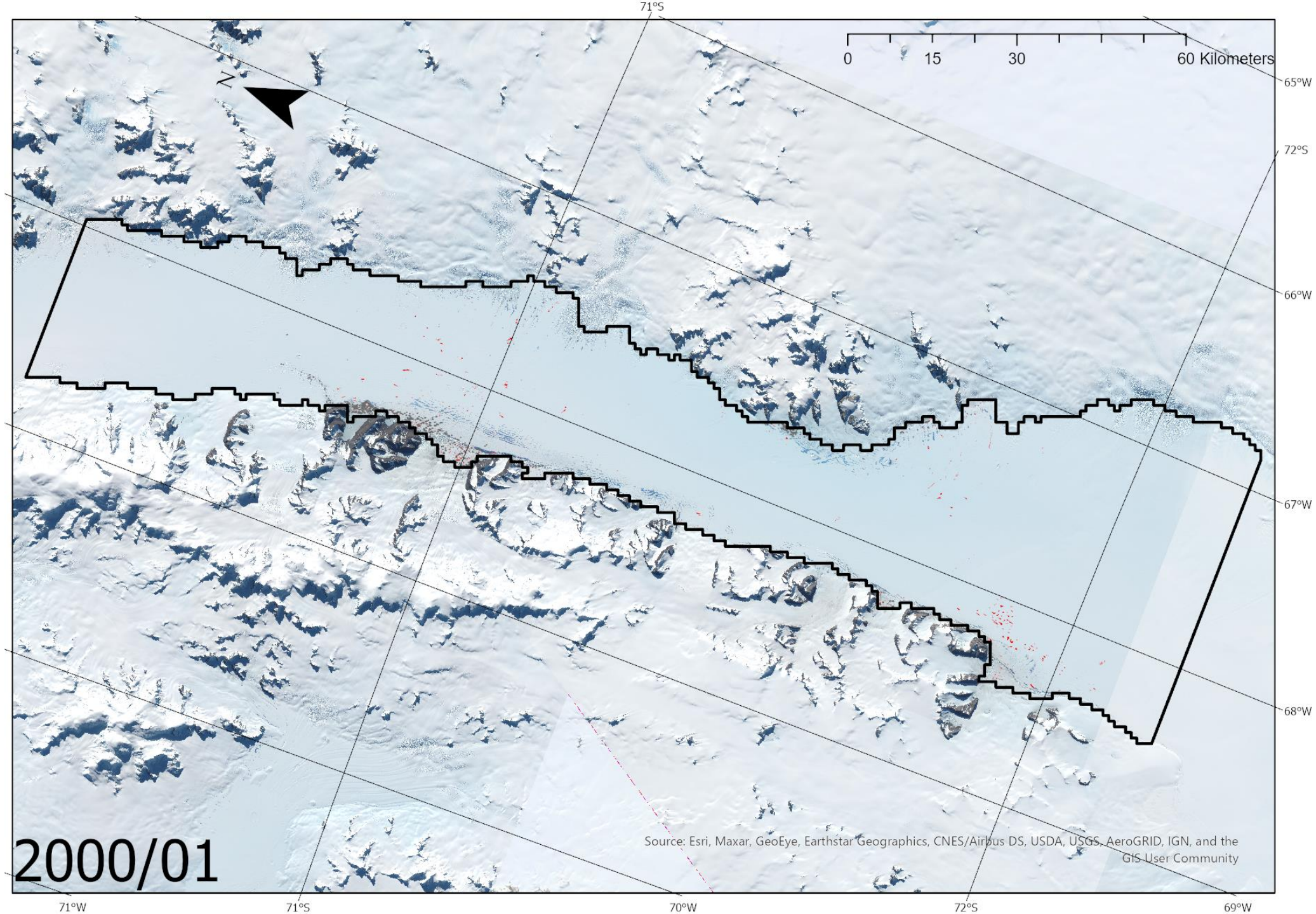
71°S

70°W

72°S

69°W





0 15 30 60 Kilometers

65°W

72°S

66°W

67°W

68°W

Source: Esri, Maxar, GeoEye, Earthstar Geographics, CNES/Airbus DS, USDA, USGS, AeroGRID, IGN, and the GIS User Community

2000/01

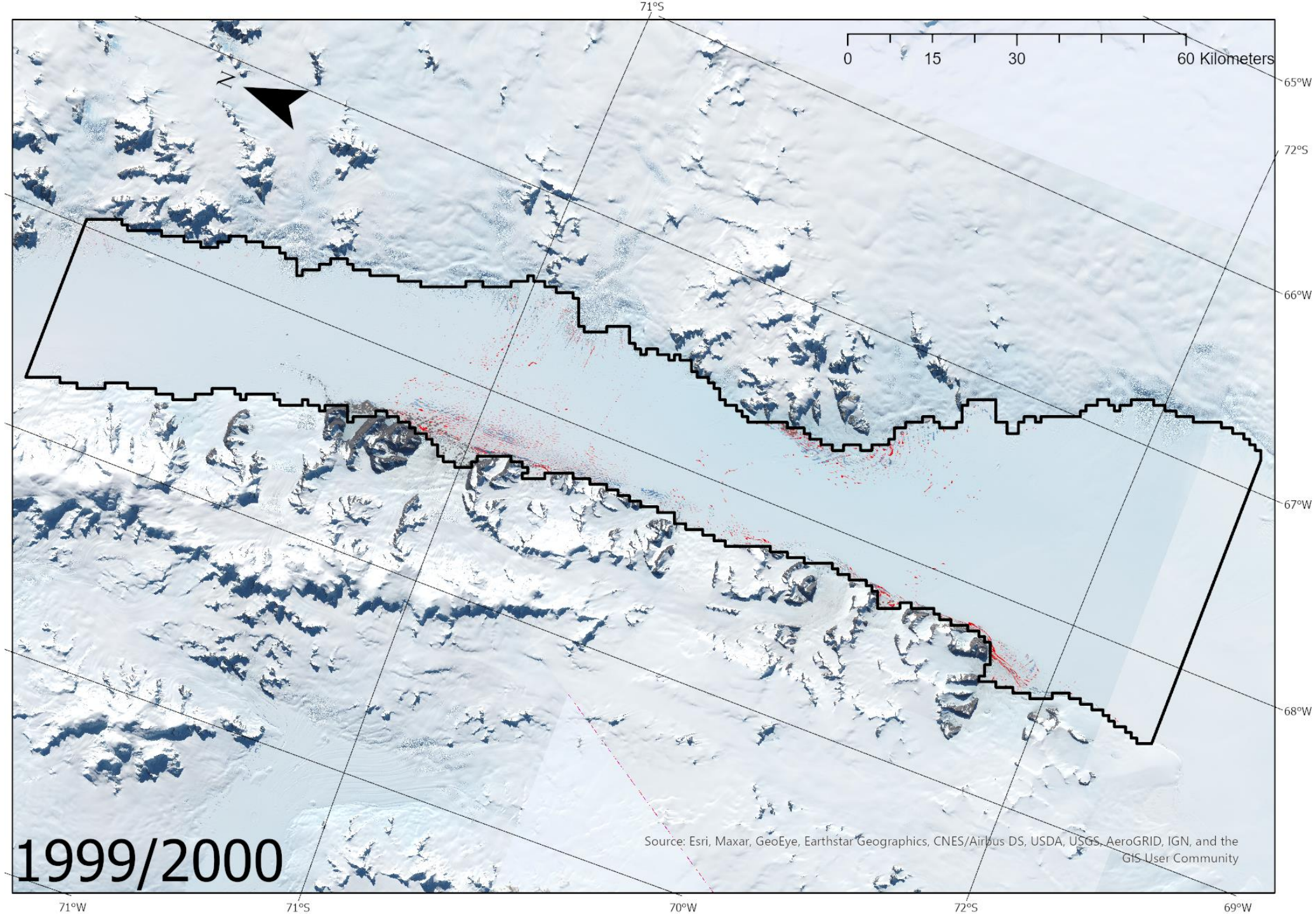
71°W

71°S

70°W

72°S

69°W



0 15 30 60 Kilometers

65°W

72°S

66°W

67°W

68°W

Source: Esri, Maxar, GeoEye, Earthstar Geographics, CNES/Airbus DS, USDA, USGS, AeroGRID, IGN, and the GIS User Community

1999/2000

71°W

71°S

70°W

72°S

69°W

Year	Red No Lake	Red Lake	Green No Lake	Green Lake	Blue No Lake	Blue Lake	NIR No Lake	NIR Lake	Avg
2020	8385.638	8243.976	7663.393	7442.074	7629.449	7178.299	6645.762	6076.157	
%Decrease		1.689%		2.888%		5.913%		8.571%	4.765%
2019	6936.556	6936.375	6302.731	6302.259	6587.651	6586.502	6044.193	6042.556	
%Decrease		0.003%		0.007%		0.017%		0.027%	0.014%
2018	6939.032	6939.314	6250.227	6210.442	6214.270	6090.866	5109.981	4955.416	
%Decrease		-0.004%		0.637%		1.986%		3.025%	1.411%
2017	8251.072	8241.980	7418.115	7407.496	7578.256	7561.958	6600.823	6582.385	
%Decrease		0.110%		0.143%		0.215%		0.279%	0.187%
2016	0.922	0.920	0.848	0.846	0.845	0.842	0.772	0.768	
%Decrease		0.194%		0.253%		0.382%		0.521%	0.337%
2015	0.874	0.874	0.792	0.792	0.800	0.800	0.751	0.750	
%Decrease		0.037%		0.044%		0.059%		0.072%	0.053%
2014	0.927	0.927	0.852	0.852	0.853	0.853	0.769	0.769	
%Decrease		0.000%		0.000%		0.000%		0.000%	0.000%

	Lake Area (m)	Lake Density	Avg % Decrease	Avg Lake Depth (m)	Snow Albedo	Surface Clear Sky Radiation	Calc'd Albedo
2014	46800	0.00%	0.000%	-	0.850	25299852.000	0.850
2015	172059361	2.54%	0.053%	0.485	0.850	16596446.000	0.850
2016	15820334	0.23%	0.337%	0.865	0.850	25254262.000	0.847
2017	78567536	1.16%	0.187%	0.722	0.850	16251910.000	0.848
2018	211696435	3.12%	1.411%	0.480	0.850	16516097.000	0.838
2019	4055400	0.06%	0.014%	0.736	0.850	28741310.000	0.850
2020	801327600	11.83%	4.765%	0.433	0.850	25159764.000	0.809

**APPENDIX 8 - Top:** Table calculating % decrease in reflectivity between George VI with lakes, and without lakes in corresponding years. Average % decrease is added in the final column, which is considered the % change in albedo for the northern sector (study area).

**Bottom:** Table calculating true change in albedo from albedo % change averages. This is applied to the ERA 5 Snow albedo values for the study area per corresponding year. The resultant changed albedo value is shown in the final column (Calc'd Albedo), with the greatest change being in 2020, of a 0.04 decrease in albedo between a snow covered George VI from 2020, and George VI with 2020's lakes.